# Microstructural Evolution of A Dual Phase Steel During Continuous Annealing

## Master thesis

X. Wu

August-2016

TATA STEEL

TU Delft

# Microstructural Evolution of A Dual Phase Steel During Continuous Annealing

Master thesis

by

X. Wu

A master thesis submitted to the
Department of Material Science and Engineering
at the faculty 3ME of the TU Delft
in partial fulfilment of the requirements

for the degree

MASTER OF SCIENCE
in
Material Science and Engineering

in the specialisation of Metal Science

Delft, The Netherlands
August 2016

*This thesis is confidential and cannot be made public.*


# Microstructural Evolution of A Dual Phase Steel During Continuous Annealing

Master thesis

by

X. Wu

Abstract: With a combination of high strength and good formability, dual-phase steels have gained much interest in the automobile industry. The final microstructure, which leads to mechanical properties of the product, is strongly dependent on the processing of the steel. Apart from hot-rolling and cold-rolling, the parameters during continuous annealing are of great importance to control the properties of the final product. This thesis is aimed to study the influence of heating rates on the microstructual evolution of a DP-steel during continuous annealing lines. The microstructual evolution evolves several phenomena, such as ferrite recrystallization, pearlite degradation, and austenite phase transformation. Experimental approaches as dilatometry and SEM are used to investigate the evolution, by applying different heating rates and stop-quenching at different temperature and soaking times. Modelling approaches, CA-model and phase field model, are also introduced to provide a further insight into the phenomena.

Keywords: Dual-phase steel, austenitization, continuous annealing

Student number: 4326687
Project duration: November 24, 2015 - September 10, 2016
Supervisors: Dr. ir. J. Sietsma, TU Delft
Dr. J. van Krevel, Tata Steel Europe IJmuiden

TU Delft Delft University of Technology

TATA TATA STEEL

# Acknowledgements

Firstly, I would like to give my biggest thanks to my supervisors, Jilt Sietsma, Joost van Krevel and Pina Mecozzi, for introducing me into the fascinating world of metallurgy, and for leading me through the zigzagging path of research. I would like to thank Pieter van der Wolk as well, for welcoming me into his group and letting me carry out the project.

Through the process of the project, my colleges from TATA steel have assisted me with all their knowledge, time and companionship, and that I would like to give a special thanks to: Joost, who has always been there, introducing me to the whole company and the group, giving me ideas and encouraging me when faced with obstacles, let alone all the trivial matters he has done to help me settle in the company; Winfried and Neus, for being there at my presentations, providing valuable suggestions all the time; Nick, Richard, and Tu, for helping me arranging everything, preparing all the samples and insisting me with efficient work and warm chats; the whole HSS group, who provided a sea of experience and knowledge for me to seek whenever needed, helping me adjust my direction when I'm off the track. And I would also like to thank my dear fellow interns, Jeff, Stefanie, Sarah, Pepijn, Linfeng, who have kept me company through all the gloomy rainy days and cheerful sunny days in the office.

Help from TUD also needs to be stressed: Prof. Sietsma, with his broad knowledge, sharp mind and warm heart, it is such an honor to work with him and discover my cans and cannots, I just wish he could be less busy though; Pina, who has the greatest patience to explain me the model; Kees and Nico, who introduced me to SEM and dilatometer, the most important experimental part of my work cannot process without their patient assisting. Thank Jing, for teaching me how to use latex, and left best memories with us. I would also want to thank all my friends from MSE, who fought along with me the whole time.

And also a special thanks to my GP, my physical therapist Erik, medical system and public transportation, Dutch government, for giving me this special experience of studying abroad and keeping me safe and healthy.

Finally, I would like to thank my family, my dearest friends who are dispersed all over the world, for supporting me unconditionally. And QC, for keeping me away from being an alcholholic.

# Contents

# 1 Introduction

Due to the energy crisis of recent years, the trend of materials used in the automotive industry has turned to lighter and stronger materials, requiring steels to achieve down-gauge while maintaining safety, this led to development of materials with higher strength. Among all the steel grades, high-strength steels (HSS) are the most prospective ones.

Special attention has been drawn to dual-phase (DP) steels, consisting mainly of ferrite and martensite, for its excellent combination between high strength and formability.

The manufacturing of cold rolled steel starts with casting, followed by hot rolling and reduced to a thickness of 3 - 5 mm. Then cold-rolled until the thickness is reduced to 1 - 2 mm. In order to obtain the final product, the cold-rolled product need to go through annealing, heating above $Ac_1$ yet bellow $Ac_3$, to get partial austenitization. During this process, heating rate can be of importance in obtaining the right steel grade properties. There are two ways of heating: RTF and flame heating, associated with different heating rates. Upon cooling austenite enriches in carbon, and as it cools below below bainite and martensite start temperature (Bs and Ms), austenite partially transforms into bainite and martensite, and the rest will be found as retained austenite in the final microstructure. During the heating process, recrystallization and recovery will also occur and may affect the final structure by affecting the formation of austenite. The final microstructure of the investigated material consists mainly of ferrite, retained austenite and martensite.

Apart from the composition and rolling parameters, the continuous annealing process can to a large extent determine the microstructure of the final product, including phase fractions and distributions, which will then determine the property of the product. Parameter of continuous annealing line includes, heating rate, annealing temperature, holding time, cooling rate, etc. Studies ([3][32][39][26]), have been carried out on the influence of heating rate and top temperature on the austenitization process, which is an important part of the continuous annealing. However, few studies have focused on the influence of heating rate on evolution of microstructure from full-hard state, and how this difference influence Austenite transformation.

Recent attentions have been drawn to computational techniques to simulate the process conditions of steel production. Modern applications demand more and more complicated composition and manufacturing of steels. Powerful modelling techniques can give a better insight of the process, which gives a better prediction, and provides an alternative of steel designing. Models as cellular-automata (CA) model and phase-field model are well developed, and have successfully reproduced similar results to experimental results.

The investigated DP800 steel has shown a large sensitivity to different heating rates during annealing. The aim of this work is to investigate heating rate influence on the evolution of the microstructure. Experimental approaches such as dilatometry and SE< are applied to investigate the evolution of the microstructure. A trial of CA model for recrystallization process, and phase-field model for austenite formation has carried out, to give a better insight of what is behind the phenomenon.

# 2

# Literature study

Upon heating during continuous annealing of cold rolled material, full-hard material first go through recovery, and above certain temperature recrystallization occurs. As temperature further increases above $Ac_1$ austenite phase transformation starts. There are two types of annealing: intercritical annealing and austenitic annealing. For intercritical annealing, the annealing temperature is chosen between $Ac_1$ and $Ac_3$, and the material is partially transformed into austenite. For austenitic annealing, annealing temperature is above $Ac_3$ and the material is fully austenite. During quenching, austenite will transform to martensite below martensite transformation temperature.

The final microstructure of a DP steel after continuous annealing process depends on several aspects, for example:

- Chemistry composition
- Start microstructure
- Heating rate
- Soaking temperature and soaking time
- Cooling rate, overaging temperature, etc...

Composition will thermodynamically determine the equilibrium ferrite/austenite ratio at intercritical temperature. The cold rolled reduction determines the dislocation density and the degree of pearlite degradation, which will also influence recovery and recrystallization of cold-rolled material. The start microstructure of cold rolled steel determines the distribution of carbon, and after heated above $Ac_1$ this difference may influence austenite formation mechanism. Heating rate determines the thermal energy provided to the whole system, by controlling nucleation and diffusion, it will strongly affect both recrystallization and austenitization. Soaking temperature and soaking time determines the ferrite/austenite ratio and grain size.

## 2.1. Microstructual evolution of cold-rolled DP steel

### 2.1.1. Continuous annealing process

There are seven stages of continuous annealing process (Figure 2.1): I. heating to the intercritical temperature region, II. soaking in order to allow nucleation and growth of austenite, III. slow cooling to quenching temperature, IV. rapid cooling to transform the austenite into bainite or martensite, V. over-aging, VI zinc-coating and VII. cooling.

The starting microstructure consists of elongated grains of ferrite and deformed colonies of pearlite after cold rolling, and this is called full-hard state (FH). The processes that occur upon annealing of a full-hard metal can be subdivided into three stages: recovery, recrystallization, and grain growth. Before strain-free grains appear, the release of stored deformation energy in the lattice is called $recovery$. Above a certain temperature $recrystallization$ starts, new nucleus show up and start to grow. When temperature reaches

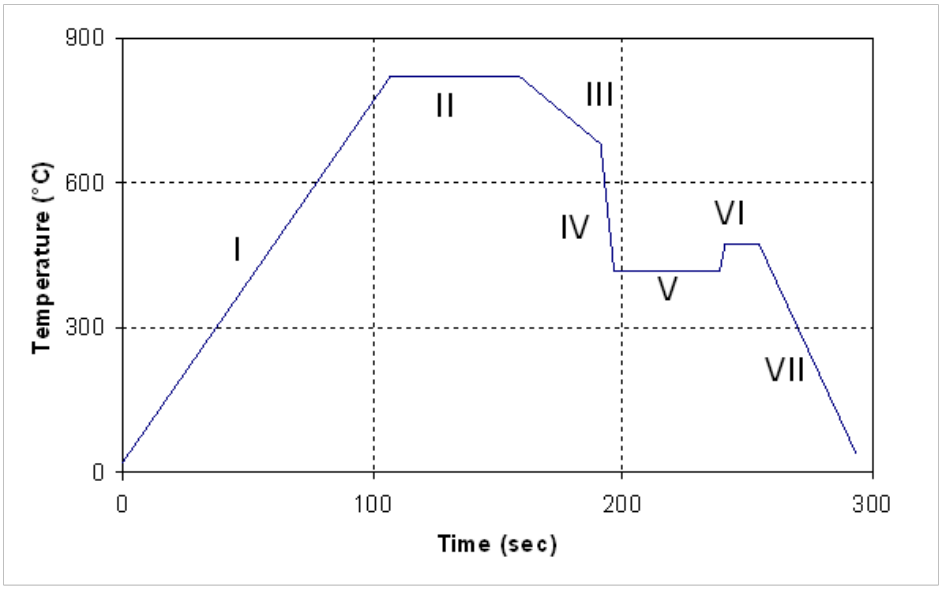


Figure 2.1: Schematic diagram of continuous annealing process.

$Ac_1$ austenite formation starts. At soaking temperature, the material is soaked for a certain time, and this is stage II. In this stage, austenite grains will further grow and reach towards equilibrium state, which is a diffusion process accompanied by carbon redistribution. During slow cooling, austenite partially transforms back into ferrite, resulting in austenite carbon enrichment. Fast cooling is then applied so that austenite transforms into bainite/martensite and forming a dual-phase microstructure (stage IV). Finally, the strip goes through over-aging for carbon enrichment, and is followed by zinc-coating and air cooling, giving additional martensite formation.

### 2.1.2. Thermodynamics of austenite phase transformation

The equilibrium phase at room temperature of steel consist of ferrite + pearlite. On heating a pro-eutectoid steel from room temperature to a two-phase region, phase transformation occurs. This consists of two stages: nucleation and growth. The driving force is given by the difference in the Gibbs free energy, $\Delta G$, between the initial and final states [7]. For a transformation from phase $i$ to phase $j$, the condition:

$$\Delta G = G^j - G^i < 0,$$

must be satisfied, in which $G^j$ and $G^i$ are the Gibbs free energy corresponding to the phases, and $\Delta G$ is the Gibbs energy difference. Figure 2.2[29] shows a schematic representation of the Gibbs free energy $G$ as a function of the carbon concentration at a temperature above the eutectoid temperature ($A_1$). At this temperature ferrite ($\alpha$) with composition $x_{\alpha\gamma}^{Ceq}$ (Figure 2.2 point 1) and austenite ($\gamma$) with composition $x_{\gamma\alpha}^{Ceq}$ (point 2) are in equilibrium. As indicated in Figure 2.2 (a), a maximum gain in Gibbs free energy ($\Delta G^{max}$) can be achieved by the formation of $\gamma$ phase with composition $x_{\gamma\alpha}^{Ceq}$. A significant enrichment of carbon must take place because of the big difference of carbon content between two phases. Figure 2.2 (a) also indicate that, besides a maximum reduction of Gibbs energy by formation of $\gamma$ with equilibrium condition, some decrease in the Gibbs free energy, although a smaller value, can also be achieved by forming of $\gamma$ with lower carbon content[29]. For example, Figure 2.2 (a) shows a reduction of $\Delta G^1$ by forming $\gamma$ with carbon content $x^1$, which is away from the thermodynamic condition.

Savran [29] summarized two possible situations of austenite formation upon heating. The first possibility is formation of $\gamma$ at $\alpha/\theta$ interface within the pearlite phase, schematically represented in Figure 2.3 (b). This process can be described as[29]:

$$\alpha_{x_{\alpha\theta}^{Ceq}} + \theta \rightarrow \alpha_{x_{\alpha\gamma}^{Ceq}} + \gamma_{x_{\gamma\alpha}^{Ceq}}$$

where $x_{\alpha\theta}^{Ceq}$ and $x_{\alpha\gamma}^{Ceq}$ are the equilibrium carbon concentrations in ferrite, changing with temperature according to lines QP and PG respectively (Figure 2.2 (b)); $x_{\gamma\alpha}^{Ceq}$ is the equilibrium carbon concentration in austenite, changing according to line SG. $\theta$ is cementite considered of a constant composition.

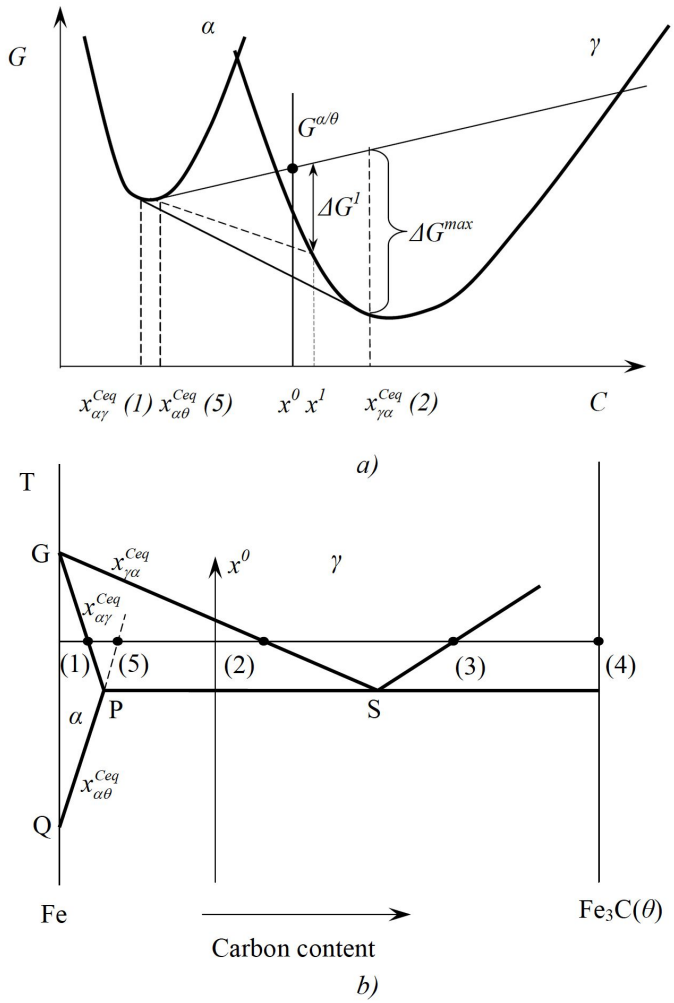


Figure 2.2: Schematic representation of the (a) Gibbs free energy G as a function of the carbon concentration in ferrite ($\alpha$), austenite ($\gamma$) and cementite ($\theta$) at a temperature above $A_1$, (b) metastable Fe-C phase diagram, indicating notations for the carbon atomic fractions. Numbers in brackets correspond to figurative points (1)-(5) in Figure 2.2, Figure 2.3. The solid thin lines in (a) represent the common tangent lines between $\alpha-\theta$ and $\alpha-\gamma$.

The second possibility is formation of $\gamma$ on $\alpha-\alpha$ grain boundaries (Figure 2.3 (c))[29], which can be described as[29]:

$$\alpha_{x_{\alpha\theta}^{Ceq}} \rightarrow \alpha_{x_{\alpha\gamma}^{Ceq}} + \gamma_{x_{\gamma\alpha}^{Ceq}}$$

The Fe-C phase diagram in Figure 2.2 (b) shows that the maximum carbon concentration in ferrite decreases with increasing temperature. This will lead to austenite nucleation at $\alpha-\alpha$ grain boundaries, and a contact with cementite is not necessary. Thus, both cementite and carbon rejected from $\alpha$ solid solution act as carbon source for austenite formation. Due to the difference in carbon solubility at the $\alpha/\theta$ and $\alpha/\gamma$ grain boundaries, a concentration gradient within the ferrite phase is present ($x_{\alpha\theta}^{Ceq} > x_{\alpha\gamma}^{Ceq}$, Figure 2.3 (c)). This creates the driving force for carbon diffusion towards $\alpha/\gamma$ grain boundary.

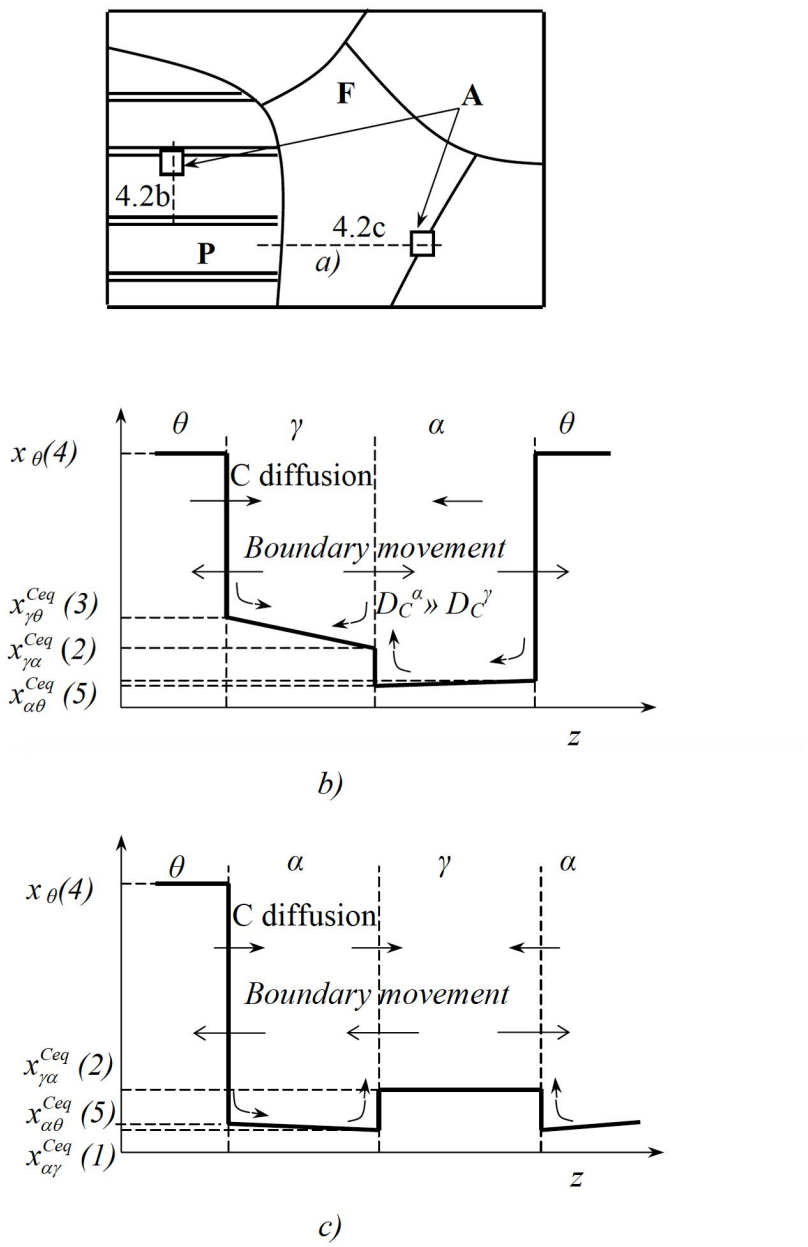


Figure 2.3: Schematic view of the microstructure (a) and variation of the carbon content across: (b) the cementite-austenite-ferrite and (c) the ferrite-austenite-ferrite boundaries. F = ferrite, A = austenite and P = pearlite.

To summarize, austenite nucleation is possible both in pearlite and at pro-eutectoid ferrite grain boundaries. However, the transformation will proceed at a much higher rate in pearlite than at $\alpha/\alpha$ grain boundaries, because of a shorter diffusion distance and the surplus of carbon that is available[29].

### 2.1.3. Recrystallization

Upon heating of a cold-worked metal, the evolution of microstructure can be subdivided into recovery, recrystallization, and grain growth[37]. The driving force at the first and second stage is the stored energy of the deformation, and the motion of dislocations and grain-boundaries are assisted by the thermal energy provided to the system.

In full-hard DP steels, recovery mainly appears as the decrease of dislocation density, sub-grain growth and increase of cell size. Above certain temperature, new strain-free grains will nucleate and this is the beginning

of recrystallization. At a certain temperature, when a new grain is nucleated, its radius will first increase linearly with time until it impinges another grain (Figure 2.4), and this can be described by $Johnson-Mehl-Avrami-Kolomogorov$ equation (JMAK theory) [37]:

$$R = G(t-\tau)$$

Where $R$ is the grain radius, $G$ is the linear growth rate, and $\tau$ is the incubation time.

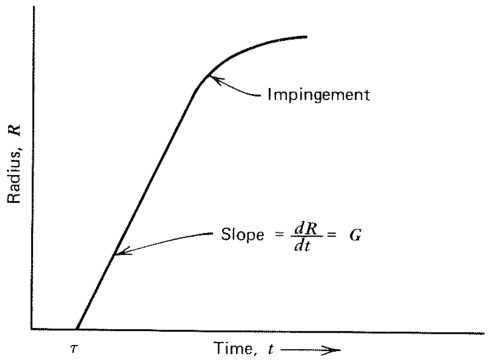


Figure 2.4: Time variation of radius of a new grain.

The nucleation rate $\dot{N}$ can be defined as:

$$\dot{N} = \frac{Numberofnuclei/timeunit}{Untransformedvolume}$$

The volume fraction ($X_r$) of recrystallized material can be governed by:

$$X_r = 1 - exp\left(-\frac{\pi}{3}G^3 t^4 \dot{N}\right)$$

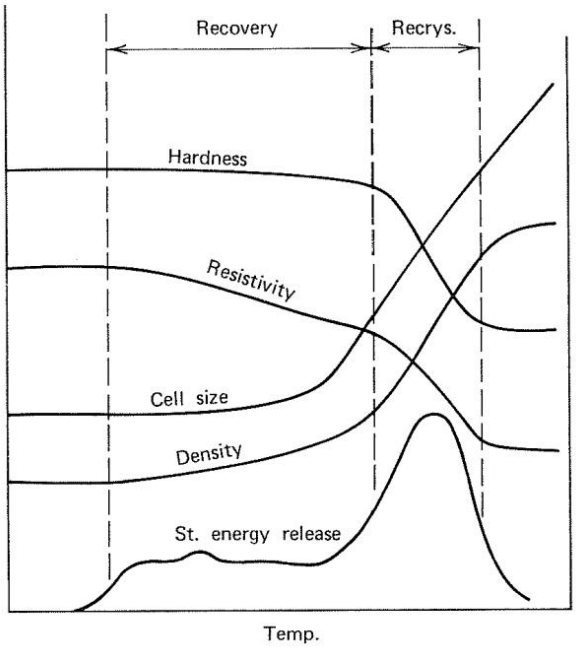


Figure 2.5: The change of properties upon heating of a cold-worked metal [37].

In continuous annealing line, the temperature changes with time, so the above situation cannot be applied. Both nucleation rate and growth rate are strongly affected by the heating rate. Whether the material is fully recrystallized or not (the fraction of the new grains, and the number and size of transformed grains before $Ac_1$), mainly determines the nucleation site of austenite and further influence the final microstructure.

As the temperature increases, the properties of the metal undergo several changes, demonstrated in Figure 2.5 [37]. According to those phenomena, the recrystallization process can be observed by several techniques, the most common ones are microscopy techniques, hardness measurements, and texture evolution measurements.

In a full hard material, ferrite grains are elongated and severely deformed, which will appear as long-thin colonies with blurry grain boundaries under microscope. Because of the high density of dislocation, substructures like cell-structures can be observed under electron microscope. While a recrystallized ferrite grain is always polygonal and without substructures.

As recovery is associated with the reconfiguration and annihilation of dislocations, and recrystallization is characterized by forming dislocation-free grains, the hardness of the material will decrease while the dislocation density decreases (Figure 2.5). Hardness measurement can also indicate the onset of austenite formation, since the austenite at high temperature will turn into martensite during quenching and increase the hardness. Petrov et al. [24] studied the recrystallization of a cold-rolled steel, with the composition 0.11C1.26Si1.53Mn. They chose an intercritical temperature of 800°C, and a heating rate of 10°C/s. Samples were quenched at multiple temperatures. They found that there are five distinct stages in the evolution of the hardness (HV3) as a function of quenching temperature (Figure 2.6). Stage I is the consequence of a strain-aging effect of the material, caused by the pinning effect of carbon atoms and small carbide precipitates on the dislocations. Stage II reveals the recovery process triggered by the coarsening of the small carbides. Before the actual static recrystallization, there is a transition stage from recovery to recrystallization (stage III). The start of primary recrystallization is determined by the drop in hardness between stage III and stage IV. The primary recrystallization can overlap with the recovery process. For this material, above 754°C([24]) austenitization starts, and the hardness is increased by the increasing volume of martensite in the quenched material.

Texture evolution can also reveal recrystallization in cold-rolled materials. This is because when full-hard strips are annealed till recrystallization starts, new grains usually have a crystallographic preference, resulting in a texture. High-temperature XRD for example, provides an insight to the texture evolution as temperature increases or decreases. When a new, strong texture appears in the material, it usually indicates the recrystallization process.

When the strongly deformed ferrite grains start to recrystallize, the as-well deformed pearlite colonies will also degenerate. Studies([39],[30]) have found this appears as the dissolving of lamellar pearlite structures and spheriodizing of the cementites. This process can determine the distribution of carbon before phase transformation, and can strongly affect austenitization, since carbon enrichment is the key of austenite formation in steel.

### 2.1.4. Austenitization

In order to achieve a dual-phase structure, the material is heated to the intercritical temperature region, and partially transformed into austenite. This results in a thermodynamically restricted composition of both austenite and ferrite. A partitioning of alloying elements between those two phases has to occur, mainly by diffusion and redistribution of carbon. Studies[32][30][39] have delineated the process of intercritical austenitization of a typical ferrite+pearlite starting microstructure steel into three distinct stages:

(i) A rapid growth of austenite into pearlite until complete pearlite dissolution;

(ii) A slow growth of austenite into ferrite;

(iii) Slow equilibrium of ferrite and austenite.

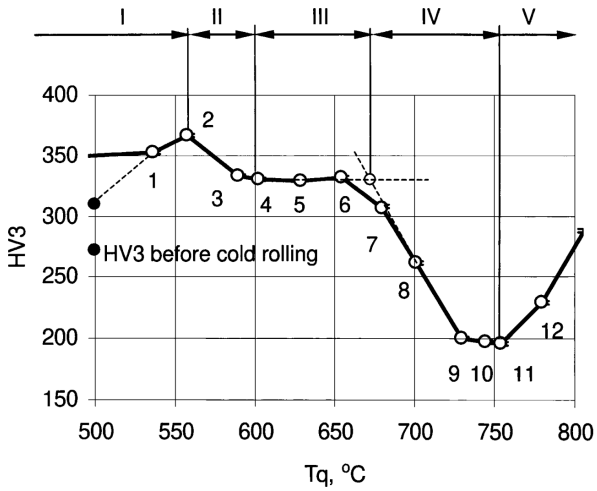


Figure 2.6: Hardness HV3 as a function of the quench temperature. Petrov et al.[24].

During the process carbon diffusion has been proposed as the controlling step in the reaction, since a higher carbon concentration is required for austenite formation.

Speich et al. [32] studied three typical Fe-C-Mn DP steels with different carbon content, all samples started from fully-recovered non-banded ferrite + pearlite microstructure before intercritical annealing. According to their observations, they proposed the three stages of austenitization. At the beginning of the first stage, austenite nucleates at the interface between ferrite and cementite within a pearlite colony and grows inward. The nucleation occurs instantaneously without nucleation barrier, and that nucleation is not the rate-limiting factor[31]. As the diffusion distance (half the thickness of the pearlite lamellar) is considerably small, this process proceeds rapidly. The time needed for complete pearlite dissolution depends on the carbon content and intercritical temperature. At the end of this stage, a high-carbon austenite is generated, which is not in equilibrium with ferrite. According to the author, the second stage can either be determined by the diffusion of carbon or the substitutional diffusion of manganese, depending on the temperature. The third stage of final equilibrium is proposed to be controlled by the slow diffusion of manganese in austenite and can take up to 2000 to 4000 h.

Apart from the original pearlite colonies, Souza et al.[30] have found that nucleation at ferrite-ferrite grain boundaries is also possible (Figure 2.7) for a steel with composition 0.14C1.59Mn0.41Si0.041Nb. Unlike Speich et al.[32], who believed that grain boundaries can act as diffusion channels for Mn and accelerate the transformation, Souza proposed the pre-existing particles (carbides, nitrides, or carbon nitrides) on the grain-boundaries are the reason for the possibility of austenite nucleation.

Yi et al.[39] studied an 0.04C2.2Si1.8Mn steel with four different starting microstructures (Figure 2.8), to investigate the effects of starting microstructure on the formation of austenite during intercritical annealing. A heating rate of 5 °C/s was applied. Their results revealed that before austenite formation, the microstructure of all samples has changed, cementite has all gone trough some extent of spheriodization. Similar nucleation phenomena were found in Ferrite-Pearlite-1 (FP-1) and Martensitic-2 (MT-2) structure (Figure 2.8), where austenite preferably nucleates at the ferrite-ferrite grain boundaries. Martensitic-1 (MT-1) showed an acicular morphology, where austenite reveals a quasi-lamellar array along the trans-granular boundaries. In the case of Ferrite-Pearlite-2 (FP-2), since pearlite is not completely dissolved before austenitization, austenite nucleated primarily on the pearlite colony boundaries.The change of austenite volume fraction according to the temperature is illustrated in Figure 2.9. Since temperature is linearly increasing with time, this graph can be qualitatively related to the formation rates. Except MT-1, all three samples experienced the same formation rate at the start stage, but went to a lower rate when the volume fraction reached around 25%. This implies that the kinetics of all three samples are identical during the first stage. They argued that, the most favourable site for austenite nucleation should be the one where the nucleation is energetically favourable,

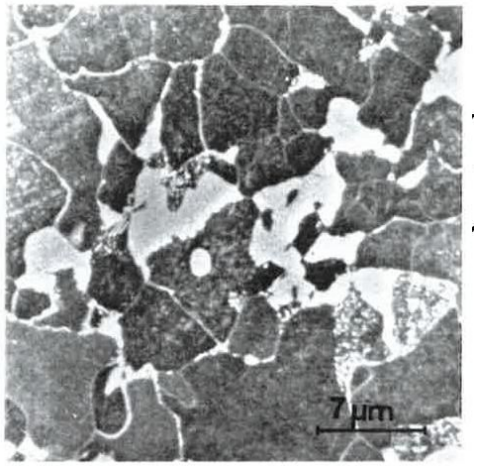


Figure 2.7: SEM Souza et al.[30], intercritically annealed at 740°Cfor 1 min. Notice the preservation of original ferrite-pearlite interfaces and austenite nucleation at particles located at ferrite boundaries. One also sees a fragmented $\alpha$-$\gamma$ interface, indicating slow growth normal to the interface.

and where the carbon atoms are available to satisfy the solubility limits of austenite. In addition, it is known that carbon diffusion is faster at the grain boundaries than through the bulk, and the grain boundaries also provide a lower distortion energy caused by the new phase. Hence, austenite preferably nucleates at the grain boundaries where there is access to cementite carbides. When all the favourite sites along grain boundary are saturated with austenite areas, the diffusion channel is no longer effective, and the volume diffusion of carbon into austenite may be the limiting factor, and this is why the austenite fraction shows a plateau. They proposed a diffusionless mode of austenite growth at this slow-growing stage, a Widmanstätten growth, and this type of growth may increase the austenite volume fraction more rapidly since the pointed interface may collect carbon atoms more effectively.

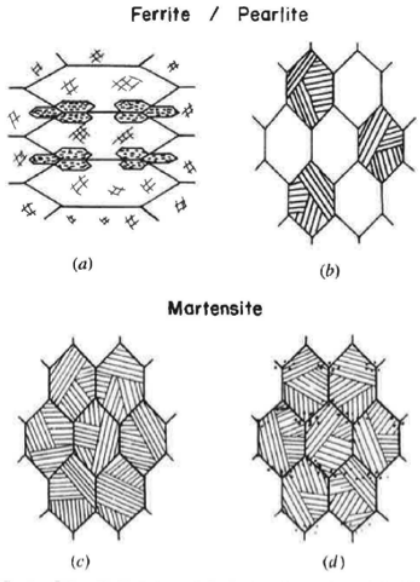


Figure 2.8: Schematic illustration of the starting microstructures of Yi et al.: (a)Full hard material, elongated ferrite + pearlite (FP-1); (b)Fully recovered ferrite + pearlite (FP-2); (c)Fully martensite microstrucuture (MT-1); (d)Fully martensite microstructure with part of the carbon sphereiodized (MT-2).[39]

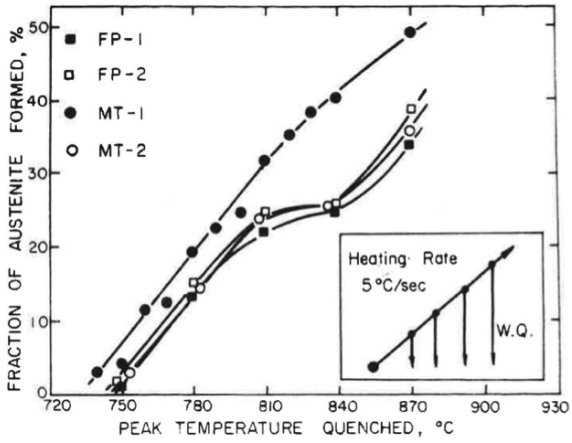


Figure 2.9: Variation of austenite volume fraction of each sample upon heating to intercritical temperature[39].

Rocha et al. [26] studied three different continuous annealing routes and their effect on a cold-rolled DP steel, with the composition of 0.08C1.91Mn. The microstructure after each stage during the process is quenched and observed under SEM (Figure 2.11). The design from route 1 to route 3 is demonstrated in Figure 2.10. From the microscopy pictures, all austenite colonies distribute along the ferrite, which suggests that the formation of austenite islands took place after the complete recrystallization of ferrite. Thus all three samples have completed recrystallization before soaking. They discovered that the volume fraction of austenite and its coarseness increase with increasing soaking temperature and time (Figure 2.11, comparing between the pictures horizontally). Hence, a higher heating rate and shorter soaking time leads to a finer austenite distribution. After soaking, austenite constituents increase further in size, and the microstructure becomes more homogeneous (Figure 2.11 (d) to (f)). After slow cooling, part of the austenite transforms back into ferrite, but the extent to which this transformation also depends on the annealing route parameters (heating rate, soaking time, soaking temperature, slow cooling rate, etc.).

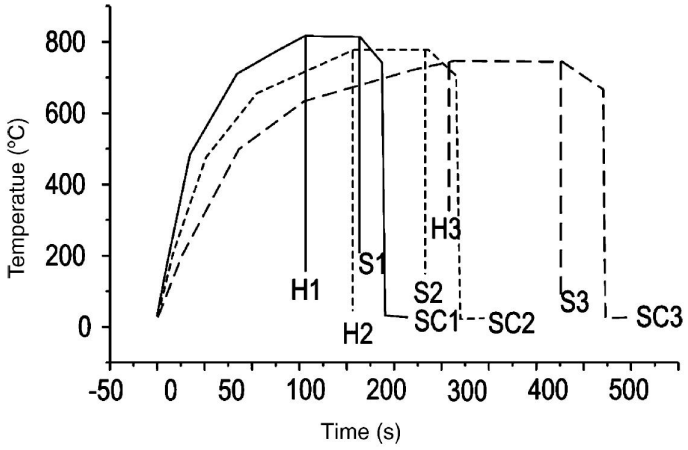


Figure 2.10: Schedule of the annealing processing simulation, route 1 to 3 marked with 1-3. H, S, and SC represent heating, soaking, and slow cooling steps, respectively.[26]

Savran et al.[29] studies four kinds of C-Mn steel with different carbon content and their influence on austenite formation. The start microstructure is a mixture of ferrite and pearlite, with different fractions. She argued that there are two carbon sources for austenite formation: the pearlite areas, and the pro-eutectoid ferrite itself, since the equilibrium carbon content of ferrite is lower after phase transformation. With the latter one, nucleation of austenite is possible at ferrite grain boundaries, and the contact with cementite is not necessary. With Electron probe micro-analysis (EPMA) measurements, they discovered that there is significant variation

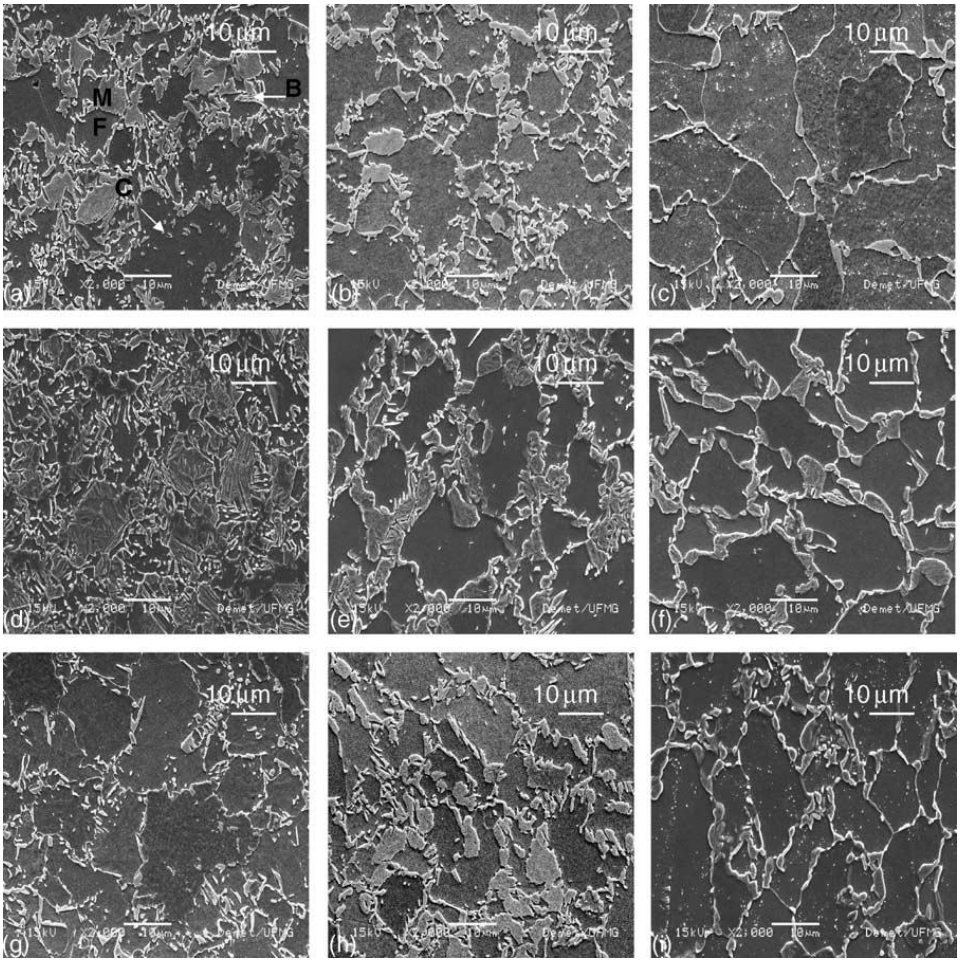


Figure 2.11: SEM micrographs of samples after various processing routes by Rocha et al. [26]: After heating: (a) Route 1, (b) Route 2, (c) Route 3; After soaking: (d) Route 1, (e) Route 2, (f) Route 3; After slow cooling: (g) Route 1, (h) Route 2, (i) Route 3. Ferrite - F; Carbide - C; Bainite - B; Martensite - Austenite - M.

in carbon content in austenite nucleated on the ferrite-ferrite grain boundaries (low-carbon austenite) and the one nucleated on pearlite-ferrite boundaries (high-carbon austenite). They also found that there is a delay between austenite formation and cementite dissolution, according to the observation that there is still cementite plates visible within martensite after quenching.

### 2.1.5. Interaction between recrystallization and austenitization

Over the years, the mechanism of austenite formation during annealing process has been studied from different perspectives on various type of steels. The influence of carbon content, heating rate, soaking temperature, and holding time has also been investigated (see discussion subsection 2.1.4). This is of special interest for high-strength steels, as modern steels urge for higher strength yet better formability. This involves a more delicate alloying recipe and a carefully-controlled heat treatment. As production lines develop and various conditions are adjusted, special attention has been drawn to the interaction between recrystallization and austenite formation. This is because a large sensitivity has been found of the final product, resulting from this interaction during the annealing process.

Mumford et al. [23] studied the effects of heating rate, soak temperature and cold reduction upon recrystallization. They discovered that increasing heating rate will suppress recrystallization, indicated by the hardness profile (Figure 2.12). This effect is highlighted by comparing the microstructures of highest and lowest heating rates (Figure 2.13). It is clear that the sample heated with 2°C/s is fully recrystallized at this temperature, which corroborate with the "plateau" at the minimum, in the hardness profile (Figure 2.12). However, for

the sample with heating rate of 200°C/s, recrystallization has been suppressed, judged by the fact that the microstructure still consist mostly of deformed ferrite grains. This means it is possible to suppress recrystallization into intercritical temperatures by using higher heating rates. This suppression is not seen for the austenitization behaviour, so that it is possible to vary the extent to which recrystallization and transformation overlap. By applying a low heating rate (2°C/s), recrystallization is complete prior to the onset of transformation, and that significant dissolution of cementite has occurred. They agreed with Roberts & Mehl ([25]), that the time required for the transformation of spheroidized pearlite to austenite is significantly larger than that seen for pearlite with a lamellar structure. This effect is a result of the relative distance over which carbon has to diffuse. By applying a high heating rate (100°C/s, 200°C/s), recrystallization is severely suppressed. The amount of carbon in ferrite solution is severely reduced, because of the limited time for carbon to diffuse away from its high concentration within the pearlite colonies. The austenite will preferably nucleate at pearlite colonies, driving the formation of bands. As for recrystallization in this case, recrystallization nucleus can develop between the austenite bands. Once initiated, the growth rate can be rather high because of the high driving force for recrystallization, forming large grains between bands. When the grains are growing, the boundaries do not provide suitable sites for nucleation of austenite [14].

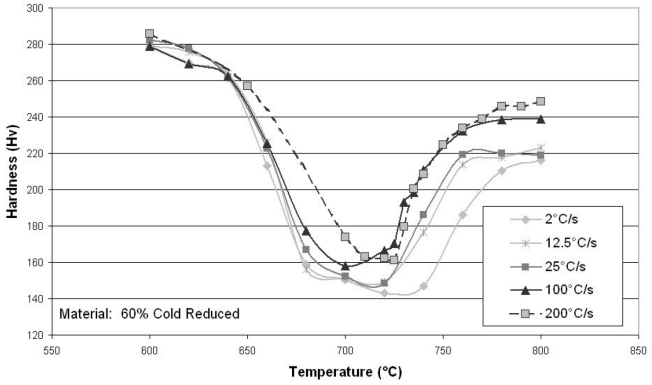


Figure 2.12: Recrystallization/transformation hardness profile by [23].

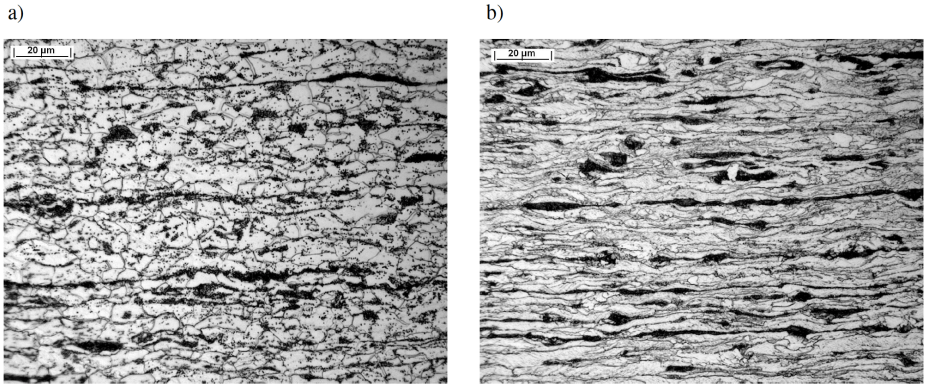


Figure 2.13: Micrographs of samples heated to 735°Cwith heating rates of (a) 2°C/s and (b) 200°C/s, which were quenched immediately[23].

Barbier et al. [3] studied the interaction between recrystallization and austenite formation at different temperature, by applying the same fast heating rate 100°C/s and holding at different temperatures. They discovered that the kinetics of ferrite recrystallization is strongly affected by the formation of austenite and can be even inhibited in some cases. In Figure 2.14, red lines indicates the fraction evolution of austenite, green lines for recrystallized ferrite, and blue lines for un-recrystallized ferrite. Below $Ac_1$, when no austenite is formed, recrystallization is finished only in one minute, while above $Ac_1$ (715°C), in the presence of austenite and

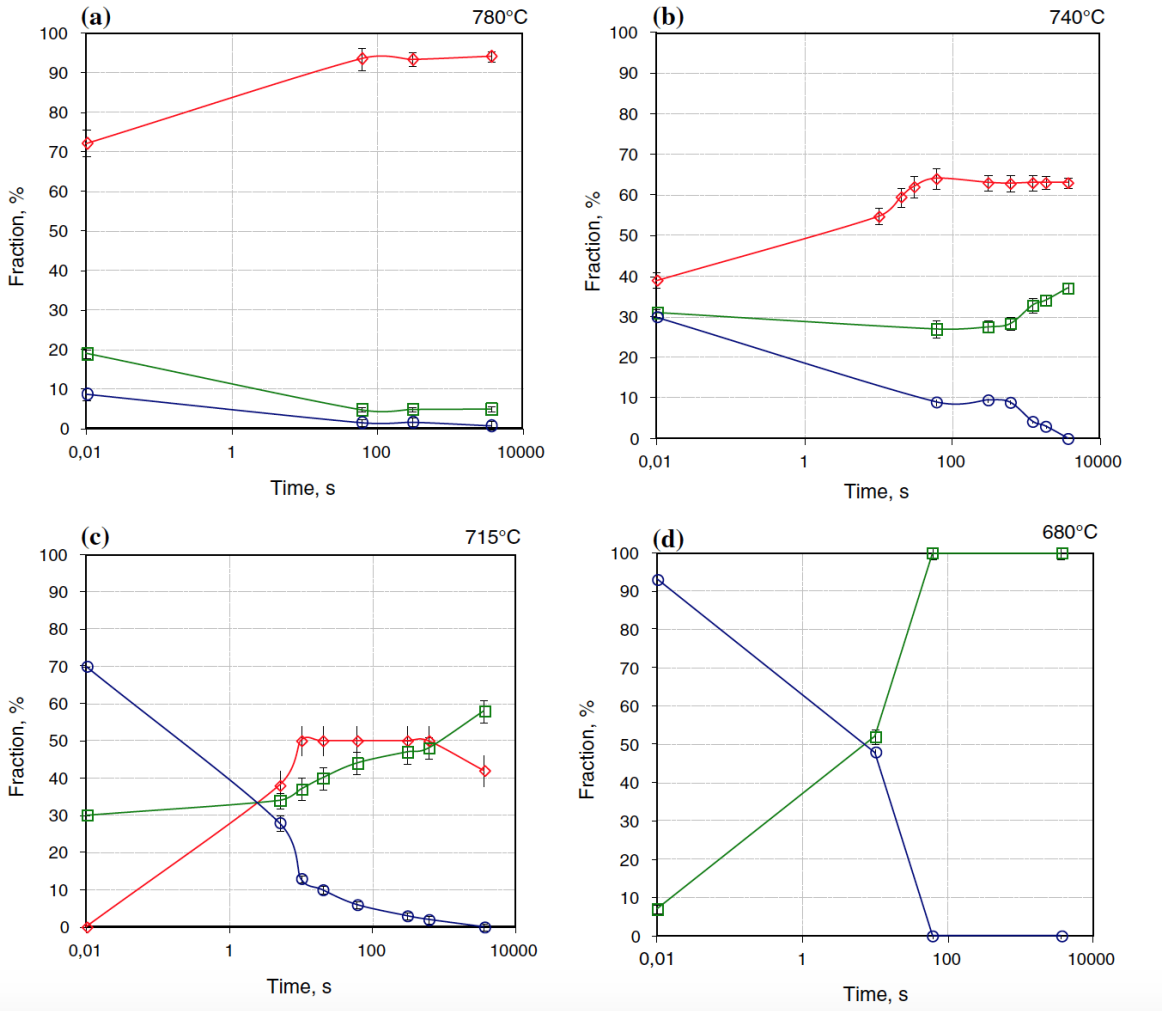


Figure 2.14: Evolution of the different phase fractions during isothermal annealing at different temperatures after repid heating (100°C/s) (a) 780°C, (b) 740°C, (c) 715°C, (d) 680°C[3]. Red lines indicates austenite, green for recrystallized ferrite, and blue for un-recrystallized ferrite.

despite a higher driving force, some deformed ferrite is still detected in the microstructure even after 5 min. Above $Ac_1$, after nucleation, austenite grains can grow very fast, and those grains act as pinning obstacles for the moving boundaries between deformed and recrystallized ferrite. Strong microstructure heterogeneity and anisotropy can result from the competitive growth of austenite and recrystallized ferrite. At higher temperatures, high amount of austenite results in finer and more homogeneous microstructures.

Andrade-Carozzo et al. [1] studied the influence of different heating rate and holding time on the interaction between recrystallization and austenite formation, on a cold-rolled Nb-added TRIP-aided steel. They discovered that by increasing the heating rate, a finer microstructure can be achieved. They proposed that deformation defects become prior potential nucleation sites for austenite at the expense of ferrite recrystallization, and that this distributed fine austenite can stabilise the deformation structure and hinder ferrite recrystallization. The added niobium retards recrystallization, but the same effect does not apply to austenite formation.

Huang et al. [14] studied the austenite formation during intercritical annealing, by applying different cold reduction and by adjusting different heating rates. They observed that the cold reduction will break down the lamellar pearlite structure, which will inhibit spheriodization of cementite in the upcoming heat treatment. They also discovered that, by applying a fast heating rate (100°C/s), the ferrite is still recrystallizing when austenite has nucleated in the pearlite colonies and starts to grow from there. These moving ferrite grain

boundaries do not provide suitable nucleation sites for austenite, leading to a lack of austenite present on ferrite-ferrite grain boundaries in the final microstructure.

### 2.1.6. Transformation temperature of Austenite into Martensite

Upon quenching austenite from high temperatures, due to the limited time for carbon to diffuse and form pearlite, the structure will go through martensite transformation. The temperature under which the transformation happens is called martensite transformation temperature (Ms). The most accepted theory of martensite transformation is proposed by M. C. Bain in 1924 [37]. He proposed a diffusionless transformation from fcc structure of austenite into bct structure (martensite), in which case carbon is trapped in the lattice (Figure 2.15). As a result, the shear deformations produce large numbers of dislocations, which is a primary strengthening mechanism of steels.

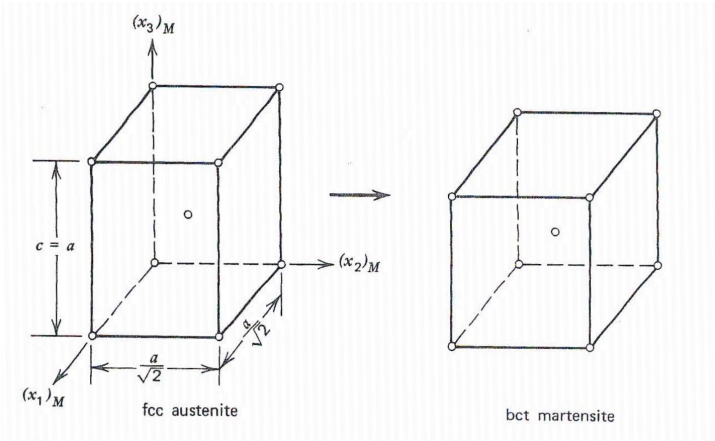


Figure 2.15: Bain's theory of martensite transformation[37].

There are many factors that can influence the martensite transformation temperature. In this thesis, three main factors are taken into account: carbon content, austenite grain size, segregation of alloying elements.

Many studies have tried to quantify the influence of alloying elements on the phase transformation temperatures ([2][9][21]). They provided equations of Ms accordingly as follows:

$$Ms = 539 - 423C - 30.4Mn - 17.7Ni - 12.1Cr - 11.0Si - 7.0Mo \text{[2]}$$
$$Ms = 550 - 350C - 40Mn - 35V - 20Cr - 17Ni - 10Cu - 10Mo - 8W + 15Co + 30Al \text{[9]}$$
$$Ms = 539 - 423C - 30.4Mn - 7.5Si - 30.0Al \text{[21]}$$

In the equations, each element symbol represents the weight percentage (wt %) of the corresponding element. Both carbon content and the influence of substitutional elements are taken into account in these equations. The biggest influence is caused by the difference in carbon content, and both increasing the local carbon content and the substitutional elements concentrations can increase the martensite transformation temperature.

Apart from composition, the martensite-start temperature also depends on the austenite grain size[38]. One argument is that refinement of austenite grain size leads to Hall-Petch strengthening of austenite, and making it difficult for martensite to form[6]. By providing a greater resistance to the motion of dislocations, solid-solution strengthening affects the nucleation of martensite and bainite. Hence, with a larger austenite grain size, it becomes easier for martensite transformation, and the Ms increases correspondingly.

An alternative explanation in the case of highly alloyed steels is based on a burst phenomenon. In this case, a large fraction of the austenite transforms into martensite within a very small temperature interval. As the austenite grain size decreases, the tendency for a burst to occur decreases[10]. However, most martensitic

steels do not under go bursts of transformation, especially those that have a low alloy content and form lath-like martensite[38].

The gradual increase in the fraction of martensite as a function of under-cooling below Ms temperature follows the classical $Koitinen-Marburger$ equation[19], as follows:

$$V_\gamma = exp[-1.10\times10^{-2}(M_s - T_q)]; \tag{2.1}$$

$$M_s > T_q > -80^\circ C \tag{2.2}$$

where $V_\gamma$ is the fraction of retained austenite, and $T_q$ is the lowest temperature reached during quenching.

## 2.2. Modelling of solid state transformation in steel

The increasing demand of stronger and more formable steels requires more and more complicated metallurgy processes. Processes throughout the production chain, from hot strip mill to continuous annealing lines, can strongly influence the final microstructure, and consequently the mechanical properties. The interaction between the various metallurgical processes such as recrystallization and phase transformation makes it difficult to identify the relation between direct process settings, such as time temperature profiles, and the final product properties. Thus, a computational model that can reveal the microstructure evolution under variable conditions is very necessary. These modelling tools can help in understanding the underlying physical principles, and may further lead to the development of new grades of steel. This chapter will introduce the basic thermodynamic and kinetics conditions for most typical modelling methods, together with the basic principles of two most promising models: cellular-automata (CA) model, and phase-field model.

### 2.2.1. Transformation thermodynamics and kinetics applied in modelling

In Fe-C steels, two main distinct phenomena occur during transformation: (a) the carbon partition between ferrite ($\alpha$) and austenite ($\gamma$), influenced by the carbon diffusion; (b) the construction of fcc ($\gamma$) lattice from bcc ($\alpha$) lattice, indicated by the interface mobility. In the literature, the transformation from bcc lattice to fcc lattice is often considered to be fast enough and not to affect the transformation kinetics, and that carbon diffusion is the rate controlling process. Under this condition the carbon concentration in $\alpha$ and $\gamma$ at the interface at anytime of the transformation are equal to equilibrium concentrations (local equilibrium). This is then called *diffusion controlled* transformation. The other extreme is that carbon diffusion is considered to be fast enough through lattice, and that the carbon concentration is homogeneous in each phase and equal to equilibrium. In this case the rate controlling step is the lattice transformation, and is said to be *interface controlled* transformation.

In reality both carbon diffusion and the lattice transformation influence the transformation kinetics, which behaves as a *mixed-mode* transformation. In the mixed-mode approach, the interface velocity, $v$, can be formulated by:

$$v = \mu\Delta G^{\alpha\gamma}(x_\gamma^C, x_\alpha^C), \tag{2.3}$$

where $\mu$ is the intrinsic interface mobility. The driving pressure for the interface migration, $\Delta G^{\alpha\gamma}(x_\gamma^C, x_\alpha^C)$, is calculated from the difference of Gibbs free energy between $\alpha$ and $\gamma$ across the interface, depending on the transient local carbon composition at the interface in the $\gamma$ and $\alpha$ side $(x_\gamma^C, x_\alpha^C)$. The carbon concentrations at the interface, $x_\gamma^C$ and $x_\alpha^C$, change with time during transformation [20], due to the finite interface mobility and the non-zero net carbon flux at the interface. The interface mobility is given by an Arrhenius type equation:

$$\mu = \mu_0 e^{\frac{-Q_G}{RT}}, \tag{2.4}$$

where $\mu_0$ is the pre-exponential constant and $Q_G$ is the activation energy for interface movement.

In a binary Fe-C system, the equilibrium condition between ferrite and austenite is well-defined at a given temperature and pressure. For a diffusion controlled transformation under atmosphere pressure, the interfacial composition at he $\gamma/\alpha$ interface at a given temperature can be obtained from the Fe-C phase diagram. However, in the mixed-mode approach, the finite interface mobility will affect the interfacial composition.

The carbon concentration of ferrite increases continuously from the bulk concentration ($x_0^{Ceq}$) to the equilibrium value ($x_{\alpha\gamma}^{Ceq}$) as the transformation proceeds.

In modern industrial steels, substitutional alloying elements, such as Mn, Ni, Si, Al, Cr, etc, are always added to improve the properties of the steel. These substitutional alloying elements may also influence the equilibrium condition of the model. Different types of growth kinetics can be distinguished, depending on the redistribution behavior of the substitutional elements: local equilibrium (LE), paraequilibrium (PE), and local equilibrium with negligible partitioning (LENP) [12][11][15].

Under LE conditions, the substitutional elements are assumed to be redistributed. Therefore, the transformation is also controlled by the slow diffusion of the substitutional elements. Due to the slow diffusion rate of substitutional elements, transformations under LE may take many hours or even days. LE is usually applied for very small heating or cooling rates.

LENP can be regarded as a special case of LE: if the driving force for phase transformation is high enough, the interface can move without being limited by diffusion of the substitutional elements. Because of the high transformation velocity, no partitioning is observed on the microscale. This is a very typical scenario for technical processes.

For PE process, only the contribution of the fast diffusing interstitial elements (C) is taken into account for the calculation of transformation kinetics. This indicates that the substitutional elements are assumed to be undisturbed by the passing of the interface, and that the equilibrium with respect to these elements cannot be attained across the interface. Three conditions are applied at the interface:

- Equal ratio of alloying elements to Fe on both sides;
- Equal chemical potential of carbon on both sides;
- Equal chemical potential of weighted average of Fe and alloying elements.

Mathematically, these conditions can be described as:

$$\mu_C^{\gamma} = \mu_C^{\alpha} U_i \cdot (\mu_i^{\gamma} - \mu_i^{\alpha}) = -U_{Fe} \cdot (\mu_{Fe}^{\gamma} - \mu_{Fe}^{\alpha}), \tag{2.5}$$

where $U_i$ refers to the site fraction of element $i$ defined as $\frac{x_i^0}{x_i^0 + x_{Fe}^0}$. The driving force under PE is governed only by the carbon diffusion, and the interface conditions can be obtained by solving the diffusion equations for carbon in both $\alpha$ and $\gamma$, together with the mass balance of carbon at the the interface, and the above Equation 2.5. Unlike LE conditions, transformation under PE can finish in seconds.

### 2.2.2. Sharp-interface model (Cellular automata model)

In order to provide a desired quantitative link between process settings and final product microstructure, an integrated microstructure evolution model as cellular automata (CA) microstructure evolution model is introduced. This model includes a description of ferrite recrystallization, austenite formation from pearlite and ferrite, and austenite decomposition. By including local information from the grid, it is possible for CA model to start from any realistic microstructure. Compared with other models, the computational efficiency of this model makes it possible to run simulations for many different process settings and compositions within a reasonable timescale. Thus, this model is capable of three-dimensional (3-D) descriptions of the microstructure for a sufficiently large system size.

#### Theory

In the CA-model used in the present work, the simulated polycrystalline system is discretised in a 3-dimensional (3D) grid of cubic cells of dimension $\delta$[4]. Each cell in this system has 26 neighbouring cells, at distances $\delta$, $\sqrt{2}\delta$ and $\sqrt{3}\delta$. In the applied CA-models in this work transformation takes place at grain boundary cells according to the sub-models, and he state of each cell changes accordingly. At each time $t$, each cell has the following properties:

- The grain to which the cell belongs. The setting of this property for each cell of the system identifies univocally the *grain boundary cells*, which have neighbours that belong to a different grain. Note that each cell belongs to only one grain, for this reason, this model is a sharp-interface model.
- The growth length, $l^i_{cell}$. for each grain boundary cell, $i$. This property is updated every time step, $\Delta t$, by Euler time integration of the grain boundary velocity, i.e.

$$l^i_{cell}(t+\Delta t) = l^i_{cell}(t) + v^i_{cell}\Delta t \tag{2.6}$$

  where the velocity $v^i_{cell}$ is equal to the grain boundary velocity, $v$, which is calculated according to the relevant sub-model (see later sections).

When the growth length of a cell, $l^i_{cell}$ has reached the grid spacing $\delta$, the nearest neighbor cells are transformed into interface cells and their growth length starts to evolve according to Equation 2.6. Next-nearest neighbours are transformed when $l^i_{cell}$ exceeds the face diagonal of the cubic cell, i.e. $l^i_{cell} \geq \delta\sqrt{2}$, and the last neighbours are transformed when $l^i_{cell}$ exceeds the body diagonal of the cubic cell, i.e. $l^i_{cell} \geq \delta\sqrt{3}$. When all its neighbour cells have been transformed, a cell is no longer a grain boundary cell and its growth length $l^i_{cell}$ loses its meaning. When cells of different grains grow simultaneously into a shared neighbour cell, the same first cell that reaches the critical length determines to which grain the shared neighbour cell transforms.

To ensure that every change in the grain volume and surface area is directly reflected in the transformation kinetics, the maximum time step size, $\Delta t$, is subjected to the criterion:

$$\Delta t < (\sqrt{3}-\sqrt{2})\delta / v \tag{2.7}$$

in the present cubic cell configuration. On the basis of Equation 2.7 the time step is selected dynamically during a simulation. Equation 2.7 shows that the maximum allowed time step depends on the grid spacing ($\delta$) used in the simulation.

In CA model, the cells form grains. Grains have a number of properties:

- The phase of the grain (ferrite, austenite or pearlite);
- Strain energy;
- Average carbon concentration;
- Carbon concentration at the interface.

For all growing grains the grain boundary velocity, $v$, is determined according to the classical equation:

$$v = M\Delta G \tag{2.8}$$

where $M$ is the interface mobility and $\Delta G$ the driving force for the transformation[8].

For different metallurgical processes (ferrite recrystallization and phase transformations) that occur, different sub-models are used for the calculation of the driving force $\Delta G$ in Equation 2.8.

### Ferrite recrystallization

The nucleation of recrystallized grains can be described as site-saturation, which can be interpreted as a collection of pre-existing nuclei that start to grow when a certain temperature is reached. This is implemented as a nucleation density $n_{RX}$ and a nucleation temperature $T^{nucl}_{RX}$, which are input parameters. The number of nuclei formed, $N_{RX}$, is given by:

$$N_{RX} = \sum_i n_{RX} V^i_\alpha, \tag{2.9}$$

where $V^i_\alpha$ is the volume of a single non-recrystallized ferrite grain. The positions of the nuclei in the grains are chosen randomly.

For recrystallized-ferrite growth, the grain boundary velocity, $v$, can be described by:

$$v = M_0^{\alpha\alpha} exp(-Q_g^{\alpha\alpha}/RT)\Delta G_{RX} \tag{2.10}$$

where $M_0^{\alpha\alpha}$ and $Q_g^{\alpha\alpha}$ are respectively the pre-exponential factor and the activation energy for the grain boundary mobility and $\Delta G_{RX}$ is the strain energy of the non-recrystallized grains. The newly nucleated grain is assumed to have zero strain energy. The growth velocity, $v$, depends on the strain energy of the neighbouring grains and is calculated locally. If all deformed grains have the same strain energy, $v$ calculated with Equation 2.10 is the same for all interface cells. If deformed grains have different strain energies and neighbouring cells of a given interface cell belong to different grains (e.g. on a triple point), the highest strain energy among the neighbouring grains is used in the calculation of the interace velocity. In this way it is also possible to apply a strain energy profile to the microstructure in this model.

### Austenite transformation

The nucleation of austenite is described as site-saturation, in a similar way to ferrite recrystallization. The limitation of this model is that austenite can only nucleate in pearlite grains.

The austenite growth rate from pearlite is described by:

$$v = M_0^{\gamma P} exp(-Q_g^{\gamma P}/RT)\Delta G_{\gamma P}. \tag{2.11}$$

In this model, pearlite is treated as a single phase, and only transforms in a small temperature range, therefore the pearlite-to-austenite driving force $\Delta G_{\gamma P}$ can be considered as a constant. $M_0^{\gamma P}$ is the pre-factor, and $Q_g^{\gamma P}$ is the activation energy for the interface mobility. All three factors are input parameters.

The austenite growth into ferrite grains is based on an interface-controlled model, where the interface velocity is calculated by:

$$v = M_0^{\gamma\alpha} exp(-Q_g^{\gamma\alpha}/RT)\Delta G_{\gamma\alpha}(x_c^{\gamma,h}) \tag{2.12}$$

where $M_0^{\gamma\alpha}$ and $Q_g^{\gamma\alpha}$ are the pre-exponential factor and the activation energy for the interface mobility. The driving force, $\Delta G_{\gamma\alpha}$, is calculated based on the average austenite carbon concentration, $x_c^{\gamma,h}$, given by:

$$x_c^{\gamma,h} = \frac{x_0 - f_\alpha x_C^{\alpha,eq} - f_P x_C^{P,eq}}{1 - f_\alpha - f_P} \tag{2.13}$$

where $x_0$ is the overall carbon concentration in the steel, $x_C^{\alpha,eq}$ and $x_C^{P,eq}$ are the equilibrium carbon concentration in ferrite and pearlite, and $f_\alpha$ and $f_P$ are the ferrite and pearlite fractions. The advantage of this approach is that the correct equilibrium phase fraction can always be attained.

### Previous applications of Sharp-interface model

Due to the computational efficiency of CA model, it is usually applied in 3D simulations. By starting from realistic microstructures, effective microstructure simulation can be achieved since aspects of the initial microstruture are maintained during intercritical annealing.

Bos et al.[4] applied a 3D CA model on simulating microstructure evolution of a 0.45C1.5Mn dual-phase steel. From full hard state, the material is heated at 5K/s to 1073K, held for 60s, and then cooled down to 923K at 1K/s. To illustrate the flexibility and the level of complexity that can be achieved, each deformed ferrite grain has been assigned a strain energy from a strain energy distribution. The microstructual evolution is represented by a series of 2D-cuts from the 3D simulation (Figure 2.17). As it is shown in Figure 2.17 (b), ferrite recrystallization is not completed before austenite transformation starts under this condition (red arrows indicated un-recrystallized ferrite grains). This is also shown in Figure 2.16, which gives the phase fractions as a function of time. There is still 0.12 of non-recrystallized ferrite when austenite started to form. Figure 2.17 also reveals that, austenite first form with relatively high carbon concentration from the initial pearlite. This results in a high driving force for consuming of ferrite at the early stage. The equilibrium fraction of austenite is reached in 20s. The complete 3D-structure is shown in Figure 2.18. They concluded that this CA approach provided a good description of both recrystallization and phase transformation.

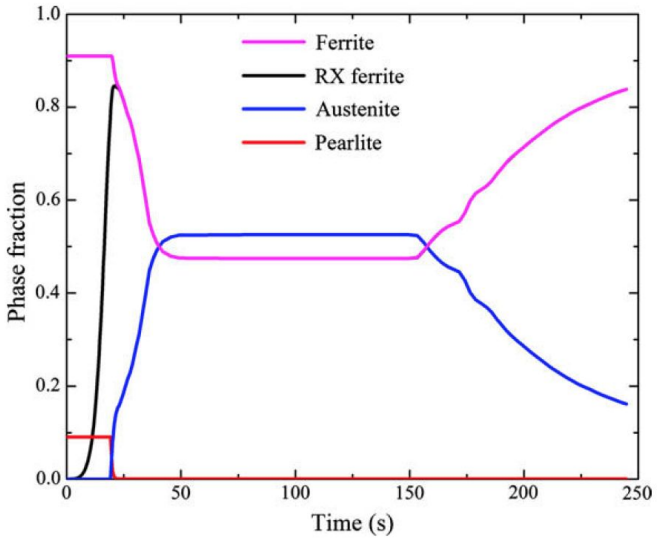


Figure 2.16: The phase fractions as a function of time. The structure from Figure 2.17 (a) was used as the starting structure [4].

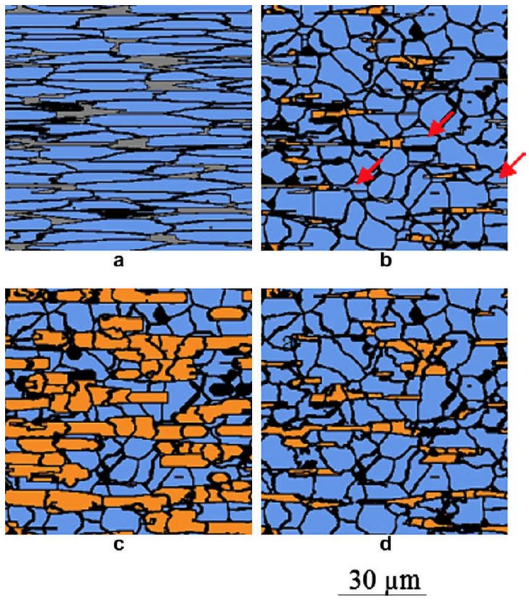


Figure 2.17: Microstructure evolution during the DP annealing simulation: (a) starting microstructure; (b) microstructure at the start of austenite formation in pearlite colonies; (c) just before the cooling stage and (d) at the end of annealing cycle. Austenite is coloured orange, ferrite blue and pearlite grey. The rolling direction is the horizontal direction. The figures show 2D-cuts from the 3D simulation system[4].

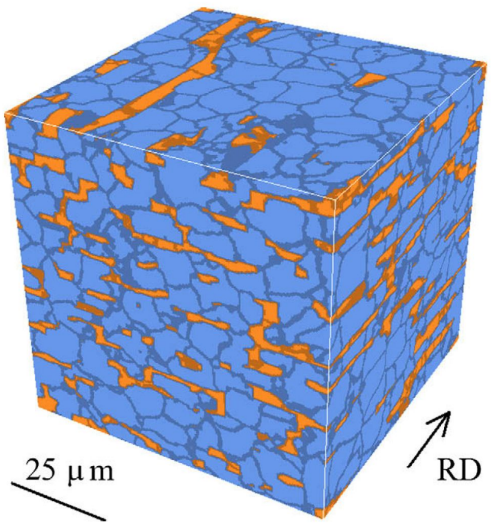


Figure 2.18: The three-dimensional microstructure at the end of the DP annealing cycle simulation: austenite is coloured orange, ferrite blue; RD represents the rolling direction[4].

Bos et al. [5] then studied the influence of different heating rates on the microstructual evolution of a dual-phase steel (0.10C1.6Mn0.3Si0.5Cr), by applying a 3D CA model. Samples were heated to 1053K (780°C) with heating rates of 2, 10, 20, 40 and 80 °C/s, followed by directly gas quenching to room temperature. Figure 2.19 gives the recrystallized ferrite fraction ($f_{rx}$) together with recrystallized ferrite grain size ($d_{rx}$), regarding to different heating rates. It indicated that both the recrystallized fraction and recrystallized ferrite grain size

increases with decreasing heating rate. They explained that this is a consequence of the longer annealing time before quenching associated with lower heating rates. For higher heating rates, only a limited number of nuclei formed, and they are still small when austenite forms. The final microstructure after quenching, obtained both from experiment and from the simulations together with the grain size distribution of the recrystallized ferrite grains are shown in Figure 2.20. It is clear that the average grain size and the distribution of grain size reproduced well. The poor match between simulation and experiments for heating rate 40 and 80 °C/s (Figure 2.20 (a) and (b)) was caused by the noise in the experimental grain size distribution. Figure 2.20 also shows that the fraction of remaining pearlite after quenching decreases with decreasing heating rate. They argued that although the transformation from pearlite to austenite is very fast, there is not enough time to completely dissolve the pearlite under high heating rates. They also discovered that in practice, martensite (austenite before quenching at high temperature) is located almost exclusively along ferrite/ferrite grain boundaries, whereas in the simulations the austenite always appears elongated in the rolling direction and have a strong affinity to pearlite. This revealed a limitation of this CA model approach, that the austenite grain morphology is strongly determined by the initial pearlite morphology. Nevertheless, this CA-model reproduced the microstructure quite well with experiments. It also indicates that the effect of heating rate on the mechanical properties of the final DP steel is more attributed to the distribution of the second phase and not the ferrite grain size distribution.

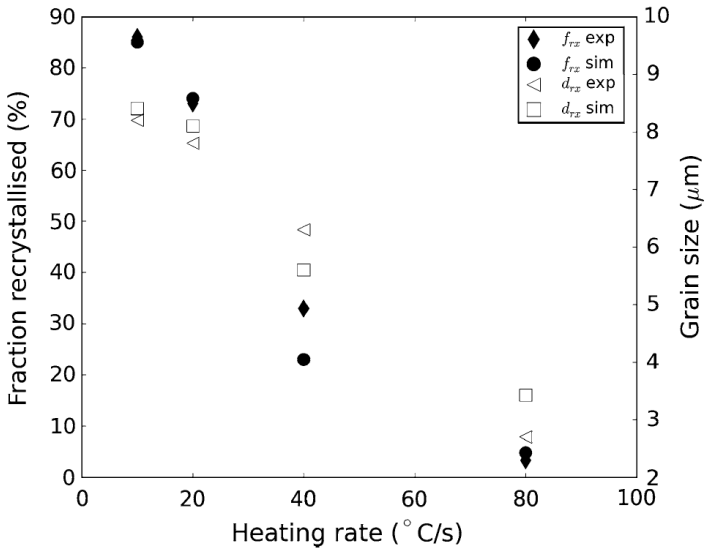


Figure 2.19: Fraction recrystallized ($f_{rx}$) and the area average grain size of the recrystallized grains ($d_{rx}$) as a function of the heating rate to 1053K (780°C). Both the EBSD experimental (exp) and simulation (sim) results are shown[5].

Zheng et al. [40] used a 2D CA model to study the interaction between recrystallization and phase transformation during intercritical annealing of a cold-rolled DP steel (0.08C0.11Si1.75Mn). To obtain full coupling between ferrite recrystallization and austenite transformation, fast heating is imposed, at different temperatures and for different holding times. The simulated microstructures together with carbon distributions, soaked at 760°C for increasing soaking time, are shown in Figure 2.21. Similar to Bos et al.[5], they found that the morphology of the newly formed austenite grains is strongly determined by the shape of the initial pearlite zones, resulting in a banding structure of austenite. Thus further growth of recrystallizing ferrite grains along the compression direction will be topologically restricted. It is shown in the carbon concentration distributions in Figure 2.21 that, the pearlite-nucleated austenite forms with relatively high carbon concentrations, which lead to high driving forces acting the $\alpha/\gamma$ interfaces moving to sweep the surrounding ferrite. From these results, they proposed that the growth of austenite bands can retard ferrite recrystallization in two ways: (I) if the surrounding ferrite matrix remains un-recrystallized, rapid thickening of of the austenite bands will consume most of the potential nucleation sites of recrystallization in the vicinity of the prior $\gamma/P$ interfaces; (II) if the surrounding ferrite has already recrystallized, the intensive austenite growth

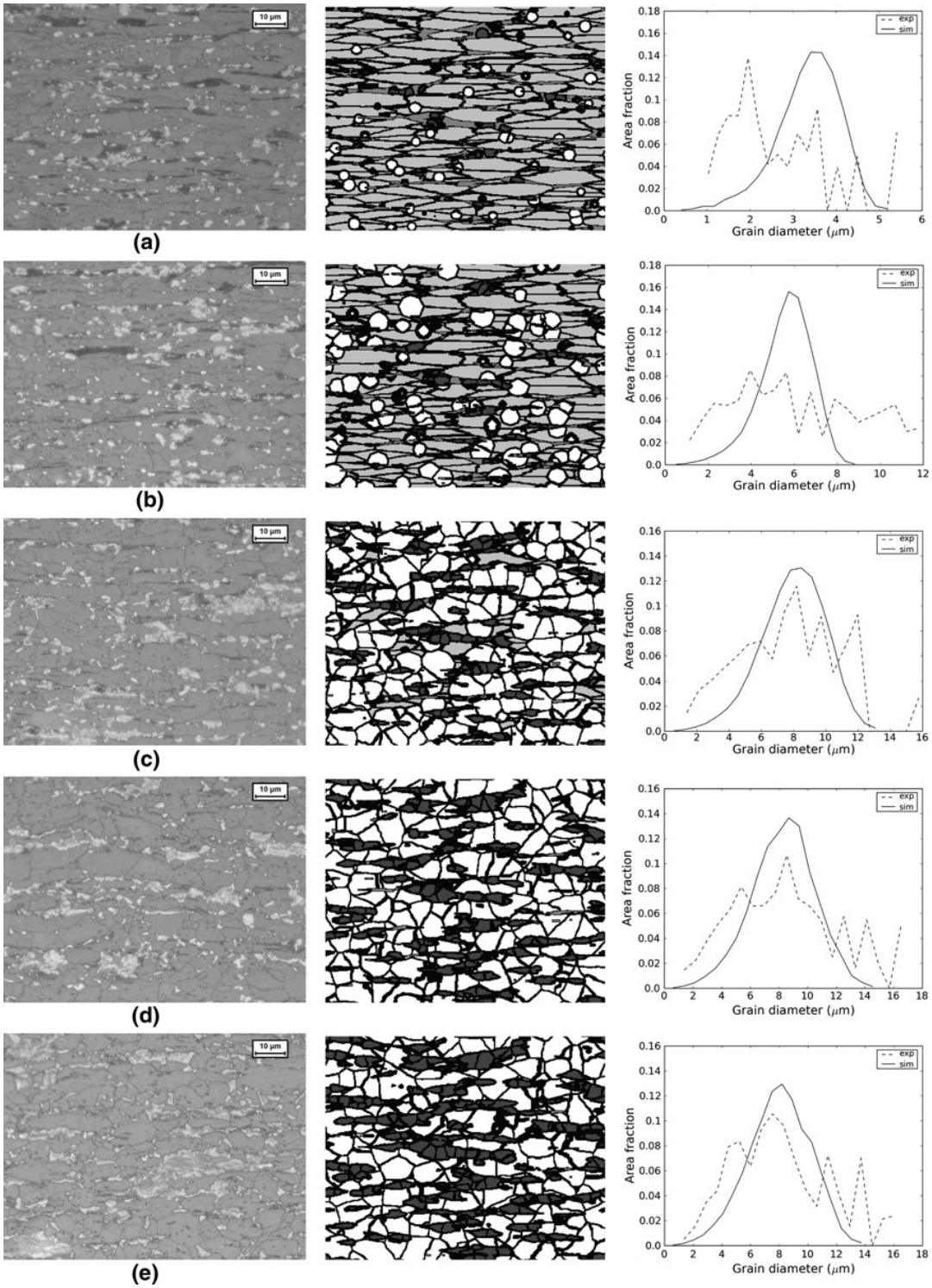


Figure 2.20: Final microstructure from the EBSD experiment (left) and from the simulations (middle) and the grain size distribution of the recrystallized ferrite grains (right) for a heating rate of: (a) 80 °C/s, (b) 40 °C/s, (c) 20 °C/s, (d) 10 °C/s, and (e) 2 °C/s. The simulated micrographs are 2D cuts from the 3D simulation system and have the same scale as the optical micrographs. In the simulated micrographs, pearlite is middle gray, austenite is dark gray, deformed ferrite is light gray, and recrystallized ferrite is white[5].

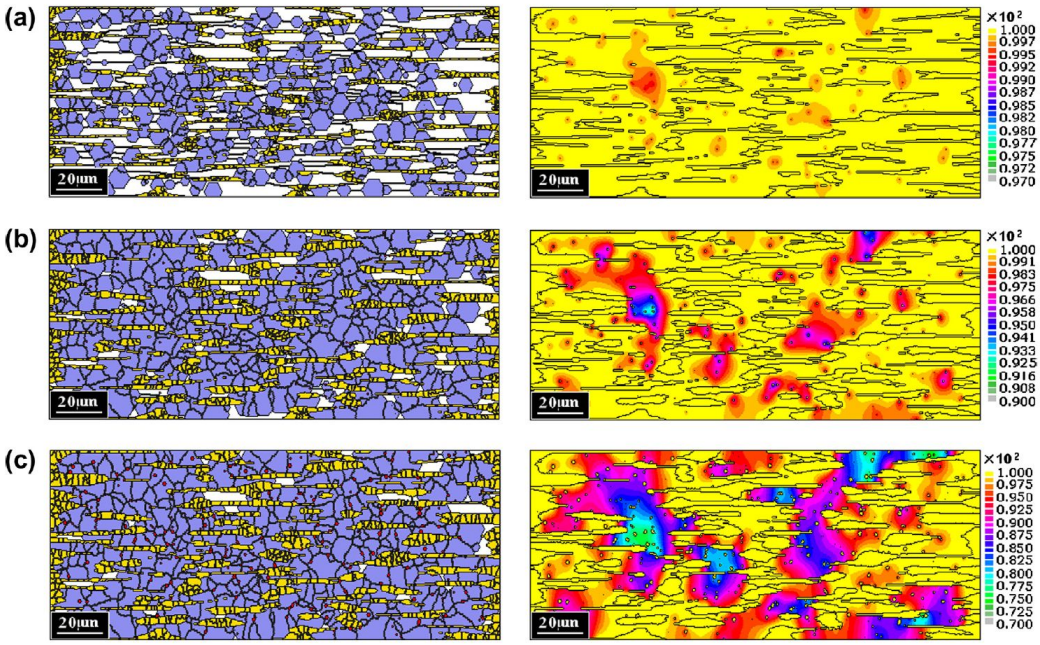


Figure 2.21: Simulated microstructure (left) and the carbon concentration field (wt.%) in ferrite phase (right) at different soaking times: (a) 5 s, (b) 20 s, (c) 40 s, during the isothermal holding of 760 °C. In the simulated microstructure (image left-hand side), the yellow areas are the pearlite-nucleated austenite; the small-sized red patches (image left-hand side) are the grain-boundary-nucleated austenite. The blue regions indicate the recrystallized ferrite and the white indicate un-recrystallized ferrite (image left-hand side). The black lines in the figures indicate the grain boundaries. The images on the right-hand side indicate the distribution of carbon[40].

will consume the recrystallized regions and transform them into austenite. They also studied the influence of heating rates and soaking temperatures on this interaction effect. They found that both ferrite recrystallization and phase transformation are promoted significantly with an increase in annealing temperature. By increasing the initial heating rate, a morphology occurs from randomly distributed to a banded structure of austenite, and this trend is consistent with experimental findings.

### 2.2.3. Phase-field model

One of the most powerful tools for calculation of microstructure evolution of dual-phase steel is phase-field. Phase field model treats a multi-phase system, containing both bulk and interface regions, in an integral manner. One or more field variables, $\phi_i(r,t)$, which is also referred to as phase field or order parameters, are introduced to describe at any time, $t$, and at each point, $r$, the different domains present in the system. These phase field variables have a constant value in the bulk regions, and change continuously over a diffuse-interface of thickness $\eta$. Thus, phase-field is not a sharp-interface model, compared with CA model. Similar to CA model, both carbon diffusion and interface migration are taken into account for solid-state phase transformation, thus, it is also a mixed-mode model. This model can incorporate strain effects for solid-state transformations and can account for solute drag and trapping by means of the interface mobility acting as a model parameter.

#### Theory

The multiphase field model derived by Steinbach et al. [33][34][35] is used to study the austenite to ferrite transformation. A polycrystalline system of $N$ grains is described by a set of $N$ order parameters $\phi_i(r,t)$, also represented by the vector $\vec{\phi} = \phi_1, \phi_2 ... \phi_N \cdot \phi_i(r,t)$ is defined as follows:

- $\phi_i(r,t) = 1$, if the grain $i$ is present at the location $r$ and time $t$;

- $\phi_i(r,t) = 0$ if the grain $i$ is not present at $r$ and $l$.

$\phi_i(r,t) = 0$ changes continuously from 0 to 1 within a transition region or interface of width $\eta_{ij}$ (Figure 2.22). The interfacial thickness is taken to be the same for each pair of grains in contact, i.e. $\eta_{ij} = \eta$.

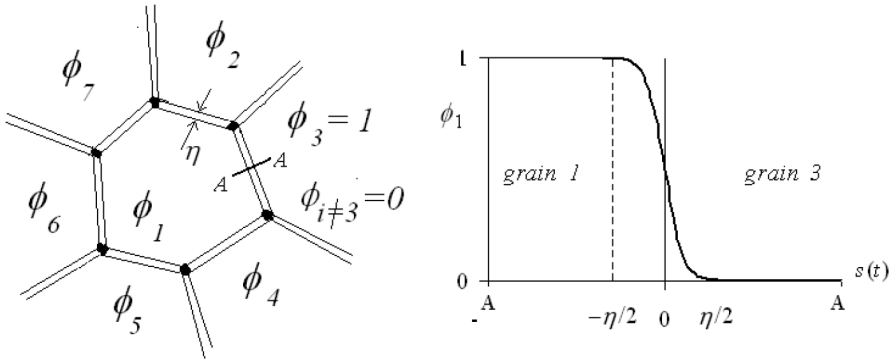


Figure 2.22: Definition of the phase field parameter $\phi_i(r,t)$: (a) representation of the microstructure, (b) $\phi_1(r)$ along the section AA.[22]

The interface thickness $\eta$ can be chosen to be large compared to the atomic interface thickness, but small compared to the microstructure length scale. There is one limitation of this approach: the interface thickness $\eta$ has to be much smaller than the smallest length of all the solutal diffusion fields. If this condition is not fulfilled, phase-field model will suffer from numerical artifacts and will not describe the correct transformation kinetics.

The time evolution of the phases is calculated by a set of phase-field equations deduced by minimization of the free energy functions:

$$\dot{\phi}_i = \sum_j M_{ij}(n)\left(\sigma^*_{ij}(n)K_{ij} + \frac{\phi}{\eta}\sqrt{\phi_i\phi_j}\Delta G_{ij}(c,T)\right) \tag{2.14}$$

$$K_{ij} = \phi_j\nabla^2\phi_i - \phi_i\nabla^2\phi_j + \frac{\phi^2}{\eta^2}(\phi_i - \phi_j) \tag{2.15}$$

In Equation 2.14, $M_{ij}$ is the mobility of the interface as a function of the interface orientation, described by the normal vector $n$. $\sigma^*_{ij}$ is the effective anisotropic surface energy (surface stiffness), and $K_{ij}$ is related to the local curvature of the interface. The interface is driven by the curvature contribution $\sigma^*_{ij}K_{ij}$, as well as the thermodynamic driving force $\Delta G_{ij}$. The thermodynamic drving force, which is function of the local composition $c$, couples the phase field equations to the diffusion equations:

$$\dot{c} = \nabla\sum_{i=1}^{N}\varphi_i D_i \nabla c_i \tag{2.16}$$

where $D_i$ is the multi-component diffusion coefficient matrix for phase $i$.

### Previous applications of phase-field model

Phase-field model has been applied to study the transformation from austenite to ferrite, as well as the other way around. For the interest of this thesis, special attentions are drawn to the application of this powerful tool on the heating precess, hence, transformation from ferrite to austenite.

Rudnizki et al.[27] studied the microstructual evolution of a DP steel (0.098C0.24Si1.65Mn) upon heating at 1°C/s from 720 °C. By comparing the simulation result using phase-field model, with experimental results, the quality of the phase transformation simulation was verified. The simulation of austenite transformation were carried out under two kinds of conditions: LENP and PE. The corresponding results were compared.

The evolve of austenite fraction regarding to the temperature of both simulation results and metallographic results are plotted in Figure 2.23.They found out the the simulation results fit the experiments very well, and concluded that under this condition, the formation of austenite from ferrite for LENP conditions matches experimental data much better than the simulation uncer PE condition (Figure 2.23). The simulated austenite fraction results under LENP reflected the two-step kinetics of austenite formation and closely matches the experimental results. As expected the simulated austenite fraction of LENP lied below the PE model, because the implemented redistribution behavior resulted in a much lower driving force and a much higher retarding effect on the transformation compared to PE. The micrographs at selected temperatures from simulation under LENP and experiments were also compared Figure 2.24. It showed that both austenite fraction and distribution of austenite grain size from simulated results fit well at different temperatures with experiments.

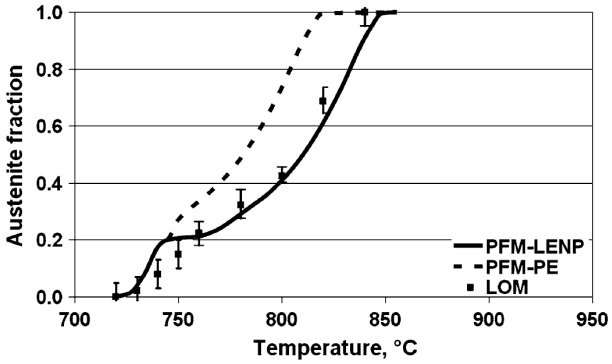


Figure 2.23: Simulation results for the evolution of the austenite fraction during heating with 1 °C/s compared to metallographic results. *LOM* indicates metallographic results from stop-quenched samples; $PFM-LENP$ and $PFM-PE$ indicate simulation results under corresponding conditions[27].

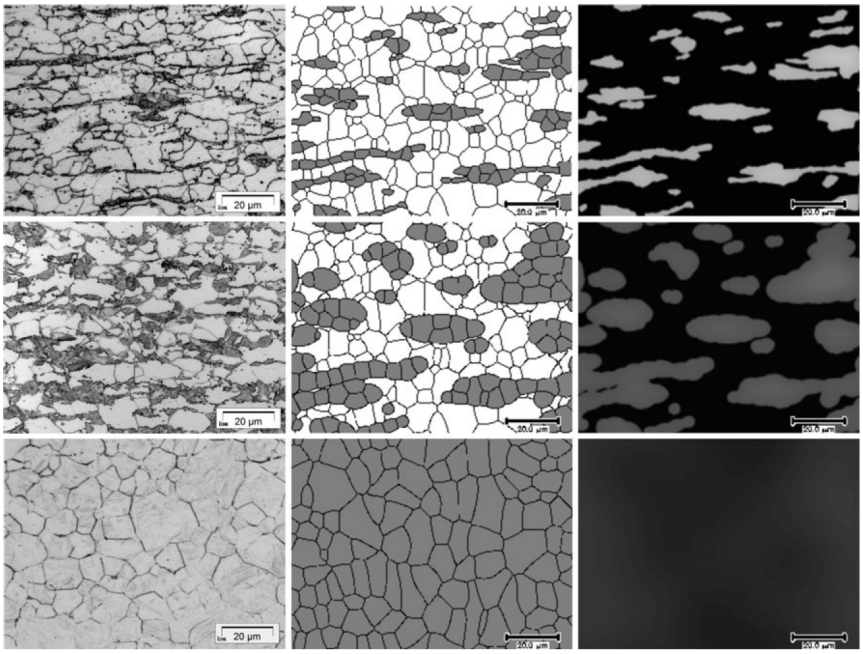

Figure 2.24: Nital-etched micrographs of the samples (left), simulated phase where ferrite is white and austenite gray (center), and simulated carbon distribution (right); the top row corresponds to 740°C, the center row to 800°C, and the bottom row to 850°C[27].

Rudnizki et al. [28] later studied and compared the quality of 2D and 3D simulations by phase-field model, with the same material (0.098C0.24Si1.65Mn) and similar condition. The ferrite fraction predicted by 3D-simulation is compared together with 2D-simulation and experimental results in Figure 2.25. It shows that 3D-simulation results had a good agreement with the experimental data, as well as a good reproduction with 2D-results. The ferrite amount simulated in 3D and 2D is inside the scatter bars obtained by metallographic analysis. The comparison of 2D- and 3D-simulated and experimental grain size distribution of ferrite after intercritical annealing is presented in Figure 2.26, with results taken at 650°C. Both simulated grain size distributions matches the EBSD results quite well. They concluded that the accurate definition of input model parameters yields both 2D- an 3D- approaches to simulate the microstructure evolution successfully. They stressed that, 2D-simulation has the advantage of the achievement of fast results and a directly comparison with experimental data, compared to 3D-simulations. This enables rapid revelation of the influencing parameters, and therefore can be utilised for the optimisation of process parameters to achieve essential microstructure. 3D-simulations are time consuming, but it can be applied easily for the coupling with models for the prediction of mechanical properties.

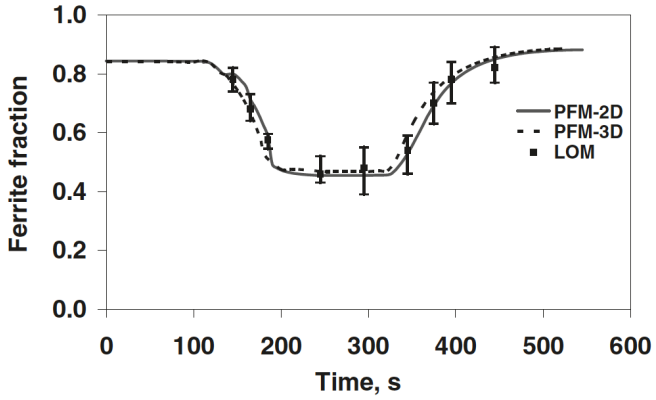


Figure 2.25: 3D-simulation results for the evolution of the ferrite fraction evolution compared with 2D-simulation results and experimental data. *LOM* indicates metallographic results from stop-quenched samples; $PFM-2D$ and $PFM-3D$ indicate results corresponding to 2D and 3D simulations[28].

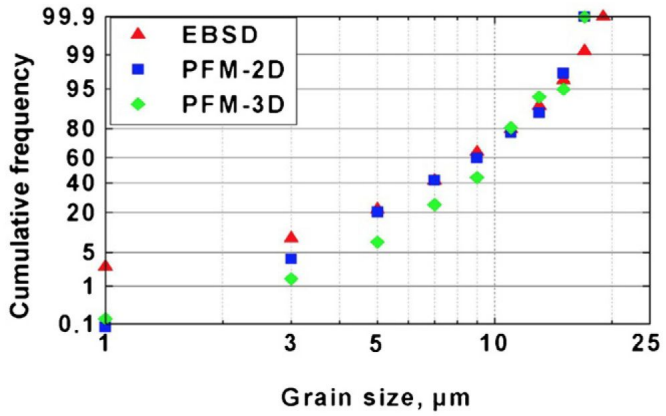


Figure 2.26: 2D- and 3D- simulation results for the ferrite grain size distribution at 650°Ccompared with the experimental data from EBSD analysis [28].

Mecozzi [22] studied the austenite to ferrite transformation of a steel with 0.1C0.49Mn. The sample was heated at 0.8°C/s to 1000°C and soaked for 120s, then cooled to room temperature at cooling rate of 0.05, 0.4 or 10°C/s. She found out that the simulated microstructures at different cooling rates reproduce quite well the variety in microstructures observed experimentally. The model well simulated the ferrite grain size and

morphology, and also the distribution of pearlite colonies, which are the remaining austenite regions in the model above eutechtoid temperature. The simulated carbon concentration profiles across the $\alpha/\gamma$ interface of three cooling rates are shown in Figure 2.27. In all three cooling rates the maximum carbon concentration at the interface increases with transformation. This is the result of the higher local equilibrium value at the interface caused by carbon enrichment and decreasing temperature. The fit of the solid line with the interface-controlled models (closed circle in Figure 2.27) at early stage of transformation indicates that, the initial stage of transformation is always nearly interface-controlled. She explained that this is because, right after nucleation, the small amount of carbon atoms rejected from the ferrite phase can easily diffuse into the bulk of austenite, and the lattice transformation is the rate-controlling process. As ferrite grains grow, the amount of carbon rejected from ferrite increases and carbon diffusivity becomes also important, which appears in Figure 2.27 as the approaching of solid line to the open circles (diffusion-controlled). Although different cooling rates evolves to diffusion-controlled transformation in different manners, depending on the morphologies formed on cooling. In this way, the phase-field model has successfully revealed the mixed-mode nature of the transformation, and provides insight in the kinetics behind phase transformation.

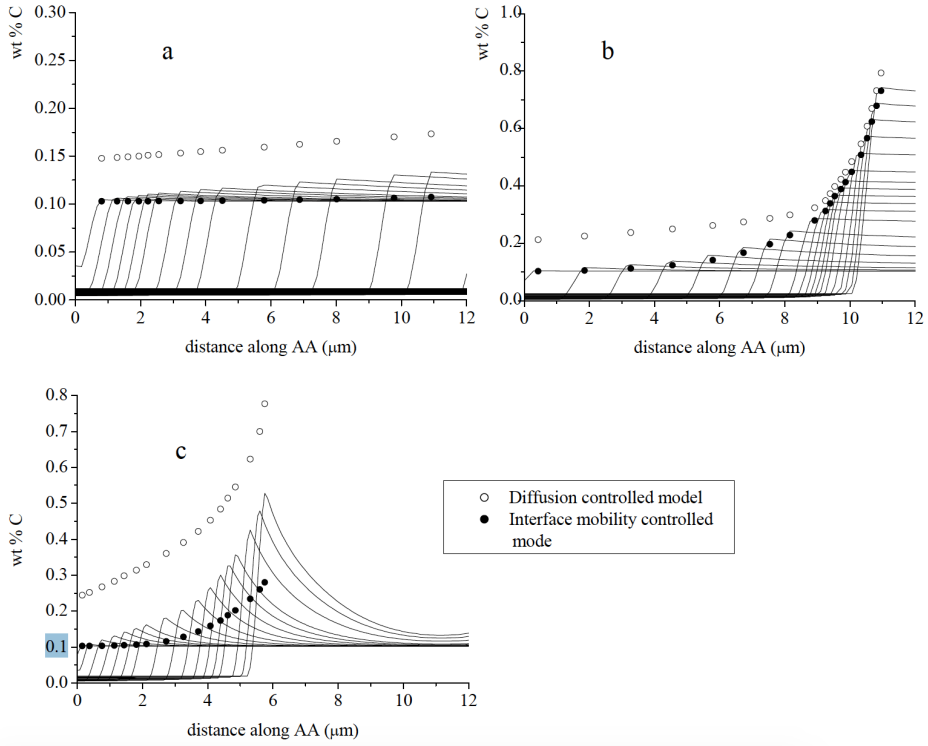


Figure 2.27: Carbon distribution along the $\alpha/\gamma$ interface at different temperatures on cooling at (a) 0.05K/s, (b) 0.4 K/s, (c) 10 K/s of the simulation results (solid lines), comparison with the carbon content in austenite at the interface as predicted by the diffusion controlled and interface mobility-controlle model (markers) [22].

# 3

# Experimental Methods

## 3.1. Composition

Commercial DP steels are cast, hot rolled, cold rolled, and continuous annealed before coated with zinc. All samples have the same cold rolling reduction. The microstructures of current intermediary DP steel product show 10-20 $\mu m$ large acicular ferrite grains with 20 $\mu m$ sized dark pearlite islands after hot rolling. The product is then cold-rolled down to 1.3-1.5 mm thick, followed by continuous annealing process. The material used in this thesis is cold-rolled strips before continuous annealing process. The composition of the studies materials are listed in Table 3.1.

Table 3.1: Compositions of DP steel

| Elements | C | Mn | Al + Si | V, Nb, Ti | N* | Other elements |
|---|---|---|---|---|---|---|
| wt% | 0.12-0.16 | 2.02 | 0.8-1.2 | 0.06 | <50 | <0.1 |

* ppm

## 3.2. Dilatometer

### 3.2.1. Dilatometry method

Dilatometry is a common technique to study phase transformation. When a sample is heated and the temperature rises linearly with time, the length will increase linearly with temperature, following the equation:

$$\frac{\Delta L}{L} = \alpha_L \Delta T$$

$$Dilatation = \frac{\Delta L}{L}$$

Where L is the total length of the sample, $\Delta T$ is the change of length, and $\alpha_L$ is the thermal expansion coefficient of the material. When the material undergoes phase transformation, the change in crystal structure and density will cause a change in volume. This will lead to a change in length, which is captured by the dilatometer. The thermal expansion coefficient of the new phase is different from the old, so the dilatometer curve is no longer linear. Thus, the deviation of dilatometer curve from linear lines indicates the ongoing of phase transformation.

Dilatometry is done on two dilatometers: Bähr thermo Analyse Dil 805, at TATA steel, with strip samples 5 mm wide, 10 mm long, and 1-2 mm thick; and Bähr thermo Analyse Dil 905, at TU Delft, with strip samples 4 mm wide, 10 mm long and and 1-2 mm thick. In both cases a thermo couple is spot-welded to the sample to control the temperature. Heating is realized by a high-frequency induction coil. A vacuum of the order $10^{-5}$ mPa is applied during heating, to protect the sample from oxidization. Quenching is done in air at TATA, while helium is used in the dilatometer of TUDeft. Full quench is applied in both dilatometers, which means the maximum cooling rate capacity to room temperature of the dilatometers are used.

### 3.2.2. Sample preparation

In order to study the influence of welding position of thermal couple on accuracy of the dilatometer, four different welding positions are applied during the sample preparation, demonstrated in Figure 3.1 together with the standard welding position. A standard welding position for the thermal couple should be in the middle of the plate, both in the vertical and horizontal direction, with the distance between the two wires of around 1mm.

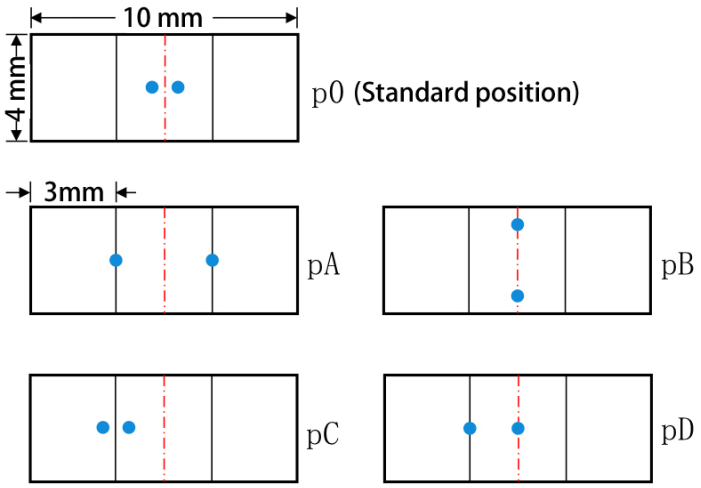


Figure 3.1: Demonstration of welding positions of thermal couple on dilatometer samples.

### 3.2.3. Thermal cycles

Different sets of dilatometer cycles are applied to investigate the evolution of microstructure in the material. The intercritical temperature is chosen as 800°C. In order to observe recrystallization behavior, samples are heated up to 800°C with three heating rates: 4.4°C/s, 18.6°C/s, and 80°C/s. Each heating rate is stopped and quenched at temperatures 650°C, 680°C, 720°C, and 740°C, demonstrated in Figure 3.2.

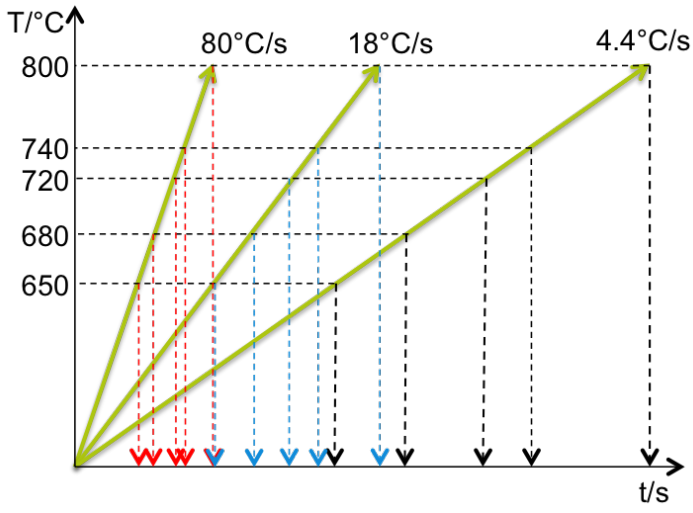


Figure 3.2: Demonstration of dilatometer experiments before 800°C.

The martensite transformation temperature is found to be very sensitive to different heating rates. Thus, various heating rates are applied to heat the sample up to 800°C and quench. To further study the behavior of austenite transformation, samples are heated up to 800°C and soaked up to 10 minutes, demonstrated in Figure 3.3. All thermal cycles used are listed in Appendix B, samples are further investigated by SEM. Each

dilatometer sample is given a code, as listed in Table 3.2. The full list of all the samples can be found in Appendix A.

To obtain the austenite transformation temperature ($Ac_1$, $Ac_3$ and Ms), fully austenitic annealing is applied with different heating rates, with top temperature 1000°C and holding time 3 minutes (see Appendix B).

Table 3.2: Sample code for dilatometer cycles

| Sample code | Top temperature (°C) | Heating rate (°C/s) | Holding time (s) |
|---|---|---|---|
| HR4 | | 4.4 | |
| HR10 | | 10 | 0, 5, 10, 30 |
| HR18 | 800 | 18.6 | 60, 180, 600 |
| HR40 | | 40 | |
| HR80 | | 80 | |

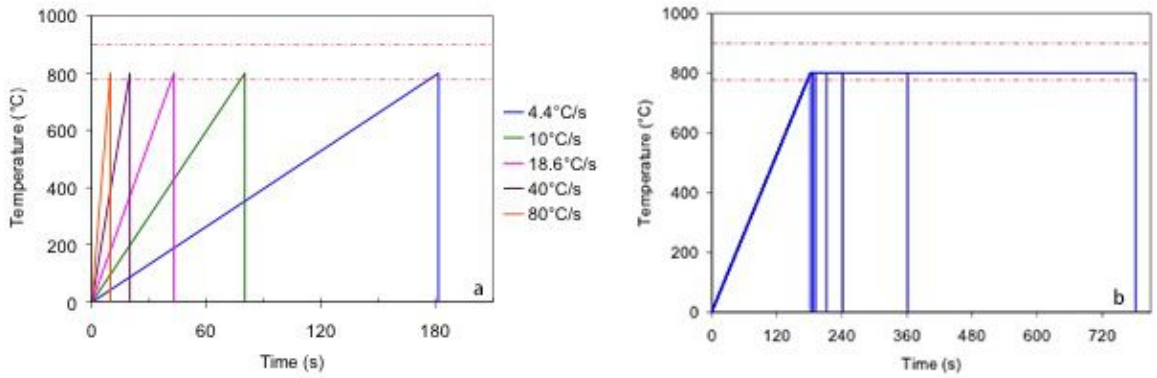


Figure 3.3: Demonstration of dilatometer experiments: (a) different heating rates; (b) increasing holding time.

### 3.2.4. Determination of phase transformation temperature

In order to determine the phase transformation temperatures in different dilatometer tests, different determination methods are applied, including: i. lever rule, ii. deflection point in the dilatometer curve (directly quenched samples), iii. derivative of dilatometer curve (directly quenched samples).

#### Lever rule

When the material undergoes phase transformation, the change in crystal structure and density will cause a change in volume. The lever rule method can be applied to calculate phase transformation volume fraction. Take the transformation from pearlite+ferrite to austenite as an example, the thermal expansion can be determined by extrapolation of the linear region before and after transformation, demonstrated in Figure 3.4. The austenite fraction ($f_L^\gamma$) at a certain temperature can be calculated as:

$$f_L^\gamma = \frac{L_3 - L_1}{L_2 - L_1}$$

Where $L_1$ is the length corresponding with the pearlite + ferrite microstructure, $L_2$ is the length corresponding with fully austenite phase, and $L_3$ is the actual length at the given temperature. Since the dilatometer can only capture the change of length, not the change of volume, in this method the volume differences between different phases are not taken into account. It is assumed that the volume change of ferrite and pearlite are the same. Another factor that is neglected is the influence of carbon content on austenite lattice parameter. As phase transformation proceeds, the lattice parameter of austenite is changing together with the carbon content, and in fact the cell volume of austenite is not constant over time.

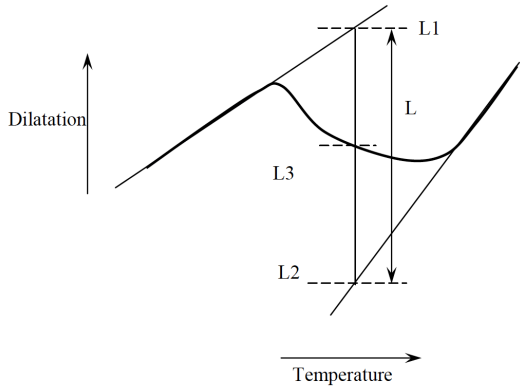


Figure 3.4: The scheme for the determination of the fraction transformed from a dilatometer curve using the lever rule method [29].

In this thesis, lever rule is applied to determine the austenite transformation fraction as well as martensite transformation fraction for fully austenite annealed samples. This method is also applied to determine martensite transformation fraction of intercritical annealed samples with holding time varying from 5 s up to 10 mins, from which martensite transformation temperature can be revealed. While in the case of full austenite transformation, a different method is applied to determine the martensite transformation temperature.

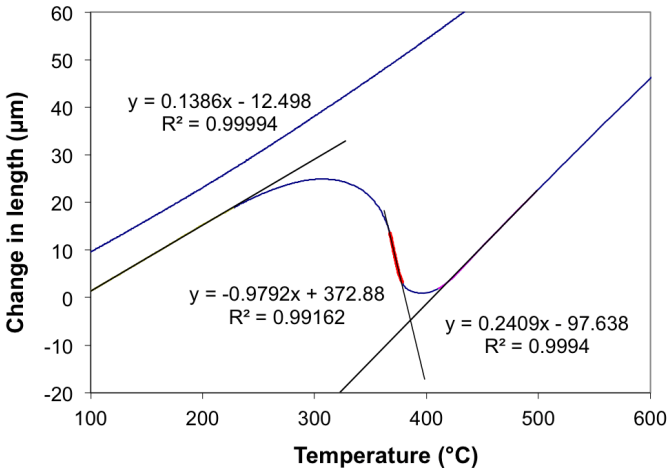


Figure 3.5: Determination of Ms from fully austenite annealed samples, HR4.

Figure 3.5 is an example of a cooling part in a dilatometer curve from a fully austenite annealed sample. Same as lever rule, a linear fit for the pre-transformation curve is applied. When austenite transform into martensite, due to the in-homogeneous distribution of carbon, the martensite transformation temperature varies in a range. Nevertheless, there is a linear part in the transformation curve which represents the behavior of most of the austenite in the material. By taking a linear fit to this part, Ms is then determined by the cross-section of this line and the line before martensite transformation.

### Deflection point in the dilatometer curve (directly quenched samples)

When Austenite transform into martensite a change in thermal expansion coefficient will happen, cause a sudden change of the slope in the cooling part of dilatometer curve. In directly quenched samples, since the sample has stayed above $Ac_1$ only for a short time, the amount of austenite is considerably small, and lever rule cannot be applied to the cooling curve to determine the transformation temperature and fraction.

As there is a sudden change in the slope of the cooling dilatometer curve, the transformation temperature can be taken from the dilatation vs. time curve (Figure 3.6), using the deflection point.

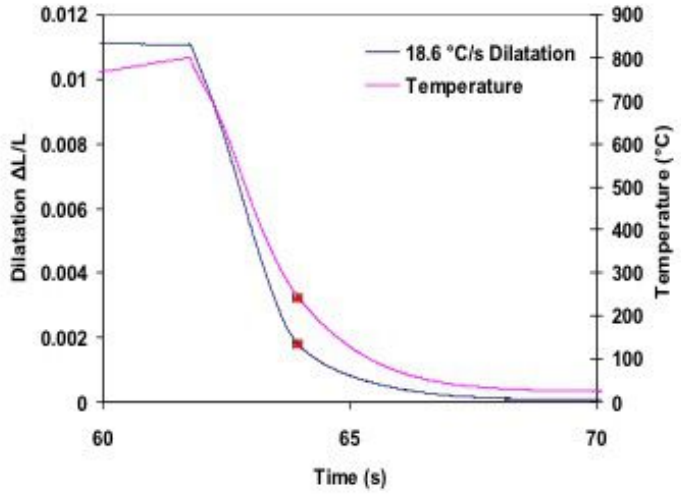


Figure 3.6: Determination of transformation temperature Ms for directly quenched samples from cooling curve.

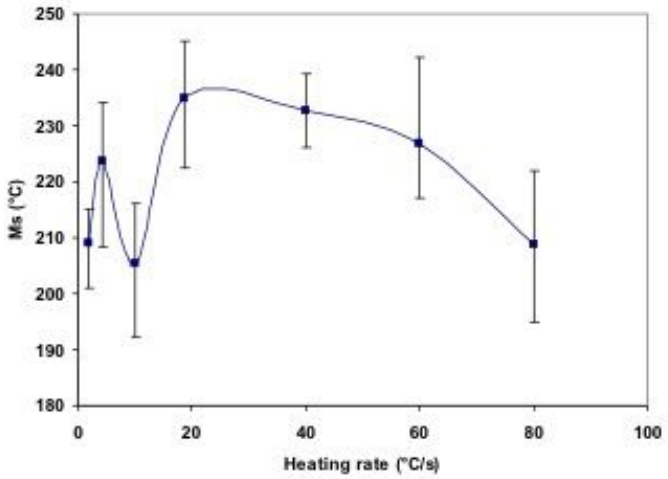


Figure 3.7: Ms as a function of heating rate, determined by the deflection point in the dilatometer cooling curve, directly quenched samples.

The obtained results are plotted in Figure 3.7. Significant error bars can be caused by the fast cooling rate. The estimated start of martensite transformation is within 0.25s (horizontal error bar in Figure 3.6). With a cooling rate of -200°C/s, this could cause an error of 20-30 °C. In addition, the deduction of martensite transformation temperature from the cooling curve is to very big extent subjective, leading to different values from the same curve. However, if one operator ideally determines Ms from all data, this variation of observation error is in a similar way and in the same range.

### Derivative of dilatometer curve (directly quenched samples)

A more accurate method is to determine Ms from the derivative curve of the dilatometer cooling curve. By applying a parabola fit to the local data of the curve, a derivative can be calculated for each point, hence each

temperature, in the cooling curve. In the same way, a second derivative can also be obtained. Accuracy can be improved by applying Savitsky-Golay smoothing. The principle of this smoothing is, while fitting the data into parabolas, different numbers of data (4, 6, 8) can be taken into account from either side of the data point. The fit and the calculation of first and second derivatives are as follows:

$$Fit: \sigma = b + m_1\epsilon^2$$
$$First\ derivative: \frac{d\sigma}{d\epsilon} = m_1 + 2m_2\epsilon$$
$$Second\ derivative: \frac{d^2\sigma}{d\epsilon^2} = 2m_2$$

The first and second derivatives of the dilatometer curves are plotted in Figure 3.8. The curve shows a sudden change in the first derivative, from a relatively constent slope to gradually reduced slope, which indicates the martensite transformation. Although the determination of this deflection point is still not accurate enough, the second derivative is not really valid any more, due to the large background noise of the data (pink curve in Figure 3.8). The first derivative of different numbers of reference points are compared in Figure 3.9. It is clear that the more reference points taken, the smoother the curve will become. And this smoothing effect does not affect the accuracy of the determination, instead, it will make the determination of the deflection point easier and reduce the error. Thus, smoothing with eight reference points are taken from both sides in all the following treatments.

After a gradual reduction of the slope, the first derivative comes to a plateau again below a certain temperature, which indicates the end of the transformation. Both temperatures are taken from the curve. For the reason of convenience, the start temperature of the transformation is called $Ms_{0\%}$, and the finish temperature is called $Ms_{99\%}$. Error in $Ms_{0\%}$ is about ±5°C, and error for deciding $Ms_{99\%}$ is about ±8°C. In the following discussion in this thesis, $Ms_{10\%}$ will be used to compare characteristics of different samples. $Ms_{10\%}$ can be calculated as:

$$Ms_{10\%} = Ms_{0\%} - (Ms_{0\%} - Ms_{99\%}) \times 10\%$$

.

And the error of $Ms_{10\%}$ will be:

$$\pm 5 + \pm 8 \times 10\% = \pm 6\ ^\circ C$$

.

This $Ms_{10\%}$ calculation does not take into account the error introduced by the non-linearity of transformation. This error is for now hard to evaluate due to the complicated nature of martensite transformation. Nevertheless, compared to the previous method, this derivative method has greatly reduced the error of the determination of martensite transformation temperature, so that this method is applied in all the directly quenched samples in the following discussion in this thesis. In the following discussion, it will be discussed how big is the influence of this uncertain error to the conclusion of this thesis.

## 3.3. Scanning electron microscopy(SEM)

Microstructure of the samples was studied by scanning electron microscopy (SEM), using JEOL JSM-6500F Field Emission Scanning Electron Microscope at TU Delft. The secondary electron images are produced by a LEO 438VP scanning electron microscope fitted with a Tungsten filament. Samples are embedded in a conductive resin, polished at TATA steel, and slightly etched to reveal the grain boundaries.

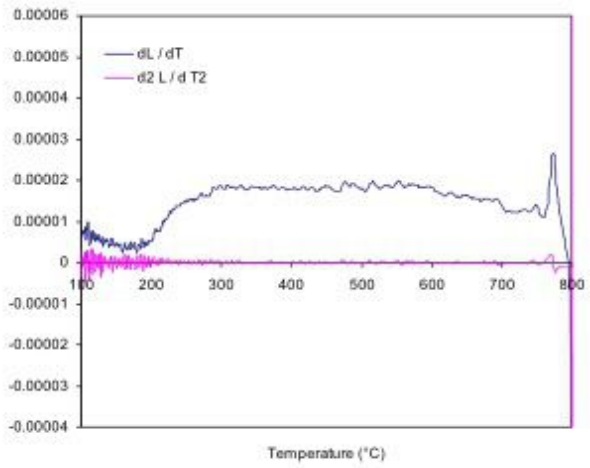


Figure 3.8: First derivative vs second derivative, 8 reference points (HR2).

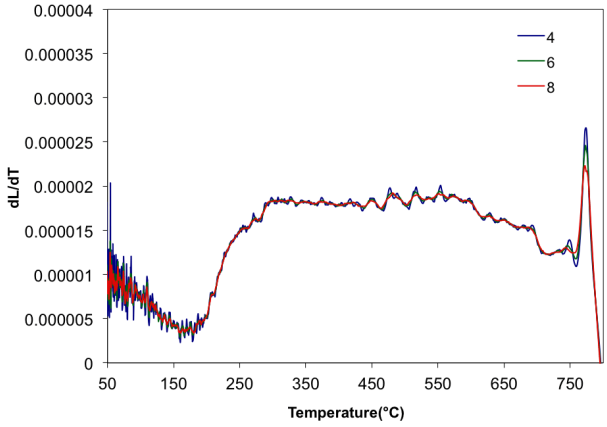


Figure 3.9: Comparison of different number of reference points taken in the Savitsky-Golay smoothing (HR2).

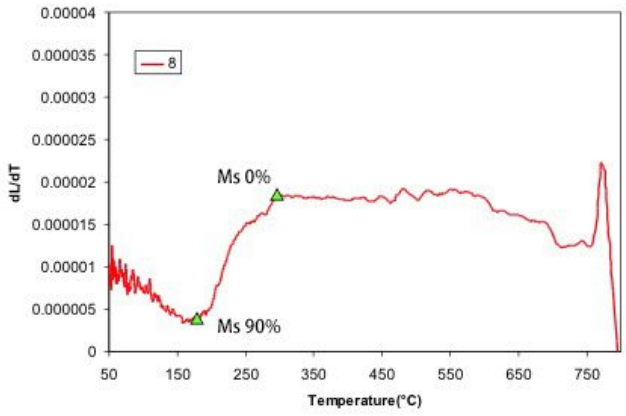


Figure 3.10: Determination of Ms by first derivative of the cooling curve.

# 4

# Simulation settings

Due to the limitations of the two kinds of models, both CA model and phase-field model are used to deduce different scenarios.

## 4.1. CA-modelling

The limitation of current CA-model is that austenite can only nucleate from prior pearlite colonies, and cannot reveal phenomenon as nucleation of austenite on ferrite-ferrite grain boundaries. Thus, in this thesis CA-model is only applied to study the influence of heating rates on ferrite recrystallization before austenite transformation starts.

In this thesis, a 2D CA-model is applied on a dual-phase steel (0.15C2Mn0.06Si). The input thermodynamic driving force is calculated from calculation software Thermo-Calc®. Simulations were calculated under PE conditions, with a grid size $\delta$ of 0.25 $\mu$m.

The creating of start microstructure first requires a full austenitic structure, which evolves five steps[4]:

(i) Creation of a fully austenitic system based on a Voronoi structure;

(ii) Cooling down the system to 900K ending in a microstructure with ferrite and austenite;

(iii) Artificially transforming austenite into pearlite;

(iv) Deforming the microstructure by scaling the normal and rolling direction, with a reduction of 30% in the normal direction;

(v) Assigning a strain energy to the deformed ferrite grains, according to Figure 4.1[4].

The creation of initial full-hard microstructure is similar to Bos et al.[4]. Starting from a system with 300×300 cells, the final micrograph after deformation consist of 90×1000 cells. The input parameters are listed in Table 4.1, which is also similar to Bos et al.[4].

Table 4.1: Simulation input parameters of CA model

| | Nucleation | Growth (thermodynamic, kinetic, and diffusion parameters) |
|---|---|---|
| RX of $\alpha$ | $T_{RX}^{nucl} = 953\ K$<br>$n_{RX} = 1.4 \times 10^{15}\ m^{-3}$ | $M_0^{\alpha\alpha} = 1.95\ mol\ mJ^{-1}s^{-1}$; $Q_{\alpha\alpha} = 142\ kJ\ mol^{-1}$ |

## 4.2. Phase-field model

Due to the computational cost of phase-field model, it is only applied for austenite formation above $Ac_1$. Simulations were carried out using the commercial software package MICRESS®. The initial microstructure

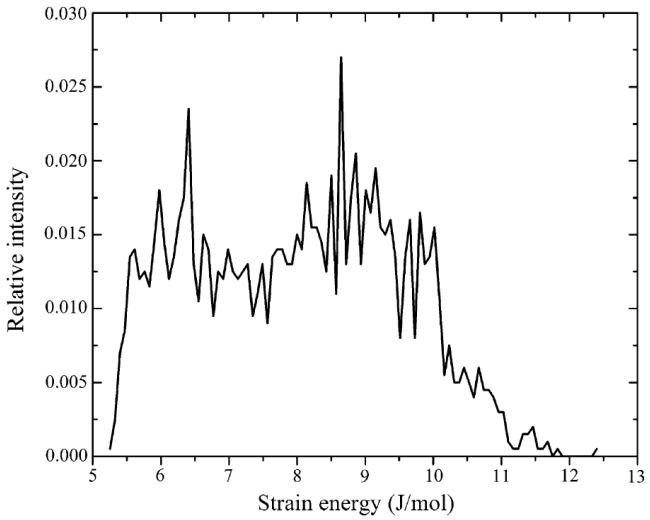


Figure 4.1: The strain-energy distribution as obtained from the Alamel model [13] calculations for a reduction by 67% and an average strain energy of .

is obtained from the previous CA-model results, slightly adapted to the MICRESS®software. The simulated area consist of 250×250 grids, with the grid size of $0.1\mu m$. The initial microstructure consists of ferrite plus cementite.

Austenite nucleation is set to occur at the $\alpha/\alpha$ grain boundary and $\alpha/\theta$ interface; shield distance (4.0 $\mu$m) and shield time (10 s), which define an area around a nucleus where for the specified shield time no further nucleation occurs, were adjusted to describe the cementite nucleation as site saturation.

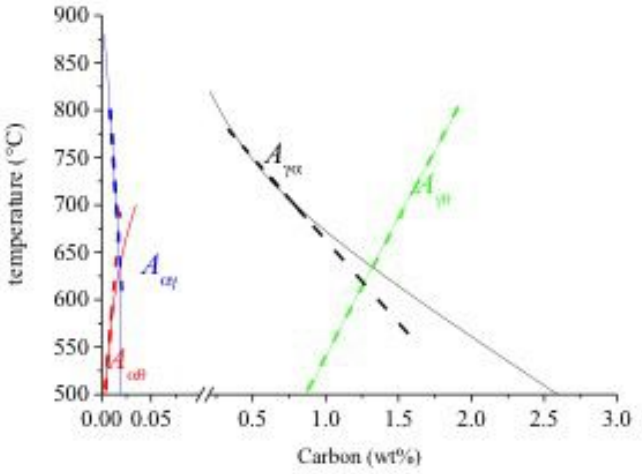


Figure 4.2: Demonstration of linearlization of the phase diagram for driving force calculation. Quasi-binary Fe-C phase diagram calculated for the formation of ferrite under PE conditions (solid lines) and linearised $\alpha/\alpha+\gamma$ and $\gamma/\alpha+\gamma$ boundary lines (dashed lines) (a); addition of the $\alpha/\alpha+\theta$ and $\gamma/\gamma+\theta$ boundary lines, calculated under PE condition (b).

The thermodynamic data for the calculation of the driving force for the transformation were taken from the linearised phase diagram (Figure 4.2), derived by using Thermo-Calc software in para-equilibrium condition.

For each austenite nucleation site (at the $\alpha/\theta$ and $\alpha/\alpha$ interface) the minimum undercooling for austenite precipitation is specified (10.0 K). For a given undercooling the driving force for austenite growth is set equal to the value calculated by Thermo-calc®for the specific composition by adjusting the value of the proportionality factors $\Delta S_{\alpha\gamma}$ and $\Delta S_{\gamma\alpha}$.

The parameters of the linearised Fe–C pseudo-binary diagram for ferrite formation and cementite formation both in ferrite and austenite are reported in Table 4.2.

Table 4.2: Data of the linearised Fe–C pseudo-binary diagram under para-equilibrium conditions

| $T^R$ (°C) | $x^{CR}_{\alpha\gamma}$ (wt%) | $x^{CR}_{\gamma\alpha}$ (wt%) | $m^R_{\gamma\alpha}$ (°C wt%$^{-1}$) | $m^R_{\alpha\gamma}$ (°C wt%$^{-1}$) | $\Delta S_{\gamma\alpha}$ (J mol$^{-1}$K$^{-1}$) |
|---|---|---|---|---|---|
| 700 | 0.014 | 0.79 | -174.53 | -16131.34 | 6.25 |
| | $x^{CR}_{\gamma\theta}$ (wt%) | $x^{CR}_{\alpha\theta}$ (wt%) | $m^R_{\gamma\theta}$ (°C wt%$^{-1}$) | $m^R_{\alpha\theta}$ (°C wt%$^{-1}$) | $\Delta S_{\gamma\theta}$, $\Delta S_{\alpha\theta}$ (J mol$^{-1}$K$^{-1}$) |
| | 1.55 | 0.007 | 289.14 | 12576.41 | 4.26 |

The carbon diffusivity in austenite was derived from the diffusivity database by coupling MICRESS® software with the thermodynamic software, Thermo-calc® and Calphad database [32] in order to include the effect of carbon concentration on the carbon diffusivity. At every prescribed time interval the carbon diffusivity in austenite and ferrite is re-calculated based on the average carbon fraction in each phase.

The heat treatment of the simulation is demonstrated in Figure 4.3.

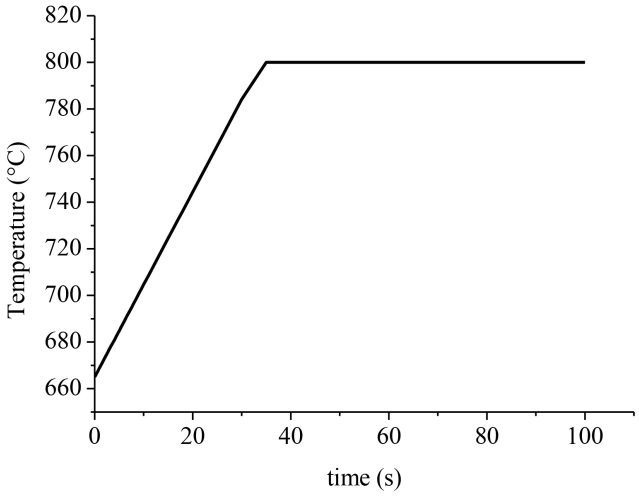


Figure 4.3: Annealing treatment applied in phase-field modelling.

# 5

# Experimental results and discussion

## 5.1. Dilatometry

### 5.1.1. Comparison of dilatometers in TATA steel and TU Delft

Identical dilatometry experiments were carried out, demonstrated in Table 5.1, to compare the dilatometers in TATA steel and in TU Delft.

Table 5.1: Dilatometer experiments of comparison between TATA steel and TU Delft

| | Heating rate (°C/s) | Top temperature (°C) |
|---|---|---|
| HR80 | 80 | 800 |
| HR18 | 18.6 | 680<br>740<br>800 |
| HR4 | 4.4 | 800 |

The maximum cooling rate of each dilatometer while quenching can be estimated by the slope of the cooling curve between 800°Cand 500°C, demonstrated in Figure 5.1. Quenching in dilatometer from TATA steel is performed by air cooling, and the one in TUDelft is by helium cooling. In the latter case a higher cooling rate can be achieved, since helium can provide a higher heat capacity compared to air.

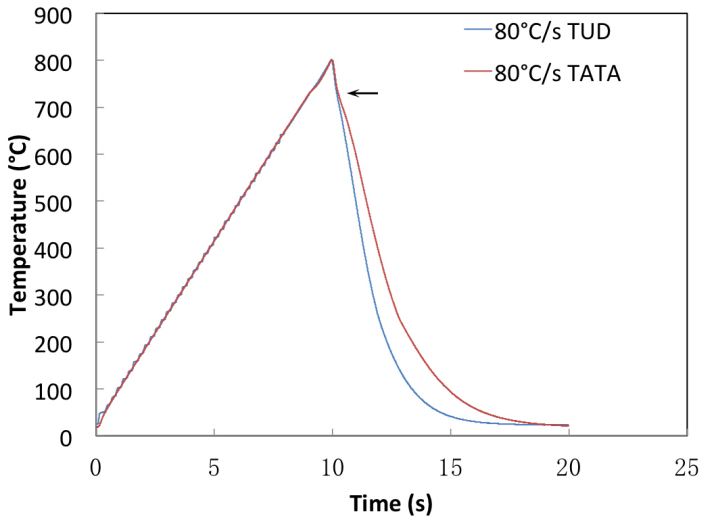


Figure 5.1: Comparison between cooling rates in dilatometers from TATA steel and TU Delft(HR80/800Q).

The estimated maximum cooling rate of dilatometer in TATA steel is around -170°C/s, and the one in TU Delft is around -250°C/s. Both cooling rates are sufficient to avoid transformation from austenite to ferrite+pearlite in this case. It seems at high temperatures, the temperature control in the dilatometer in TATA steel is less accurate, judging by the small horizontal shift at temperatures above 750°C (Figure 5.1 indicated by the arrow).

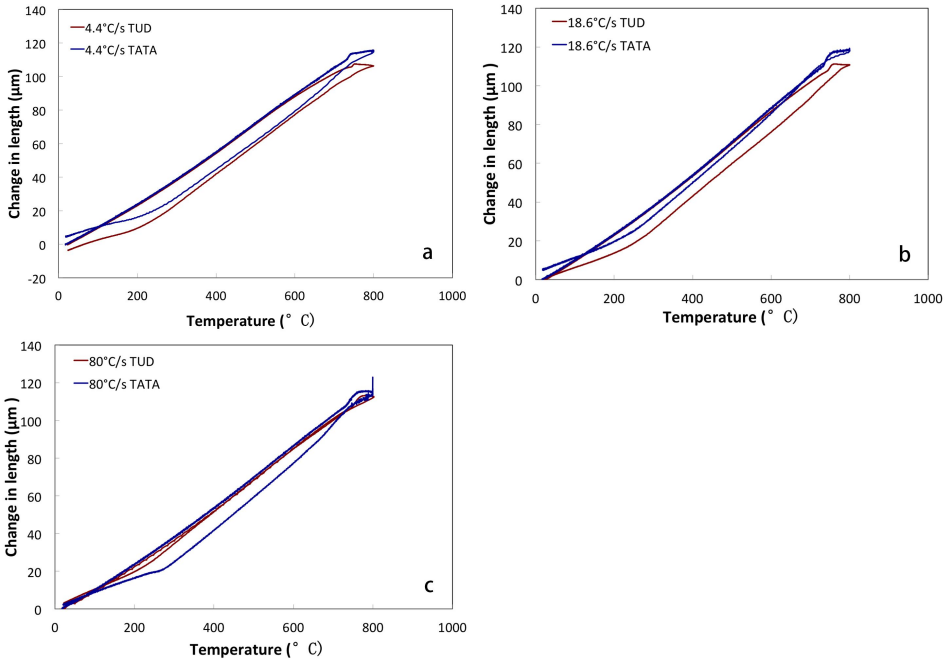


Figure 5.2: Comparison between dilatometers in TATA steel and TU Delft, same top temperature (800°C) with different heating rates: (a) HR4, (b) HR18, (c)HR80.

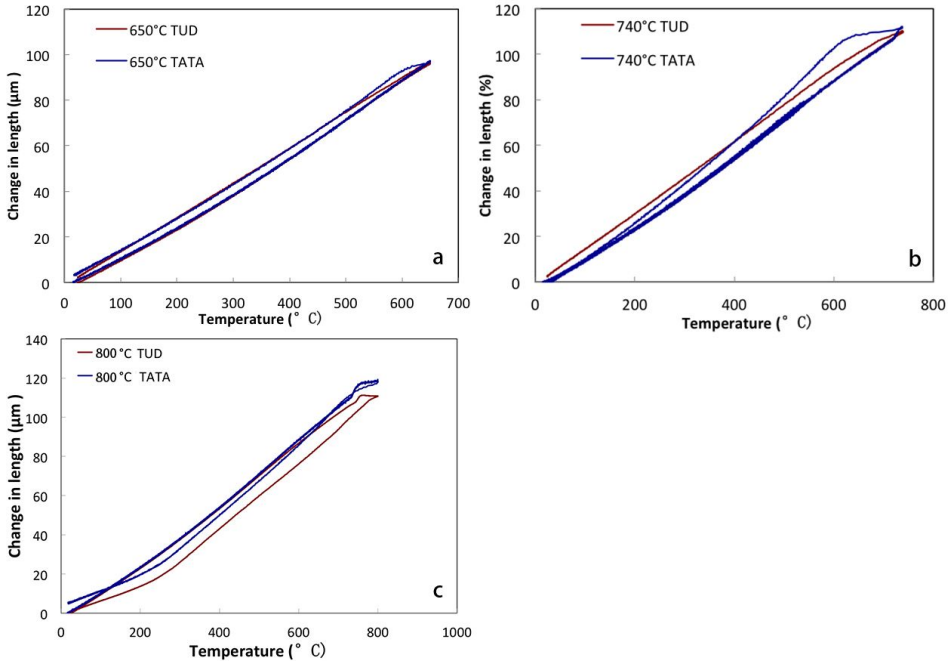


Figure 5.3: Comparison between dilatometers in TATA steel and TU Delft, same heating rate (18.6°C/s) with different top temperatures: (a) 650°C, (b) 740°C, (c) 800°C.

Apart from the small difference in temperature control, the whole dilatation curve shows a significant difference. Figure 5.2 shows the comparison between the two dilatometers with same experiments quenched from 800°C. At lower temperature the two curves seem identical, although the dilatometer in TUD slightly shifted from linear at relatively high temperatures. This could be caused by a different clamping force on the sample in two dilatometers, resulting in creep assisted effects in the samples from TUD. All curves seem to have a small change in thermal expansion coefficient before austenite formation ($Ac_1$ is around 750°C), which can be explained by an inhomogeneous transformation from ferromagnetic to paramagnetic when temperature exceeds the Curie temperature. When part of the material first goes above Curie temperature, the dilatometer responses by increasing HF-Power provided to the sample. This leads to an extra expansion to the un-transformed part of material. The small difference in heating and cooling control seems to result in a big influence on martensite transformation, which may also indicate an influence on austenite formation. The effect is magnified for heating rate 80°C/s (Figure 5.2 (c)). The transformation behavior differs a lot judged by the shape of the cooling curve. In the figure, the curve obtained in TATA steel has sharp turning in the cooling curve when martensite transformation starts, while the curve obtain in TUD is more gradual and without a sharp turning. The martensite transformation temperature also differs by approximately 80 °C. The other curves in Figure 5.2 also have variations when martensite transformation starts but not as obvious as the highest heat rate HR80.

Figure 5.3 gives the comparison with same heating rate (18.6°C/s) and quenched from different top temperatures. The heating curves coincide quite well, except for the 800°Cduring cooling, as discussed above. In the case of 800°C, the two curves start to deviate from around 600°C, while with the same heating rate but quenched from lower temperatures, this deviation does not happen. The reason for this is still unknown, but this is very likely more an instrumental problem than a material phenomenon. What can also be observed from the curve is that the dilatometer of TATA steel is not sufficient by switch heating to cooling, and this will cause some irrational dilation at the beginning of quenching. At the starting point of cooling, both cooling curves in TATA steel with temperatures below $Ac_1$ show a delay in length reduction (Figure 5.3, (a) and (b)), which agrees with the cooling signal in Figure 5.1. As the control of the shift between heating and quenching is more accurate, the dilatometer from TUDelft was chosen to proceed all the relevant experiments in this thesis.

### 5.1.2. Full austenitic annealing

To determine the $Ac_1$ and $Ac_3$ of this material, a full austenitic treatment is applied by heating the sample to 1000°C and holding for 3 minutes. Different heating rates are applied to see the influence on full austenitic transformation. A typical full austenitic treatment dilatometer curve is shown in Figure 5.4. All dilatometer curves are in appendix section C.1. As indicated in the figure, the sample length increases linearly with temperature. Above $Ac_1$ austenite formation starts and the change in length is an effect caused by dilatation of two phases: un-transformed ferrite + pearlite and austenite. Above $Ac_3$, all phases transform into austenite, and the length increases linearly with temperature again until 1000°C. Since the thermal expansion coefficient of ferrite + pearlite and austenite are different, the slope of the two linear parts are different correspondingly. After holding for 3 mins at 1000°C, the sample is quenched with the highest cooling rate of the dilatometer, which is around -200°C/s maximum. The start of the cooling curve is not ideally linear. This could be caused by creep, or an instrumental defect upon quenching from high temperature. When temperature goes below Ms, austenite starts to transform into martensite. After phase transformation is finished, the length decreases linearly with temperature again. The fact that the slope at the end of the cooling curve coincides very well with the slope at the start of the heating curve, indicates that the sample has fully transformed into martensite, and that the amount of retained austenite can be neglected.

#### Determination of $Ac_1$ and $Ac_3$

$Ac_1$ and $Ac_3$ can be determined from the full austenitic annealing dilatometer curves using the lever rule. This is demonstrated in Figure 5.5, which is the high-temperature range taken from the curve in Figure 5.4. As one can see from the curve, before austenite formation, there are irregularities in the linear part of the curve (indicated by the red line). This phenomenon is the same as discussed in subsection 5.1.1, caused by an unsynchronized heating control above Curie temperature. These do not influence the accuracy of the dilatometry data afterwards. However, this does affect the accuracy of linear fit for the lever rule, especially in this case $Ac_1$ is very close to Curie temperature. Still, the linear fit shown in Figure 5.5 gives a very good estimation of the linear increase in dilatation, only that the details at the start of the transformation are lost.

This leads to a sharp start in the austenite formation curve, shown in Figure 5.6, which is against the common knowledge that phase transformation should start gradually.

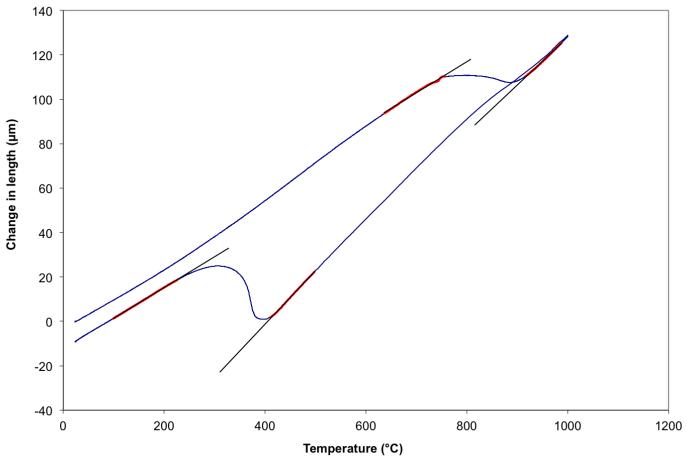


Figure 5.4: Demonstration dilatometer curve of full austenitic annealing, HR4/1000/3minQ (red parts indicate data taken for linear fit of lever rule).

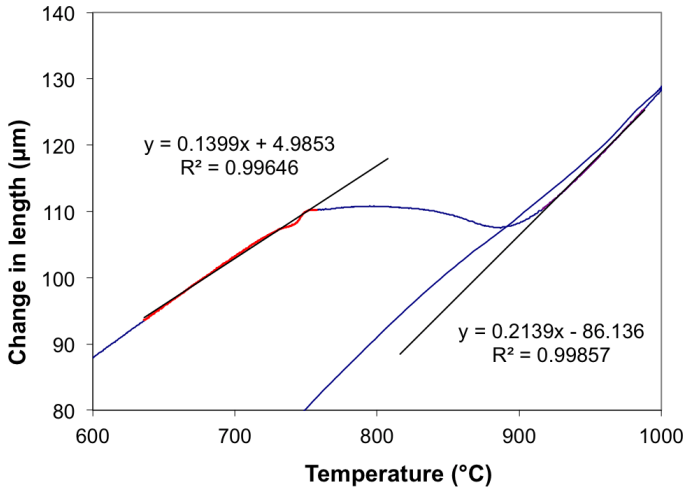


Figure 5.5: Demonstration of heating part of dilatometer curve for fully austenite annealed samples, HR4/1000/3minQ.

Another observation is that the heating and cooling curve near the top temperature do not coincide in Figure 5.5, and variations in both slope and position exist. Similar phenomenon also exist in dilatometer curves with other heating rates (section C.1), both positive and negative shifts exist. This could be caused by an instrumental reason. At 1000 °C, the sample is relatively soft, and the clamping force or any vibration of the machine could cause an unpredictable error in measured length. Nevertheless, this error of change in length at high temperature does not affect the measurement of martensite transformation at lower temperature, which is more relevant to the study.

The austenite formation fractions of different heating rates are plotted in Figure 5.6. Apparently, austenite formation temperature is hardly affected by the heating rates in the range of 4°C/s to 80°C/s. Especially for $Ac_3$, all curves overlap(Figure 5.6), and can be treated as an identical $Ac_3$. Figure 5.7 (b) shows the $Ac_3$ taken

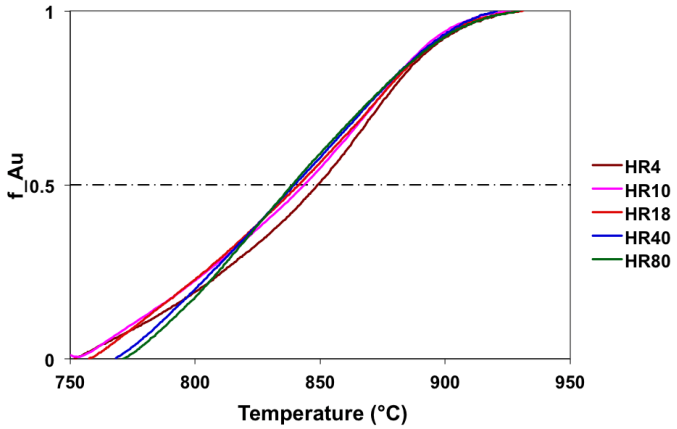


Figure 5.6: Comparison of austenite formation fraction between different heating rates.

from the fraction curve with a transformation fraction above 99% (99%, 99.5% and 1). Considering the end of transformation strongly depends on kinetic factors, $Ac_3$ is taken at 99.5% austenite formation. The variation between $Ac_3$ is around ± 3 °C, and the average $Ac_3$ is 923°C.

On the other hand, $Ac_1$ is more affected by different heating rates compared to $Ac_3$ (Figure 5.7 (a)). Differentiation of fraction from 0% to 1% is not very important, compared to the big difference between different heating rates. Apart from the measurement accuracy, it seems that as heating rate increases, $Ac_1$ gradually increases as well. In other words, $Ac_1$ is slightly delayed for the high heating rates. Notice that this could be caused by a kinetic effect, rather than a thermodynamic effect. It is more reasonable that it is not the equilibrium transformation temperature is different, but the start temperature has a delay in responding to heating, since the heating rate is very high and time taken for this response is considerably very small. Again, $Ac_1$ is taken at the point when 0.5% of the transformation has taken place, and the average temperature is 761°C.

Apart from the difference in $Ac_1$ and $Ac_3$, different heating rates do have an effect on the rate of austenite formation, which is revealed by the slope of the austenite formation fraction curve (Figure 5.6). Since temperature increases linearly with time, a linear transformation fraction indicates a steady rate of transforming from one phase to another. An interesting discovery is that, on the contrary to our common sense that a low heating rate gives a more homogeneous microstructure, this homogeneity does not give a steady transformation. In stead, by applying a high heating rate, which can reserve most of the microstructure close to full hard state, the transformation from ferrite+pearlite to austenite is more linear (Figure 5.6 HR40, HR80) and more homogeneous through out the process, despite of the fact that austenite formation through two-phase region is not linear. And as the heating rate increases from HR4 to HR80, the fraction curve goes closer to a linear transformation. However, we should keep in mind that a higher heating rate within the same temperature region implies a shorter time, and a faster transformation. From HR4 to HR80, the time that the sample stays in two-phase region goes from 37 s to 2 s. This could also lead to the linear transformation phenomenon.

According to literature, theoretical $Ac_1$ is related to the content of alloying elements, and it can be calculated accordingly as:

$$Ac_1 = 754.83 - 32.25C - 17.76Mn + 23.32Si + 17.3Cr + 4.51Mo + 15.62V \text{ [17]}$$

$$Ac_1 = 739 - 22.8C - 6.8Mn + 18.2Si + 11.7Cr - 15Ni - 6.4Mo - 5V - 28Cu \text{ [36]}$$

$$\begin{aligned} Ac_1 = {} & 723 - 7.08Mn + 37.7Si + 18.1Cr + 44.2Mo + 8.95Ni + 50.1V + 21.7Al + 3.18W + 297S - 830N \\ & - 11.5CSi - 14.0MnSi - 3.10SiCr - 57.9CMo - 15.5MnMo - 5.28CNi - 6.0MnNi + 6.77SiNi \\ & - 0.80CrNi - 27.4CV + 30.8MoV - 0.84Cr^2 - 3.46Mo^2 - 0.46Ni^2 - 28V^2 \text{ [18]} \end{aligned}$$

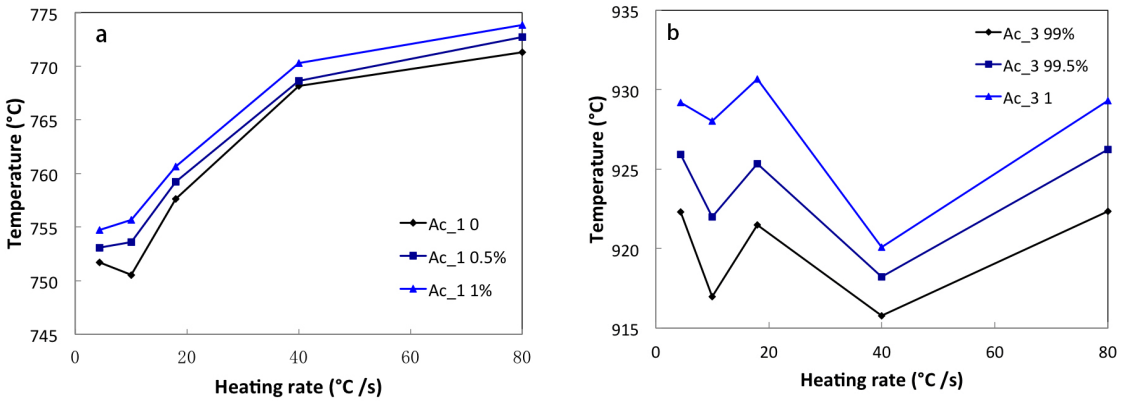


Figure 5.7: Comparison of (a) $Ac_1$, (b) $Ac_3$, as a function of heating rate.

Introducing the composition, neglecting all the irrelevant elements, the equations turn into:

$$Ac_1 = 754.83 - 32.25C - 17.76Mn + 23.32Si + 15.62V = 728^\circ C$$
$$Ac_1 = 739 - 22.8C - 6.8Mn + 18.2Si - 5V = 732^\circ C$$
$$Ac_1 = 723 - 7.08Mn + 37.7Si + 50.1V + 21.7Al - 830N - 11.5CSi - 14.0MnSi - 27.4CV - 28V^2 = 722^\circ C$$

In the equations, each element symbol represents the weight percentage (wt %) of the corresponding element. These results show that $Ac_1$ should be around 730°C, while the results obtained are around 750 °C. The reason behind this is yet unknown, it could be caused by the difference of segregation of subsititutional elements such as Mn, Si in an engineering material, that leads to early transformations at low temperature. This indicates, that estimations based on these equations does not match perfectly with the material studied in this thesis, and that it is not quantitatively reliable.

By neglecting the small differences between different heating rates, we can obtain the austenite fraction at the chosen intercritical annealing temperature (800°C) is about 20%. At 800°C, carbon in ferrite is considerably low compared to austenite. Thus, by considering all carbon exist in austenite, and assuming at this temperature the microstructure consist of ferrite + austenite, we can obtain the carbon content of austenite at 800°C to be approximately 0.75%.

### Influence of heating rate on Curie temperature

The sample is heated by an induction coil from room temperature to the soaking temperature. As we know steel is a ferromagnetic material at room temperature. By induction from room temperature, the alternating magnetic flux field causes the magnetic dipoles of the material to oscillate as the magnetic poles change their polar orientation every cycle, known as *hysteresis*[16]. A minor amount of heat is produced due to the friction produced when the dipoles oscillate. When steels are heated above Curie temperature they become nonmagnetic, and hysteresis ceases. When steel transforms from ferromagnetic to paramagnetic state, extra energy is needed to heat up the material. Thus Curie temperature can be determined by the steep rise in the curve of applied HF-Power versus temperature, demonstrated in Figure 5.8. In order to better interpret the deflection point of the curves, derivative method discussed in Figure 3.2.4 is applied. The first derivative of the HF-Power signal is plotted in Figure 5.9. The red arrow in the plot indicates a sharp deflection point in the curve, which is the Curie temperature. Apparently, the error of $T_C$ is very small. Figure 5.8 shows that different heating rates do not influence the Curie temperature, plotted in Figure 5.10. All Curie temperatures are within a range of around 5 °C. Hence, it can be considered that Curie temperature is independent of heating rates, and is taken by the average as 747°C. The typical Curie temperature of carbon steels is around 760 °C[16].

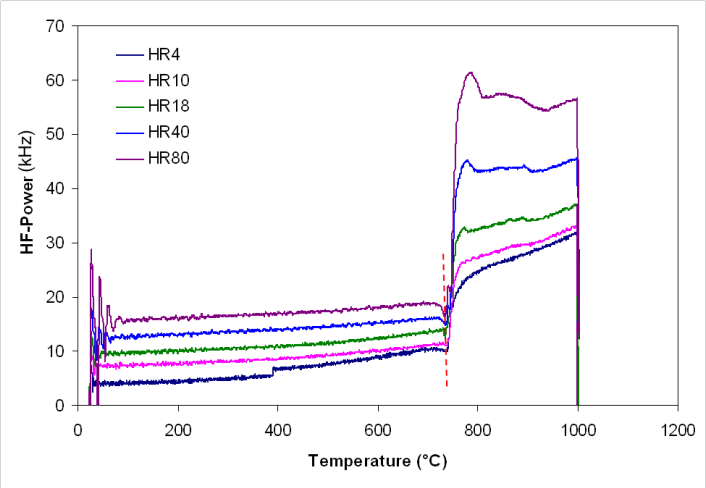


Figure 5.8: Comparison of HF-Power between for heating rates.

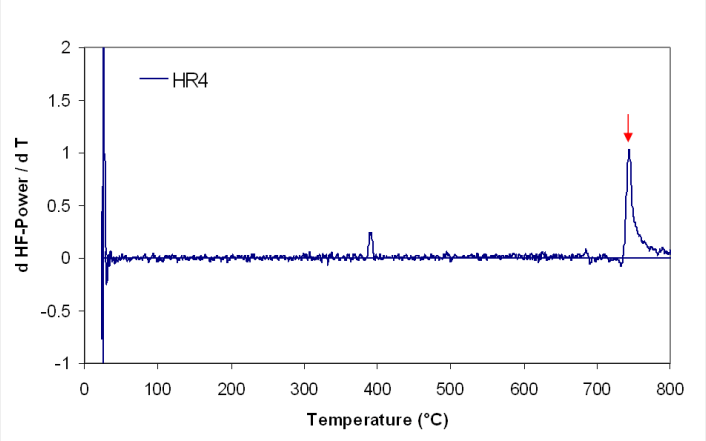


Figure 5.9: First derivative of HF-Power versus temperature, HR4/1000/3minQ.

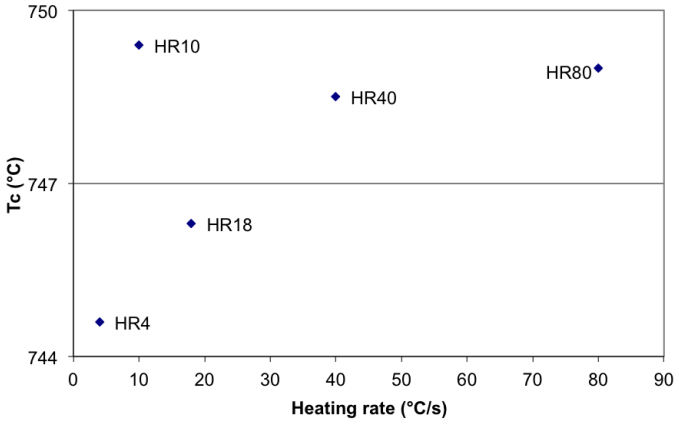


Figure 5.10: Comparison of Curie temperature as a function of heating rates.

### Influence of heating rate on martensite transformation temperature (Ms)

Similar to austenite formation, martensite transformation fraction can also be estimated by applying lever rule to the cooling part of dilatometer curve, and the results are shown in Figure 5.11. It shows that unlike $Ac_1$ and $Ac_3$, Ms is very sensitive to heating rate. The Ms taken from the dilatometer curves, using the method discussed in subsection 3.2.4, is listed in Table 5.2, together with $Ms_{10\%}$ from the fraction curves. In this discussion, Ms is more important and reveals a materials property, $Ms_{10\%}$ is for the convenience of the following discussions from an engineering perspective.

The lower heating rates (HR4, HR10, and HR18) have an identical Ms, 386°C, while the high heating rates have a higher Ms. The difference is around 15 to 20 °C. As discussed in subsection 2.1.6, studies have tried to quantify the influence of alloying elements on the phase transformation temperatures ([2][9][21]) as follows:

$$Ms = 539 - 423C - 30.4Mn - 17.7Ni - 12.1Cr - 11.0Si - 7.0Mo \text{[2]}$$
$$Ms = 550 - 350C - 40Mn - 35V - 20Cr - 17Ni - 10Cu - 10Mo - 8W + 15Co + 30Al \text{[9]}$$
$$Ms = 539 - 423C - 30.4Mn - 7.5Si - 30.0Al \text{[21]}$$

Neglecting all the irrelevant elements, the equations become:

$$Ms = 539 - 423C - 30.4Mn - 11.0Si = 407^\circ C$$
$$Ms = 550 - 350C - 40Mn - 35V + 30Al = 425^\circ C$$
$$Ms = 539 - 423C - 30.4Mn - 7.5Si - 30.0Al = 397^\circ C$$

In the equations, each element symbol represents the weight percentage (wt %) of the corresponding element. All the estimations are around 400 °C, which falls in the range of the results from the experiments (Figure 5.12). Since all samples are with full austenitic microstructure, the alloying elements content should be the same, and that this difference of Ms is caused by austenite grain size. As discussed in subsection 2.1.6, a larger austenite grain size will lead to a higher Ms temperature. This means as the heating rate increases, the austenite grain size increases as well. Because the holding time for all heating rates is the same, this differentiation in grain size should originate from heating. This could be caused by the fact that with a high heating rate, a lot of deformation energy is stored inside the microstructure, and that once austenitization starts, extra driving force is provided for the transformation, resulting in a higher growth rate of austenite.

Another hypothesis is that, the difference in austenite grain size is actually related to different austenite formation mechanisms. The phenomenon that HR4, HR10, and HR18 have the same Ms, also supports this hypothesis, since one would also expect a difference in stored energy in those three heating rates. It is possible that the three low heating rates are with similar transformation mechanism, and that they will form austenite in a similar way with similar size.

Table 5.2: Ms of fully austenite annealed samples

| Sample code | Ms (°C) | $Ms_{10\%}$ (°C) |
|---|---|---|
| HR4 | 386 | 390 |
| HR10 | 386 | 385 |
| HR18 | 385 | 388 |
| HR40 | 408 | 419 |
| HR80 | 397 | 407 |

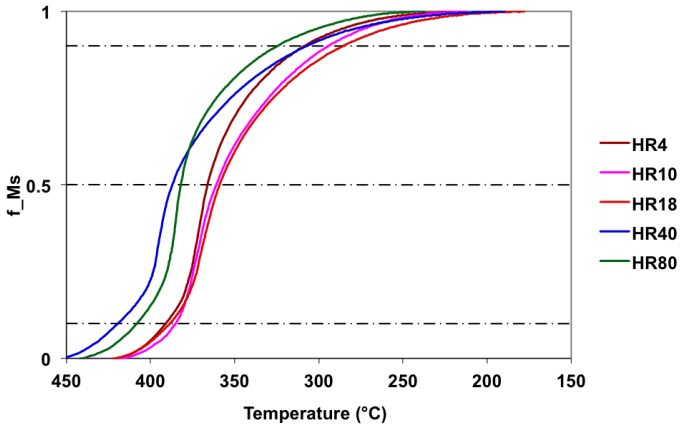


Figure 5.11: Martensite transformation fraction as a function of different heating rates.

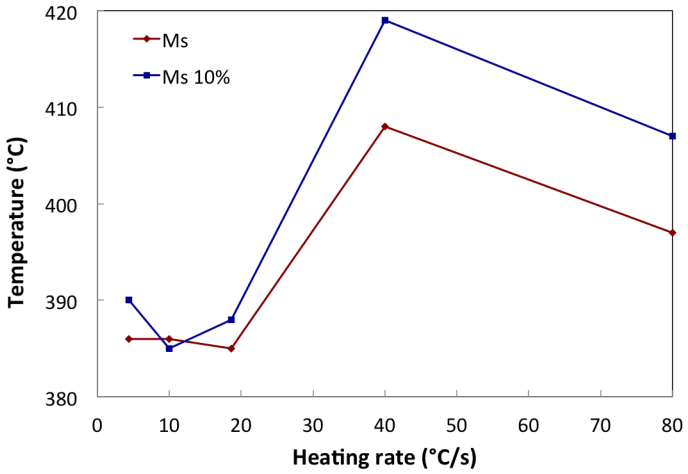


Figure 5.12: Comparison of Ms between different heating rates.

### 5.1.3. Intercritical annealing

A typical intercritical annealing sample's dilatometer curve is demonstrated in Figure 5.13. The beginning of heating part is similar to full austenitic annealing samples, but till a top temperature of 800°C. The sample is held at 800°C for 10 s, during which time austenite formation still proceeds, resulting in a decrease of length. After the holding is completed, quenching is applied to the sample, and the length decreased linearly with time. The non-linear behavior at the beginning of quenching is similar to full austenitic annealing samples, and was discussed in subsection 5.1.2. Below a certain temperature, austenite starts to transform into martensite. For the same reason of inhomogeneity discussed in the previous section, martensite transformation takes place over a range of temperature. As the contraction becomes linear, martensite transformation is completed. The slope at the end of the cooling curve does not collaborate well with the slope at the start of heating. This is because austenite partially transformed into martensite, so that a certain amount of retained austenite still exist in the final microstructure at room temperature. The slope at the end of the cooling curve is an overall effect of the thermal expansion from untransformed ferrite, martensite, and retained austenite.

Lever rule is applied to the cooling part to obtain martensite transformation fraction. Due to the fact that intercritical annealing with various time could cause a very big differentiation in austenite formed at high temperature, the start of martensite transformation does not reveal the overall property of the microstructure. Thus, for an engineering point of view, martensite transformation temperature is taken at the point when 10% of martensite transformation has completed. Although theoretically this martensite transforma-

tion temperature is not the same as the Ms from full austenitic annealing samples (which is a characteristic property of the material), for the convenience of discussion here, this temperature will also be stated as Ms in this thesis.

Dilatometer cycles for intercritical annealing samples are listed in Appendix B, and all relevant dilatometer curves are listed in section C.2. Samples are analysed by SEM.

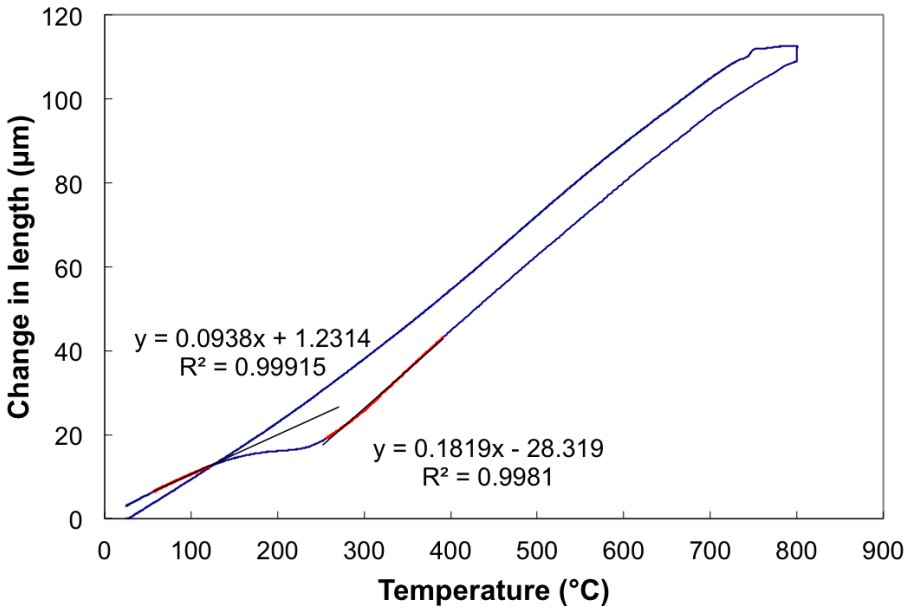


Figure 5.13: Dilatometer curve from intercritical annealing samples, HR4/800/10sQ.

### 5.1.4. Investigation of error in "Ms" measurements

From the previous discussion we can see that Ms is very sensitive to heating rate, and that this can reflect the austenite formation mechanism at high temperatures. However, the accuracy in the Ms measurement is still unknown. Two main factors that can cause deviations are investigated in this thesis: welding position, and manual operation.

#### Error caused by welding position

As described in subsection 3.2.2, four welding positions were applied for the dilatation tests using a heating rate 18.6 °C/s, top temperature 800°C, and holding time 0 sand 60 s. Each point was measured twice to improve statistics. Sample codes and details are 5listed in Appendix A. For directly quenched samples, Ms was determined by derivative of the cooling curve as discussed in subsection 3.2.4. For samples with holding time 60 s, Ms was determined by the temperature when 10% was transformed, which can be obtained from the fraction curve. The results are plotted in Figure 5.14 and Figure 5.15. The dashed line in the figure represents the result from each pair of experiments, and the solid line is the average value taken from the two experiments.

Figure 5.14 gives the Ms by different welding positions of directly quenched samples. Both $Ms_{0\%}$ and $Ms_{99\%}$ taken from the derivative curve are plotted in the same figure. Obviously, the largest error of 50°C is caused by welding position C, which is asymmetrically welded. Ms of other welding positions lie in between position C and standard position, and position A and D even appears that they hardly introduce any error. Another observation is that most of the error caused by different welding positions are positive. This is probably an overall effect from the measuring method of dilatometer.

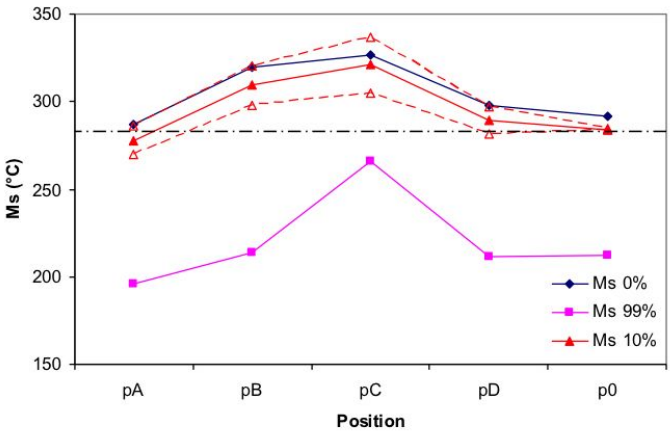


Figure 5.14: Ms versus welding position, directly quenched (EB/HR18/800Q).

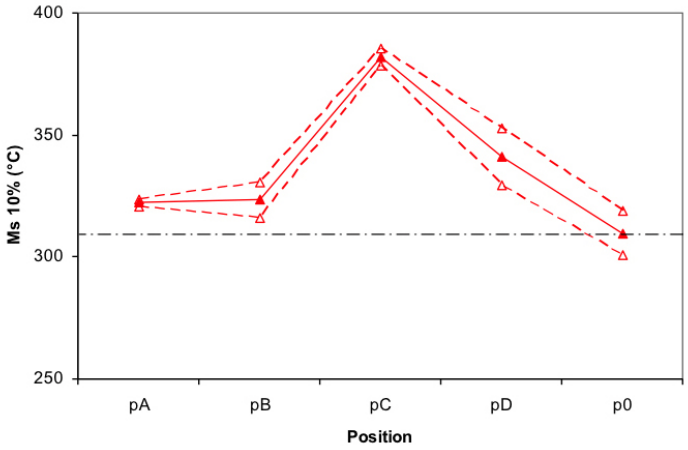


Figure 5.15: Ms versus welding position, holding time 60 s(EB/HR18/800/60sQ).

Since temperature control of the dilatometer is based on the thermo-couple signal, an asymmetric welding can cause an actual different thermal cycle. Due to instrumental reasons, both heating and cooling of the sample is not homogeneous over the length, and a temperature gradient exists. In other words, at near-top-temperature region, samples with different welding positions may catch the top point "800°C" at different stages of the heating process. When the signal of 800°C is reached, the program will shift the machine to quench, while in fact the temperature distribution of each sample is different. At the onset of austenite formation, this small difference in thermal cycle could cause a large influence on austenite formation, and affect the measured Ms. Thus, this error in Ms for directly quenched samples, is a combination of both in-accurate heating control at high temperature, and an in-accurate temperature capture of the sample when martensite transforms.

For samples with holding time 60 s, this in-accuracy of heating control can be neglected, assuming that the holding time is long enough to ensure temperature homogeneity. Although the holding time can slightly differ, slight differences in holding will not severely affect the microstructure and phase transformation. Thus, the error plotted in Figure 5.15 is mainly caused by a different temperature captured by the thermal couple, due to a thermal gradient induced by quenching. Coincidentally, this reveals a similar influence as the directly quenched samples. Still, the largest error is caused by position C, which is around 80°C, and the other positions lie in between. Compared to standard position, position C can be considered as measuring the temperature 2 mm away from the center of the sample. If the martensite transformation is considered to start at the same temperature in the center of the sample, regardless of where the thermo-couple is welded, position

C in fact reflects the temperature 2 mm away from center when martensite transformation starts. In this way we can roughly estimate the thermal gradient of cooling from the center of the samples is around 40 °C/mm. Although this difference is significant, the cooling rate during quenching is around -200°C/s. Thus, this thermal gradient will only introduce an error of the measured Ms, but not to the actual martensite transformation throughout the sample. Same as the directly quenched samples, all the error caused by different welding positions are positive. Position A and B do not introduce a significant error. This may lead to a experience-based conclusion that, as long as the welding points are symmetric, the error is acceptable. It is also worth stressing that, all welding positions are intentionally chosen to be odd, and that in a standard dilatometer test, the welding is nowhere near any of the circumstances we discussed before. This will lead to the conclusion that, a small difference in welding position is not a main source of error in Ms measurements.

### Error caused by operation

Repeating a same set of experiments may still introduce error, this is referred to as error caused by operation. Error of repeating the experiments over time could be caused by environmental conditions, which will affect the working condition of the machine. In the same time period, apart from some rare odd error from instrumental or sample fluctuation, error still exists. Experimental error comprises variation in welding, sample condition, and the instrumental condition. In order to investigate this error, experiments of heating rate HR4 and HR18 are repeated over time. The first set of experiments were done in March, and the second set in April. Some points are repeated twice to see the error by repeating in the same time period. The experiments are listed in Table 5.3. Detailed information of samples in this section can be found in Appendix A.

The corresponding results are plotted in Figure 5.16. For experiments repeated in April, the average Ms from the two experiments are plotted, and the difference is plotted as an error bar in the figure. For HR4, the repeated experiments in April is very reproducible, the error bar is around ±8 °C. However, compared between March and April, Ms with holding time less than 60 s differs a lot, with a maximum error of 45 °C. Although samples with holding time over 1 min have a small error. In June another set of the same experiments are carried out, and the results are also presented in Figure 5.16. The data in June shows a similar trend as the one in April, and the biggest error is below 20 °C. The reason for the difference between April and March is still unknown, this could be caused by a fluctuation in samples. For HR18, all results differ within a range of ±10 °C, maximum 27 °C. And the trends from the two sets of experiments correspond with each other quite well.

In general, the measurement of Ms is not very accurate, and an error bar is estimated at ±10-15 °C. Even so, with the most similar conditions (time period, sample, etc), error could stay within ±10 °C in one series. Another observation is that, Ms data could only be compared in series, rather than as separate data points from different time period. This is due to an instrumental drift, and only data from the same time period under identical conditions are comparable with each other. Possible source of error could be: welding position, insufficient cooling, sample fluctuation, machine signal delay, etc.

Table 5.3: Thermal cycles for error investigation

| | Holding time (s) | Experiment date | Repeated times |
|---|---|---|---|
| HR4 | 0 | Mar | 1 |
| | | Apr | 2 |
| | | Jun | 1 |
| | 5 | Mar | 1 |
| | | Apr | 2 |
| | | Jun | 1 |
| | 10 | Mar | 1 |
| | | Apr | 1 |
| | | Jun | 1 |
| | 30 | Mar | 1 |
| | | Apr | 2 |
| | | Jun | 1 |
| | 60 | Mar | 1 |
| | | Apr | 2 |
| | | Jun | 1 |
| | 180 | Mar | 1 |
| | | Apr | 1 |
| | | Jun | 1 |
| HR18 | 0 | Mar | 1 |
| | | Apr | 2 |
| | 5 | Mar | 1 |
| | | Apr | 1 |
| | 10 | Mar | 1 |
| | | Apr | 1 |
| | 30 | Mar | 1 |
| | | Apr | 2 |
| | 60 | Mar | 1 |
| | | Apr | 2 |
| | 180 | Mar | 1 |
| | | Apr | 1 |

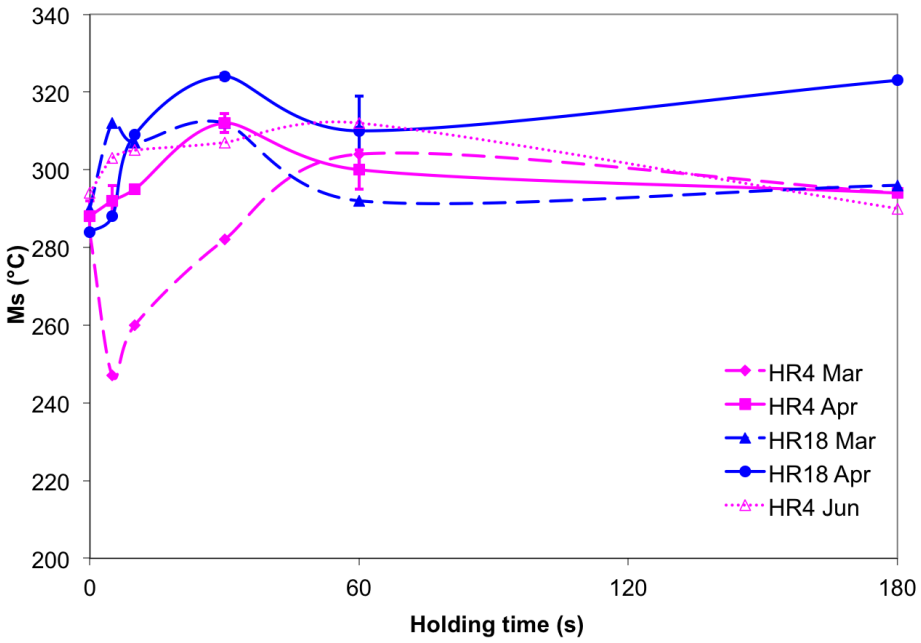


Figure 5.16: Ms from experiments over time versus holding time, HR4 and HR18.

## 5.2. Evolution of microstructure during annealing

### 5.2.1. Microstructual evolution below $Ac_1$

Samples HR4, HR18 and HR80, are heated to 650°C, 680°C, 720°C, and 740°C, and analyzed under SEM Figure 5.17.

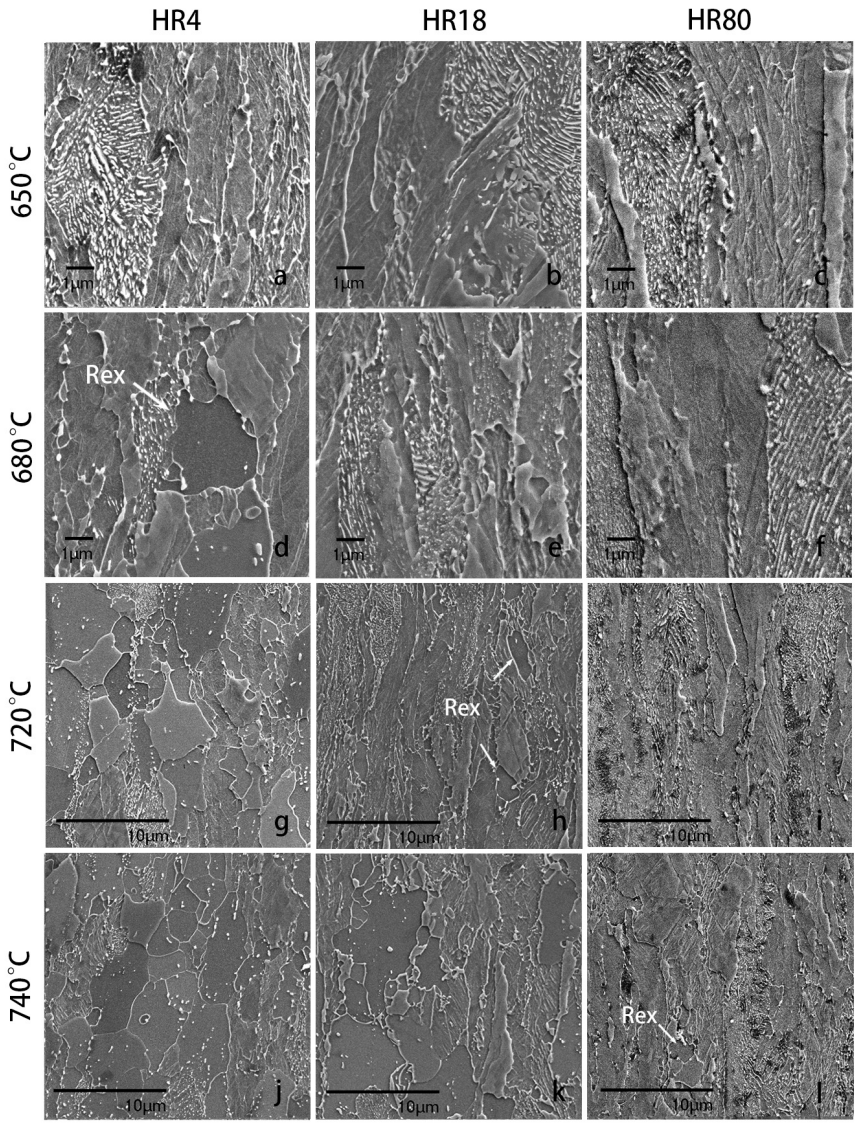


Figure 5.17: SEM result of different heating rates: (a) HR4/650Q; (b) HR18/650Q; (c) HR80/650Q; (d) HR4/680Q; (e) HR18/680Q; (f) HR80/680Q; (g) HR4/720Q; (h) HR18/720Q; (i) HR80/720Q; (j) HR4/740Q; (k) HR18/740Q; (l) HR80/740Q. $(a)-(f)$ $SEI$, ×5000; $(g)-(l)$ $SEI$, ×2000, *Rolling direction is vertical.*

At 650°C, all samples have gone through some extent of recovery, but recrystallization was not observed. Although it is hard to conclude, it seems that recovery is extensive at lower heating rate, judged by a first estimation of the cell size inside the ferrite colonies (Figure 5.17, (a)-(c)). Since recovery is a thermal assisted process, a lower heating rate means additional soaking with temperature, resulting in recovery.

First nucleation of recrystallized ferrite of HR4 is observed at 680°C, with the appearance of strain-free ferrite grains in the microstructure (Figure 5.17, (d) indicated by the arrow). The recrystallized grains can be charac-

terized by absence of substructures inside the equiaxial grain. The recrystallized grain size at this temperature is about 3-4 $\mu$m.

At 720°C, at the lowest heating rate of HR4, recrystallized fraction is around 50%. Meanwhile lamellar pearlite in HR4 has disappeared, instead the cementite has spheriodized and are scattered among the recrystallized ferrite grains. Some degraded pearlite turns into spheriodized cementite carbides and stay close to the original pearlite band. Recrystallization in HR18 just started, indicated by the arrows (Figure 5.17, (g)-(i)). The recrystallization fraction is under 10%. (Recrystallization fraction is an estimation from the SEM microstructure.) As for HR80, no big changes are present yet.

At 740°C, HR80 also starts to recrystallize, indicated by the white arrow (Figure 5.17, (j)-(l)). According to the dilatometer tests, $Ac_1$ is around 750°C, so 740°C is almost the start microstructure before austenite formation. For HR4, from 680°C to 740°C, the heating time is:

$$\frac{(740-680)^\circ C}{4.4^\circ C/s} = 13.6s$$

The recrystallization fraction increases from below 10% to around 90%, indicating that the recrystallization process is very fast, and a reliable conclusion is that recrystallization is almost finished before $Ac_1$, hence 750°C. The recrystallized ferrite grain size is around 5 $\mu$m, and grains are slightly elongated along the rolling direction. Lamellar pearlite degraded, and spheriodized carbides are scattered inside the ferrite grains, some still are present in bands. For HR18, recrystallization fraction is around 50%. Similar to HR4, pearlite has also degraded. From 720°C to 740°C, the heating time is:

$$\frac{(740-720)^\circ C}{18.6^\circ C/s} = 1.1s$$

The recrystallization is even faster than HR4. Apparently, with a higher heating rate, there is more stored energy reserved inside the structure, and hence both nucleation and growth proceed faster. For HR80, recrystallization fraction is less than 10%, it can be deduced that most of the stored energy is still reserved inside the ferrite.

To conclude, recystallization temperature increases with heating rate, as was also observed by Mumford et al. [23]. The earliest recrystallization of all samples starts at 680°C, forming uni-axial grains among deformed ferrite grains. At the same time, increase of the heating rate helps preserving deformation energy inside the lattice to a higher temperature. Both higher driving force and higher deformation energy at advanced temperature will speed up recrystallization.

While ferrite recrystallises, lamellar pearlite degenerates and forms spherical cementites. This observation agrees with Huang et al. [14]. Another observation is that, recrystallized ferrite nuclei do not only grow into un-recrystallized ferrite grains, but also into the ferrite areas between lamellar cementite in a pearlite colony. This could increase the surface energy of the lamellar cementite morphology. With spheriodizing, the surface area between cementite and ferrite reduces, which is thermodynamically more stable. This degradation of pearlite involves carbon diffusion in ferrite lattice, leading to carbon re-distribution and homogenization before austenite formation starts. From Figure 5.17 (d) to (g) and (j), it is obvious that the recrystallization process coincides with the degradation of pearlite. The recrystallization fraction can in a way reveal the degree to which pearlite degrades. Judged by the microstructure pictures, the more ferrite recrystallizes, the more cementite degrades.

Since recrystallization forces elongated ferrite into uni-axial grains, and spheriodization re-distributes carbon outside the orginal pearlite colonies, this evolution before $Ac_1$ can reduce the banding structure. Although substitutional alloying elements such as manganese and silicon can hardly diffuse during this process, considering the time scale and temperature, this effect on banding structure will still influence austenite formation.

### 5.2.2. Microstructure at 800°C

From the experiments of fully austenitic annealing discussed in subsection 5.1.2, different heating rates seem to influence the austenite formation by controlling carbon diffusion, and this also affects Ms temperature.

Further experiments were carried out to see if Ms changes with heating rate. Heating rates of 2°C/s, 4.4°C/s, 10°C/s, 18.6°C/s, 40°C/s, 60°C/s, and 80°C/s were applied, and all samples are heated to 800°C and quenched (see Table 5.4).

Table 5.4: Sample preparation for dilatometer

| Sample code | Top temperature (°C) | Heating rate (°C/s) |
|---|---|---|
| HR2 | | 2 |
| HR4 | | 4.4 |
| HR10 | | 10 |
| HR18 | 800 | 18.6 |
| HR40 | | 40 |
| HR60 | | 60 |
| HR80 | | 80 |

As discussed in subsection 3.2.4, there are two methods to determine the Ms of directly quenched samples, both are plotted in Figure 5.18. Data marked with *"Mar"* is determined by the deflection point of the cooling curve, and data marked with *"Derivative"* is determined by the deflection point in the first derivative of cooling curve. It is clear that the Ms taken from the deflection point of the cooling curve lies between $Ms_{0\%}$ and $Ms_{99\%}$ from the derivative curve. $Ms_{10\%}$ obtained by derivative method are used, because of its relatively smaller error bar. Despite of the error bars, there is a significant trend that heating rate affects Ms temperature. Samples are also examined with SEM (Figure 5.20).

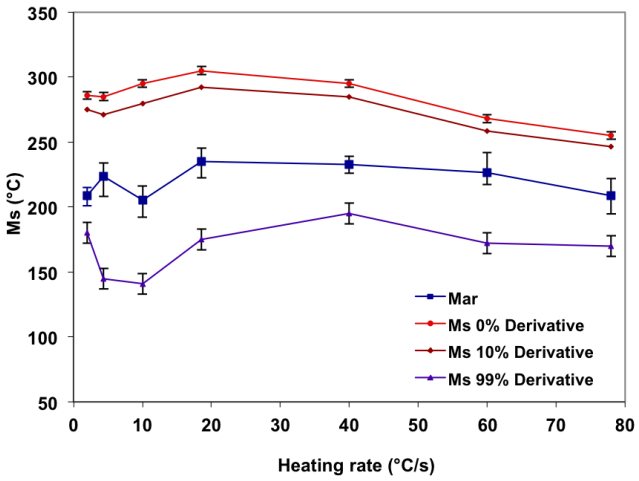


Figure 5.18: Influence of heating rate on Ms temperature determined by different determination methods, directly quenched samples. Data marked with $Mar$ is determined by the deflection point of the cooling curve, and data marked with $Derivative$ is determined by the deflection point in the first derivative of cooling curve.

There are two main factors affecting Ms temperature (discussed in subsection 2.1.6): carbon content and austenite grain size. During quenching, austenite has just started to nucleate. During this stage, austenite nuclei are very small and have similar size as shown by SEM (Figure 5.20). It is assumed that, the influence of austenite grain size on Ms can be neglected. Studies ([2][9][21]) have found out that, higher Ms temperature is related to lower carbon content. Ms from all heating rates range within 50°C(Figure 5.18). Neglecting the inhomogeneity of substitution elements as Mn, Si and Al, the carbon content of austenite can be estimated based on the following equation[2] (the element symbols in the equations represents the composition of the corresponding element in wt %):

$$
\begin{aligned}
Ms &= 539 - 423C - 30.4Mn - 17.7Ni - 12.1Cr - 11.0Si - 7.0Mo \\
&= 539 - 423C - 30.4Mn - 11.0Si \\
C &= (472^{\circ}C - Ms)/423^{\circ}C/(wt\%)
\end{aligned}
$$

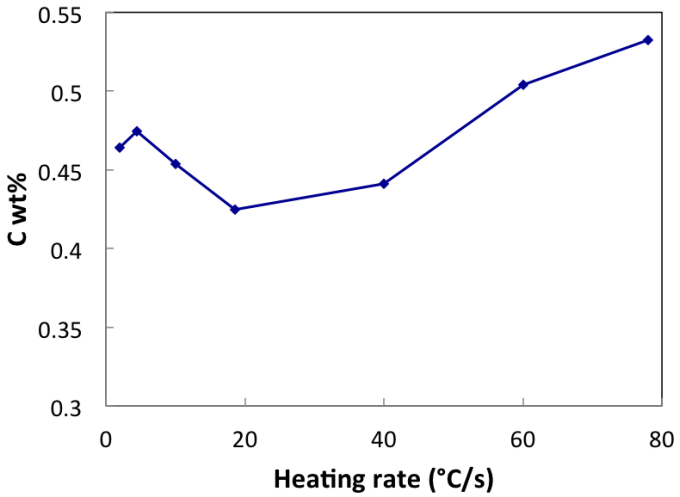


Figure 5.19: Estimated of carbon content in austenite for directly quenched samples at 800°C.

Table 5.5: Estimated C wt% of full austenitic annealing samples

| Sample code | Ms (°C/s) | Calculated C wt% |
|---|---|---|
| HR4/1000/3minQ | 386 | 0.20 |
| HR10/1000/3minQ | 386 | 0.20 |
| HR18/1000/3minQ | 385 | 0.20 |
| HR40/1000/3minQ | 408 | 0.15 |
| HR80/1000/3minQ | 397 | 0.18 |

The results are plotted in Figure 5.19. Before discussing the results, the reliability of this estimation can be evaluated by applying the same equation on full austenitic annealing samples, with data taken from Table 5.2. The estimated carbon concentrations are listed in Table 5.5. Since all samples listed consist of fully austenite, the carbon content of all samples should be ideally be identical, hence, 0.15%. It is the austenite grain size that cause this difference in Ms, rather than carbon content, and this factor is not relevant in the equation. This indicates that, the actual calculated value from the equation cannot reveal the real carbon content of the material, but the trend from the same set of experiments is valid and reliable. Figure 5.19 shows that different heating rate can cause a difference in carbon content of maximum 0.1%. Remember that this Ms is taken from the onset of martensite transformation ($Ms_{10\%}$), i.e., the austenite that transformation first in the material with the highest Ms and lowest carbon content. The increasing of Ms from HR18 to HR80 seems to indicate that the average lowest carbon content in austenite increases as heating rate accelerates. However, considering the limited fraction of austenite formed at this stage of transformation, and the inaccuracy of Ms measurement, it is hard to draw further conclusions, and further studies are needed.

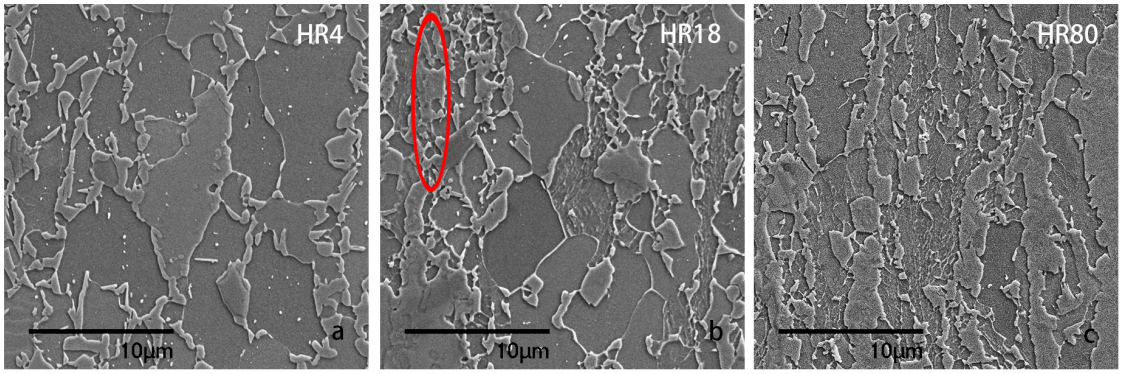


Figure 5.20: SEM results at 800°C, directly quenched samples, (a) HR4, (b) HR18, (c) HR80. *SEI*, ×2000, *rolling direction is vertical.*

The microstructure already reveals strong differences between different heating rates (Figure 5.20). At 800°C, all samples are above $Ac_1$. Austenite formed in the two-phase region will turn into martensite or retained austenite upon quenching, and this is known as martensitic austenite colonies (MA). MA constituents can be determined by the acicular substructure inside the grains. By applying different heating rates, the extent to which recrystallization and austenite formation interfere can be adjusted. In Figure 5.20 (a), austenite nuclei mainly distribute at ferrite-ferrite grain boundaries, and the structure is nearly fully recrystallized before phase transformation. Some cementite spheres still remain un-dissolved in ferrite, and appear as white dots under SEM. Whereas for HR18, ferrite is still partially un-recrystallized. A similar morphology as HR4 in the recrystallized ferrite areas is observed, only that less austenite nuclei exist on ferrite-ferrite grain boundaries. A distinction between HR4 and HR18 is that, there is an area in HR18 that austenite nuclei form a elongated net, indicated by a circle in Figure 5.20. This could be austenite formed from former pearlite colonies. It is well accepted that austenite nucleates and grows faster from pearlite than from ferrite-ferrite grain boundaries, because pearlite provides austenite with a richer carbon source and a shorter diffusion distance. When pearlite colonies still exists in the microstructure, austenite will always nucleate first at these sites. As stated in the three-step austenite formation mechanism in subsection 2.1.4, austenite will first grow in pearlite until consuming all pearlite, before further growth into ferrite. Although in this case it is more complicated due to the degradation of pearlite, un-dissolved pearlite will still form austenite above $Ac_1$. As for HR80, it is clear that there is still a significant amount of non-recrystallized ferrite, and that austenite mainly forms from former pearlite colonies. Notice that ferrite continues to recrystallize above $Ac_1$ with an even higher driving force due to the high temperature. The newly recrystallized ferrite grains grow rapidly between pearlite bands. However, at this temperature pearlite bands have transformed into austenite, which will hinder ferrite recrystallization.

To conclude, at temperatures above 800°C, heating rate influences the interaction between recrystallization and austenitization, by controlling recrystallization and pearlite degradation. Austenite nucleation sites strongly depend on the microstructure below $Ac_1$. For recrystallized ferrite, cementite spheriodizes before $Ac_1$, and austenite mainly nucleates at ferrite-ferrite grain boundaries. This involves the diffusion of carbon, from cementite spheres to ferrite grain boundaries. For un-recrystallized ferrite structures, pearlite remains in lamellar morphology, and austenite mainly nucleates at the pearlite colonies. Since pearlite provides a rich carbon source, and the diffusion length is small, this process is faster compared to the previous circumstance. While austenite grains nucleate and grow, recrystallization of ferrite continues. The growing ferrite grain boundaries can be blocked by the austenite grains, restricting further ferrite growth.

### 5.2.3. Microstructural evolution with varying holding times at 800°C

To further observe austenite formation at intercritical temperature, samples are heated to 800°C and soaked for various times, with details listed in Table 5.4. All samples except holding time of 10 s are examined by SEM

(Figure 5.21).

Compared to the directly quenched samples (Figure 5.20), during the first 5 seconds, austenite in HR4 has grown in size. More austenite nuclei also formed, since the ferrite-ferrite grain boundaries are nearly all covered by austenite nuclei. As holding time increases to 30 s and 1 min, austenite grows normally from the grain boundaries into the ferrite bulk with a rather low speed. The austenite grain size hardly increases from 30 sto 1min. Because of this low growth rate, the carbon trapped inside the ferrite bulk can also nucleate. Compared to nucleation at grain boundaries, nucleation inside bulk introduces more surface energy and distortion energy. One way to reduce this induced energy is to form coherent interfaces, indicated by the green arrow in Figure 5.21 (d). There are also round-shaped austenite colonies inside the ferrite bulk (Figure 5.21 (c)), which could be a cross section of the previous one, resulting from different orientations during preparation. Still, austenite inside the bulk is only observed after longer holding time, from 1 min up to 3 min.

Different morphology is seen in HR80 (Figure 5.21 (i)-(l)). As discussed before, pearlite colonies are still present inside the microstructure, which will transform into austenite first (indicated by the red circle in Figure 5.21 (i)). Apart from pearlite colonies, austenite can also nucleate at cell walls of un-recrystallized ferrite areas, indicated by red arrows in Figure 5.21 (i) and (j). It is also clear that recrystallization coincides with phase transformation. As indicated by the blue arrow in Figure 5.21 (i), the growing front of a recrystallized ferrite grain is pinned by an austenite nucleus. Huang et al.[14] has argued, this moving grain boundary does not provide suitable nucleation site for austenite. As a result, the remaining carbon trapped inside ferrite bulk before recrystallization, will enable nucleation at the interfaces, where the energy state is more preferable. Once those nuclei form at the cell walls inside un-recrystallized ferrite, further recrystallization will be suppressed, since there are pinning points throughout in the structure. In addition, the austenite that formed on the corners of cells will also reduce the deformation energy, which further suppresses recrystallization. For these two reasons, some areas between small austenite nuclei bands are always present inside the microstructure (Figure 5.21 (l)). Hence, the material cannot be fully recrystallized even after long soaking time. Since higher heating rate preserves most deformation energy inside the microstructure, the new recrystallized ferrite grains grow rapidly. Normal to the rolling direction, the growing ferrite will be pinned by austenite colonies. This leads to large, long ferrite grains between austenite colonies. Few austenite grains are found on the ferrite-ferrite grain boundaries in HR80.

HR18 behaves in a mixed way of HR4 and HR80. The recrystallized ferrite areas behave similar as HR4, with austenite nucleating on ferrite-ferrite grain boundaries, and growing normally into the bulk. The un-recrystallized areas behave similar as HR80, with austenite nucleate at pearlite colonies and at interfaces inside deformed ferrite (red arrow in Figure 5.21 (g)). Similar to HR80, ferrite remains partially un-recrystallized even after long soaking time (Figure 5.21 (h)).

Another way to observe the austenite formation is by capturing the Ms at different stages. The corresponding Ms are plotted in Figure 5.23. As shown, Ms scattered a lot at the beginning stage, (<1min) due to the low accuracy of the test. For different heating rates in general, Ms increases as holding time increases. Roughly two stages of transformation can be distinguished from the curves:

- I. Growth of small austenite nuclei, carbon concentration decreases, Ms increases (fast).
- II. austenite formation almost completed, grain size effect takes place. Austenite grain size increases, Ms increases (slow).

Take HR4 for an example, from Figure 5.21 we can see that austenite nucleation and growth takes time. After nucleation, austenite grows normally into the ferrite bulk, and this process lasts until at least 60 s. This can be indicated by stage I, during which time the microstructure has not reached the equilibrium austenite fraction, and increment of austenite amount and size is happening. At this stage, there may be variations of austenite grain size with different heating rates, but the main factor that is influencing Ms is carbon content. Austenite preferably nucleate at sizes with a rich carbon source, resulting in a nucleus with higher carbon content. The austenite grains that nucleated at a lower temperature are with an even higher carbon content, according to the phase diagram. Thus, when these small nuclei with high carbon content grow, the local carbon content inside austenite will decrease, causing and increment in Ms at stage I. When austenite fraction gradually reaches equilibrium, the amount of austenite does not change very much with time. This means,

the average carbon content in austenite becomes stable as well. Take again HR4 for example, judged by the microstructure (Figure 5.22 (a) and (b)), the morphology of HR4 with holding time 3 min and 10 min does not differ a lot. During this time, the austenite grains still increase in size, while the carbon content stays the same. This will cause a gradual increase in Ms, as indicated by stage II. From Figure 5.23 we can see this increment of Ms caused by grain size is rather small. From holding time 3 min to 10 min, Ms only increases around 20°C, thus it is reasonable to neglect this effect at stage I. There is no sharp distinction between those two stages in the figure, due to the fluctuation caused by different heating rates.

In subsection 3.2.4 the error of martensite transformation temperature for directly quenched samples is discussed. The error of ±6 °Cis relevant at the start of each curve in Figure 5.23. This Ms for directly quenched samples can fluctuate over a large range due to the randomness of the sample at this stage, and is of small importance to the whole trend for the increasing holding time. Hence, the error of Ms determination for directly quenched samples does not have a big influence on analysing the austenitization phenomenon.

Notice for the lower heating rates (HR4, HR10), there seems to be a minimum at around holding time 3 min, indicated by the red arrow in Figure 5.23. In the repeated HR4 series in June, this minimum still exists, despite of the inaccuracy of the Ms test. As discussed above, at stage I, neglecting grain size effect, Ms decreases as carbon content increases. Carbon content is controlled by carbon diffusion, i.e. dissolving of carbon from cementite into austenite. When austenite grows into ferrite after nucleation, local carbon content will decrease. However, as soaking time increases, the total amount of carbon dissolved into austenite increases in the whole structure. If the growth of austenite is slower than the dissolving of carbon, an increasing in carbon content is possible. These are two counteracting effects. Besides the inaccuracy of the Ms measurements, this could also be the reason for the ups and downs in the beginning stage of the transformation.

A possible hypothesis for the minimum as a function of low heating rates is, due to the different austenite formation mechanism in low heating rates, after certain holding time, the dissolving of carbon exceeds the growth of austenite fraction, resulting in an abnormal temporary increasing in carbon content. From Appendix D we can see HR10 behaves similar as HR4. Both HR4 and HR10 is fully or nearly fully recrystallized before phase transformation, and that austenite nucleate mostly at ferrite-ferrite grain boundaries. At the beginning, the small austenite nuclei with relatively high carbon content grow rapidly. Although austenite growth and carbon dissolving happen at the same time, the total effect is a decrement of local carbon content. This is same for all heating conditions. As holding time goes to around 1 min, the ideal nucleation sites for HR4 are saturated, and the growth of austenite fraction has to be realized by normal growth into ferrite. This hypothesis can be side-proved by observing the microstructure of HR4 with holding time in Figure 5.21 (c). Indeed, at this time, the ferrite-ferrite grain boundaries are almost fully covered by austenite nuclei. This normal growth is relatively slow, while carbon continuously dissolves into austenite. At a certain point, the dissolving of carbon exceeds the increasing of austenite fraction, and carbon content slightly increases. From Figure 5.23, this increasing of carbon content (i.e. decreasing of Ms) starts after soaking for around 30 sto 1 min. The biggest difference of Ms of this minimum is around 20°C. And the relevant difference of carbon content can be estimated using the same equation (the element symbols in the equations represents the composition of the corresponding element in wt %):

$$
\begin{aligned}
Ms &= 539 - 423C - 30.4Mn - 17.7Ni - 12.1Cr - 11.0Si - 7.0Mo \text{[2]} \\
&= 539 - 423C - 30.4Mn - 11.0Si \\
&= 472 - 423C \\
\Delta Ms &= 423\ \Delta C \\
\Delta C &= \frac{20°C}{423°C/wt\%} / = 0.05\,wt\%
\end{aligned}
$$

Notice that whether Ms with holding time 3 min is the lowest or not cannot be proved. The lowest point could either be earlier than 3 min or later, and further experiments are needed. At least, this 20°C difference is the minimum captured by these Ms measurements. At around 3 min, austenite growth and carbon dissolving are almost completed, and carbon content becomes stable. The influence of austenite grain size starts to take place, and Ms slowing rises. For higher heating rates, nucleation of austenite starts from a different microstructure. The same competition between increasing of austenite fraction and carbon dissolving still

exists, only that the nucleation sites are not restricted to ferrite-ferrite grain boundaries. Take HR18 for example, austenite can nucleate at pearlite colonies, at un-recrystallized ferrite cell walls, and at recrystallized ferrite-ferrite grain boundaries. The austenite fraction can always increase by forming new grains. There may be ups and downs, but those two processes are always in a similar pace, which explains why this minimum only appears in HR4 and HR10.

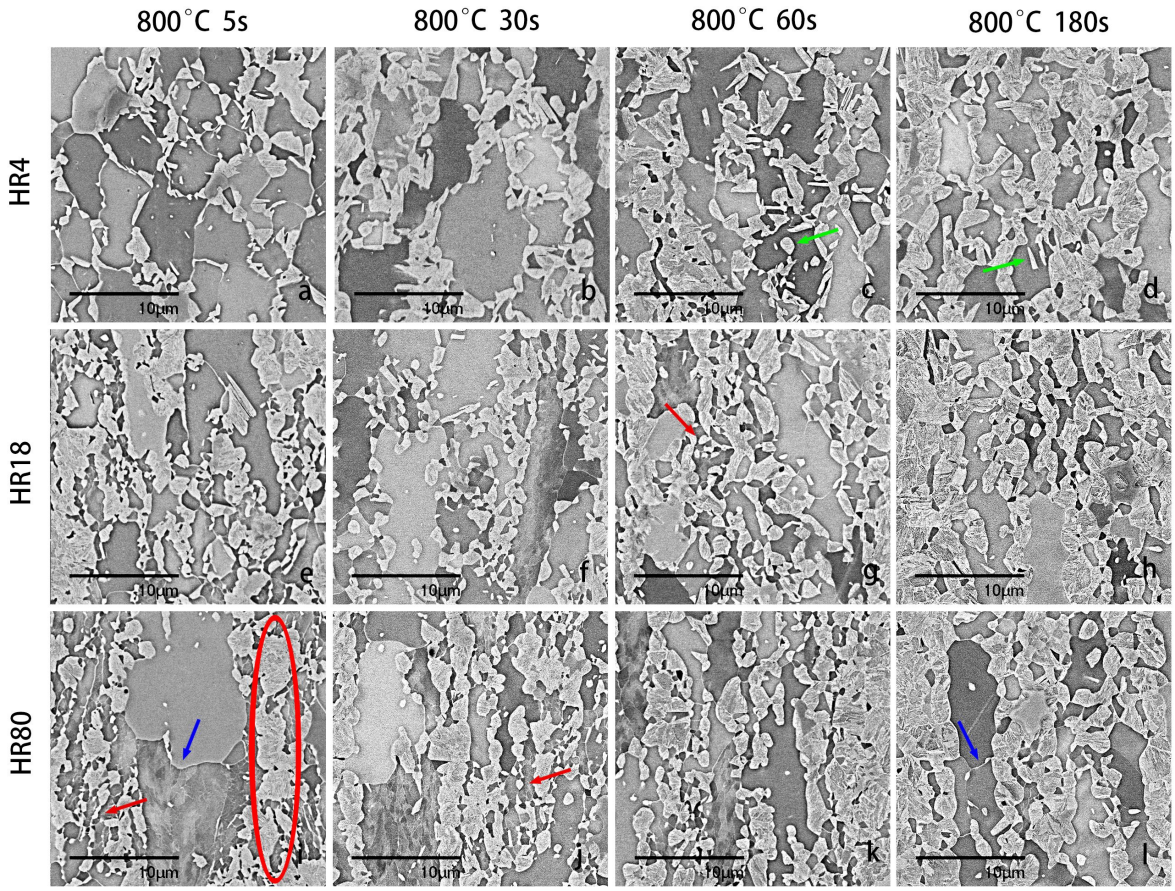


Figure 5.21: SEM result of different heating rates, (a) HR4/800/5sQ, (b) HR4/800/30sQ, (c) HR4/800/1minQ, (d) HR4/800/3minQ, (e) HR18/800/5sQ, (f) HR18/800/30sQ, (g) HR18/800/1minQ, (h) HR18/800/3minQ, (i) HR80/800/5sQ, (j) HR80/800/30sQ, (k) HR80/800/1minQ, (l) HR80/800/3minQ. *BEI*, ×2000, *rolling direction is vertical.*

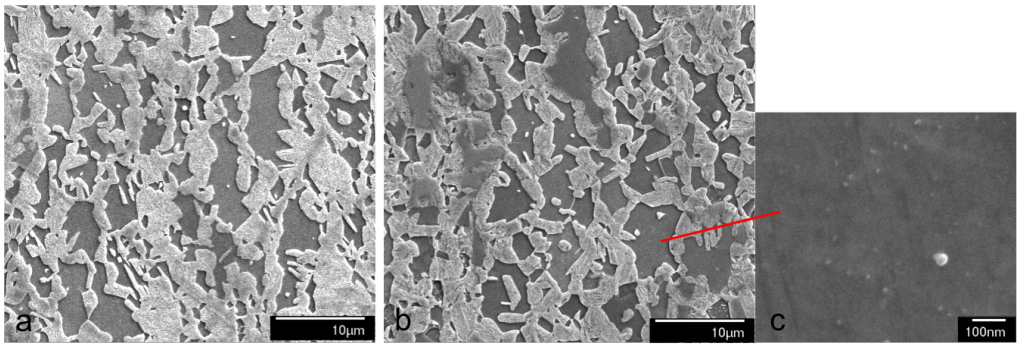


Figure 5.22: SEM result of different heating rates, (a) HR4/800/3minQ, (b) HR4/800/10minQ, ×2000, (c) HR4/800/10minQ, ×50,000, *SEI, rolling direction is vertical.*

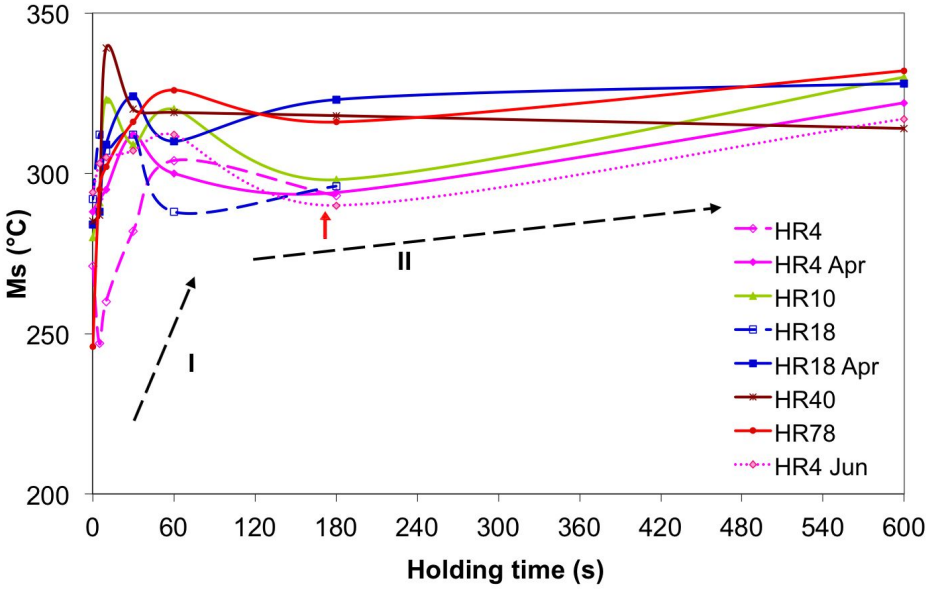


Figure 5.23: Influence of heating rate and holding time on Ms.

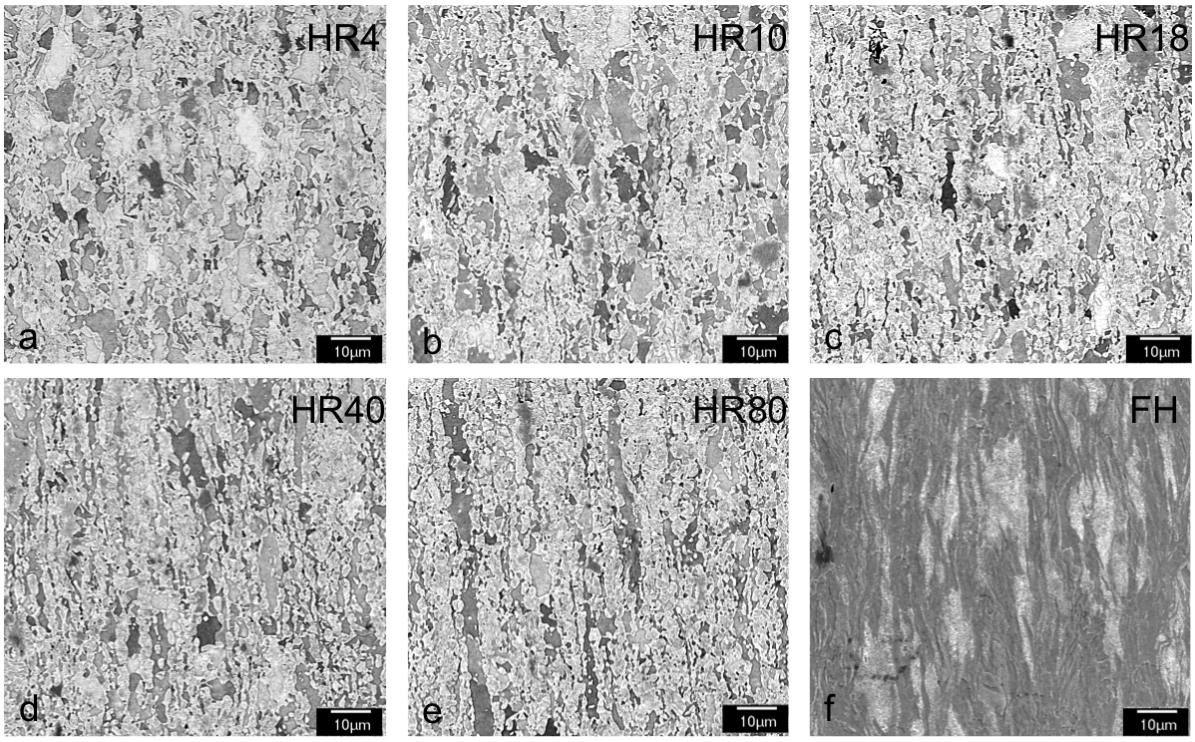


Figure 5.24: SEM result of different heating rates, (a) HR4/800/3minQ, (b) HR10/800/3minQ, (c) HR18/800/3minQ, (d) HR40/800/3minQ, (e) HR80/800/3minQ, (f) Full hard.
$(a)-(e)$ $BEI$, ×2000; $(f)SEI$, ×2000, *rolling direction is vertical.*

Another observation is that, by increasing the heating rate, the banding structure also increases, if we look at the microstructures at a lager scale. Figure 5.24 presents the microstructure of all heating rates after soaking for 3 min. As heating rate increases from HR4 to HR80, the banding structure becomes more and more serious. By changing heating rate, different initial microstructure can be modified before austenite formation in two ways: recrystallization process, which can reduce the banding structure by forming uni-axial ferrite;

the degeneration of pearlite, which redistributes carbon, forcing carbon to leave the original pearlite bands. As it appears in Figure 5.24, HR4 consists of recrystallized uni-axial ferrite grains surrounded by austenite colonies, while HR80 consists of long bid recrystallized ferrite grains between austenite bands.

When soaking over 3 min, the austenite formation is almost completed, comparing micrograph (a) and (b) in Figure 5.22. Coarsening of precipitates can be observed as soaking time goes to 10 min. Those precipitates are so small that they cannot be observed in the samples with shorter holding time. Whereas, in Figure 5.22 (c) the precipitates are very obvious, randomly scattered inside ferrite grains. The estimated diameter of the precipitates is around 20 nm.

### Summary

Comparing to the three-stage theory of austenite formation mechanism discussed in subsection 2.1.4, the austenite formation of this material under different heating rates can be concluded as follows:

From different initial microstructure, transformation of austenite is different:

- From fully recrystallized ferrite structure:
  - (i) Austenite nucleates at ferrite-ferrite grain boundaries until site-saturation.
  - (ii) Slow growth of austenite, normally into ferrite. Carbon trapped inside ferrite bulk can also nucleate as soaking time increases, by forming coherent interfaces between austenite and ferrite.
  - (iii) Slow approach to equilibrium, growth of precipitates and increasing of austenite grain size.
- From un-recrystallized ferrite structure:
  - (i) Austenite nucleates at pearlite colonies and at interfaces, including recrystallized ferrite-ferrite grain boundaries and cell walls of un-recrystallized ferrite grains.
  - (ii) Various nucleation sites of austenite can be activated over a longer time period, followed by a slow growth of these nuclei. Austenite nuclei block the moving grain boundaries of recrystallized ferrite. Austenite at nucleated at cell walls can reduce the deformation energy inside the cold-rolled structure, suppressing further recrystallization.
  - (iii) Slow approach to equilibrium, growth of precipitates and increasing of austenite grain size.

Recrystallization temperature increases as heating rate increases. For the lowest heating rate HR4, recrystallization starts at 680 °C, and recrystallization fraction is fully completed before austenite formation. For intermediate heating rate HR18, recrystallization starts at 720 °C, recrystallization fraction is around 50% prior to austenite formation. For highest heating rate HR80, recrystallization starts at 740 °C, recrystallization fraction is below 10% before austenite formation. By modifying the heating rate, the extend to which recrystallization and austenitization interact can be modified.

Upon heating, lamellar pearlite degradation takes place together with recrystallization. The recrystallization process coincides with the degradation of pearlite. By applying lower heating rate, the degradation becomes stronger.

# 6

# Simulation results and discussion

## 6.1. Simulation with CA-model below $Ac_1$

From the previous chapter it is clear that there are two possibilities for austenite nucleation: at pearlite colonies and at ferrite-ferrite grain boundaries. However, in the present CA-model, austenite can only nucleate from prior pearlite colonies, and grow normally into ferrite afterwards. This limitation disables simulating austenite transformation above $Ac_1$ for the complications in this study. However, it can still be applied to simulate the ferrite recrystallization below $Ac_1$. Input parameters are listed in Table 4.1, and five heating rates (HR4, HR10, HR18, HR40, and HR80) were simulated to see the influence on ferrite recrystallization. The simulated micrographs together with the input initial microstructure are shown in Figure 6.1. Light blue areas indicate recrystallized ferrite, dark blue areas indicate un-recrystallized ferrite, and grey areas indicate pearlite.

It is clear that by increasing heating rate, recrystallization of ferrite is retarded due to the limited soaking time associated with fast heating rates. By comparing with the experimental results (Figure 6.2), the simulation results show a similar trend. Although the degradation of pearlite is not simulated in this model, the distribution of recrystallized ferrite, as well as the recrystallized ferrite size are well reproduced. By modifying heating rates, the extent to which ferrite recrystallization and austenite transformation can be modified. It is beyond the capability of the current CA-model to further simulate the austenite formation from this complicated microstructure with different austenite nucleation mechanisms. Thus, phase-field model was introduced to give an insight of austenite transformation.

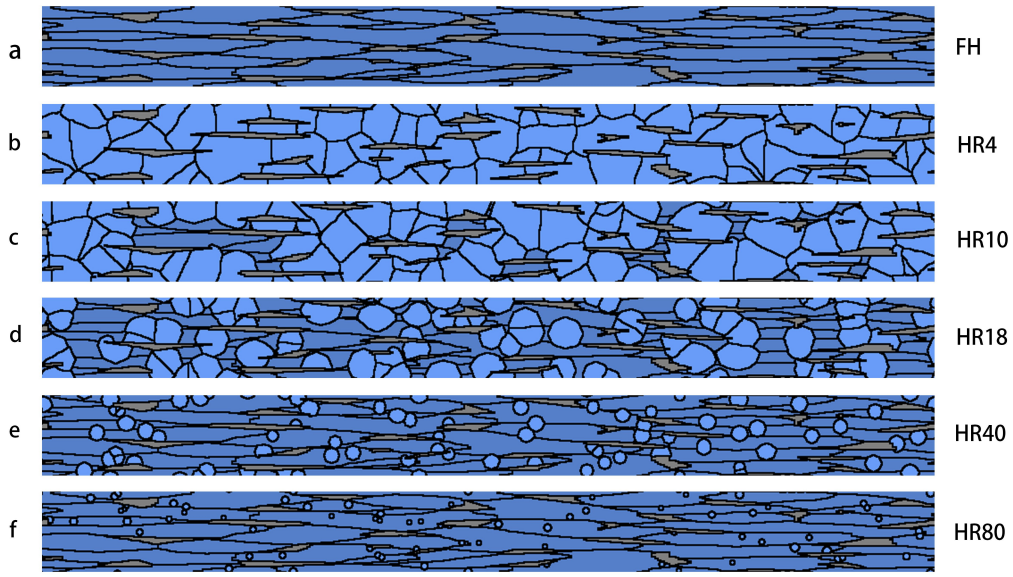


Figure 6.1: Simulated micrographs with CA model, top temperature 750°C with heating rate (b) HR4, (c) HR10, (d) HR18, (e) HR40, (f) HR80, together with initial microstructure (full hard) (a) after 30 % reduction. Light blue areas indicate recrystallized ferrite, dark blue areas indicate un-recrystallized ferrite, and grey areas indicate pearlite.

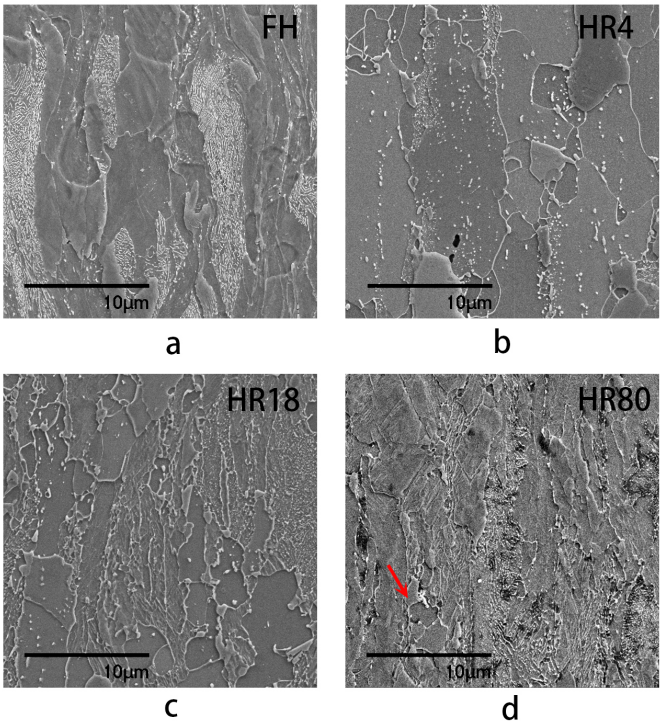


Figure 6.2: SEM results from top temperature 740°C of (a) full hard and heating rates (b) HR4, (c) HR18 and (d) HR80. SEI, ×2000. Rolling direction is vertical.

## 6.2. Simulation with phase field model above $Ac_1$

Compared to the CA-model, the phase-field model has more possibilities dealing with complicated initial microstructures and different nucleation sites. However, the computational cost in 3D is enormous and efficiency has to be taken into account. Due to the limitation of time, only the simplest situation HR4 is studied with phase-field model, hence, the simulation starts from a fully recrystallized microstructure, and austenite can nucleate both at $\alpha/\alpha\theta$ interfaces, and at $\alpha/\alpha$ grain boundaries. The cementite is to imitate the spheriodized cementite in the SEM observation (Figure 6.2b). In the reality, the size of ferrite is about 20$\mu$m, while the small cementite spheres are about 20 nm in diameter. If the true size of cementite spheres are to be simulated, the grid size has to be to the order of 10 nm. With the same grid size, the number of grid points necessary to describe a microstructural domain with at least two or three ferrite grains will be too large. Thus, the dimensions of both ferrite grains and cementite spheres are modified for the convenience and efficiency of calculation, and thus the results can only qualitatively reveal the austenitization process.

The simulated austenite formation is shown in Figure 6.4 (left), together with the corresponding carbon concentration profile (right). It is clear that both nucleation on ferrite grain boundaries and from cementite colonies are possible, and austenite from both sites can further grow. An interesting discover is that, the cementite colonies can also act as carbon source, without necessity of direct transforming into austenite. Several cementite colonies inside the ferrite bulk reduced in size while austenite grains which do not have direct contact are growing (arrows in Figure 6.4c, left). Thus nucleation of austenite on $\alpha\alpha$ grain boundaries does not have to be in contact with cementite. Judged by the change of austenite nucleated from both sites from Figure 6.4 (b) to (c), nucleation and growth for both sites happen at a similar time, and with a similar speed. There is no severe distinction between those two kinds of austenite once they grow, having only a slightly difference in size.

The evolution of phase fraction versus time is shown in Figure 6.3. The austenite transformation shows a two-step behavior. At the start of the fraction curve, the fraction of cementite drops rapidly, this is because in the initial microstructure, additional cementite was added to imitate the carbides in the bulk, and that the start fraction of cementite is higher than equilibrium. At around 8 s, both ferrite fraction and cementite fraction start to reduce, this indicate the start of austenite formation. At the first stage of transformation, the dissolving of cementite is very fast, coupling with a fast consummation of ferrite. Relating to the observation in microstructure evolution (Figure 6.4), this dissolving of cementite provides carbon to austenite grains both on cementite sites and and $\alpha/\alpha$ grain boundary sites. And this process involves the diffusion of carbon through ferrite lattice and along ferrite grain boundaries.

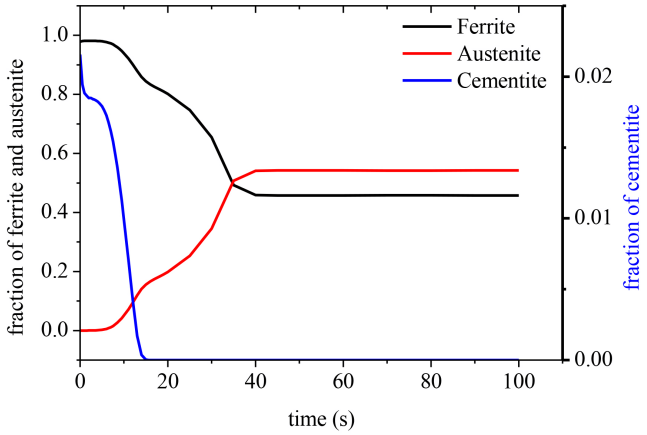


Figure 6.3: Simulated transformation phase fractions versus time.

Carbon concentration evolution versus time is taken at the cross-section shown in Figure 6.4 (c), both from austenite nucleated at $\alpha/\theta$ interface (along B-B in Figure 6.4 (c)) and at $\alpha/\alpha$ grain boundaries (along A-A in

Figure 6.4 (c)). Figure 6.5 shows that originally the cementite is with a carbon content around 7 wt%. When temperature exceeds $Ac_1$, austenite nucleated on one side of the cementite, and slowly consumes the cementite. The austenite slowly grows into ferrite with a carbon content of around 1 wt% , until a full dissolution of the cementite. The final carbon concentration in austenite is around 0.2 in wt %. A different behavior is observed in the austenite formed on $\alpha/\alpha$ grain boundaries (Figure 6.6). At first the carbon concentration is very low in the ferrite areas. When temperature exceeds $Ac_1$, nucleation of austenite happen on the grain boundary, by the appearance of a sudden increase of carbon content in the carbon profile. A decrease of carbon content in the vicinity of this nuclei can hardly be seen, due to the very low concentration in the nearby ferrite grains, which almost rule out the possibility that the carbon source is the over-saturated carbon from pro-eutechtoid ferrite. Thus it is reasonable to deduce that the carbon needed for this nuclei defused through the ferrite lattice. The carbon concentration of the nuclei after nucleation is around 1 wt %, and slowly decreases as the austenite grows. The final carbon concentration is similar to the austenite nucleated near cementite, with a value around 0.2 wt %, which once again confirms that there is no severe distinction of austenite between two nucleation sites.

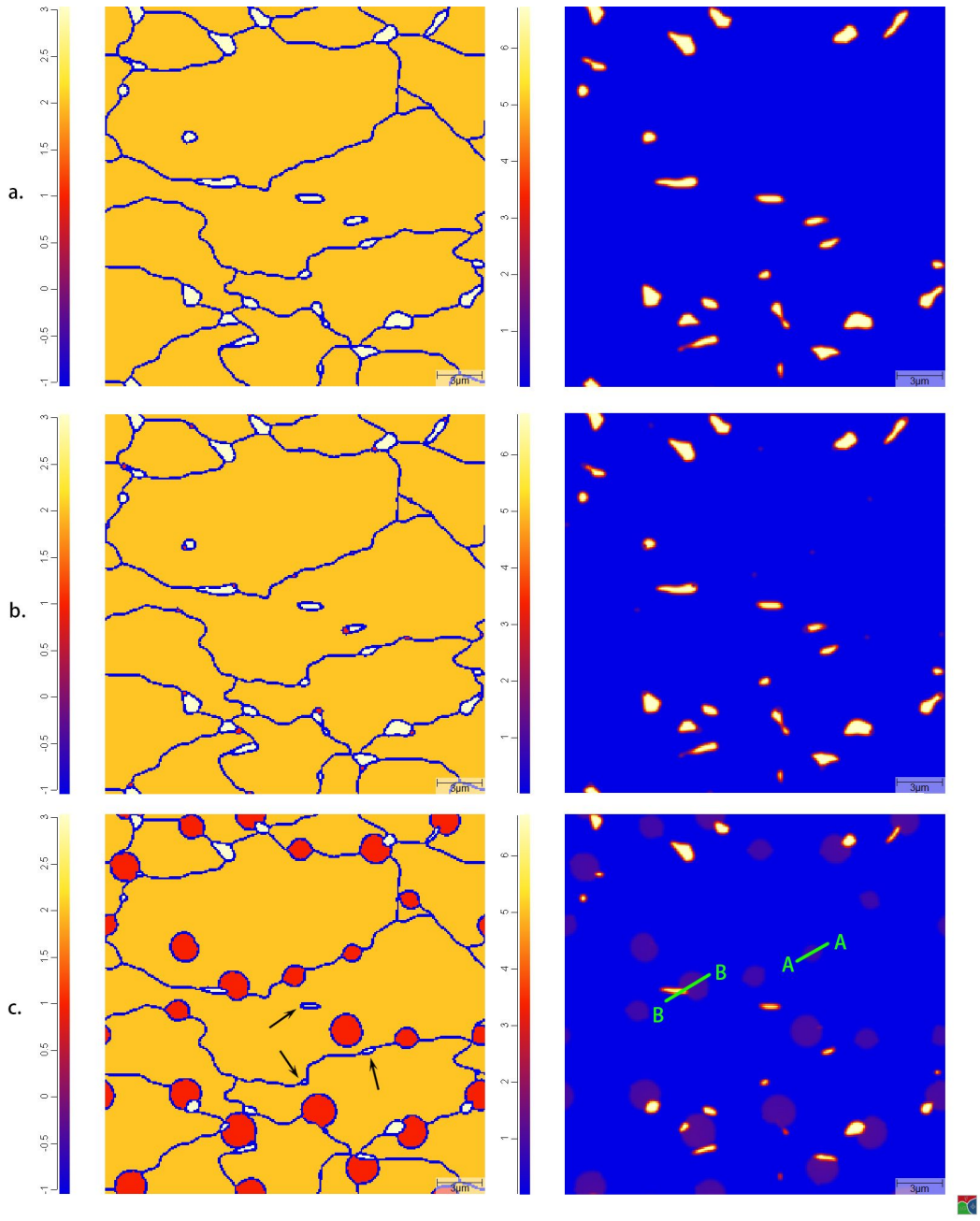


Figure 6.4: Simulated micrographs (left) and carbon concentration profiles (right) with phase-field model: (a) start microstructure, (b) 10 s, (c) 15 s.

Relating to the real microstructure of the material studied in this thesis, this result shows several indications. Since in the actual microstruture, cementite spheres with much smaller dimensions are scattered around the ferrite grains, instead of cementite colonies used in this simulation. Thus, this carbon source is more approachable and efficient compared to the simulated situation, making nucleation of austenite on ferrite grain boundaries possible. It is clear from the simulation that the nucleation of austenite does not have to have a direct contact to the cementite, and even so there is no significant differences between the austenite grains from different nucleation sites.

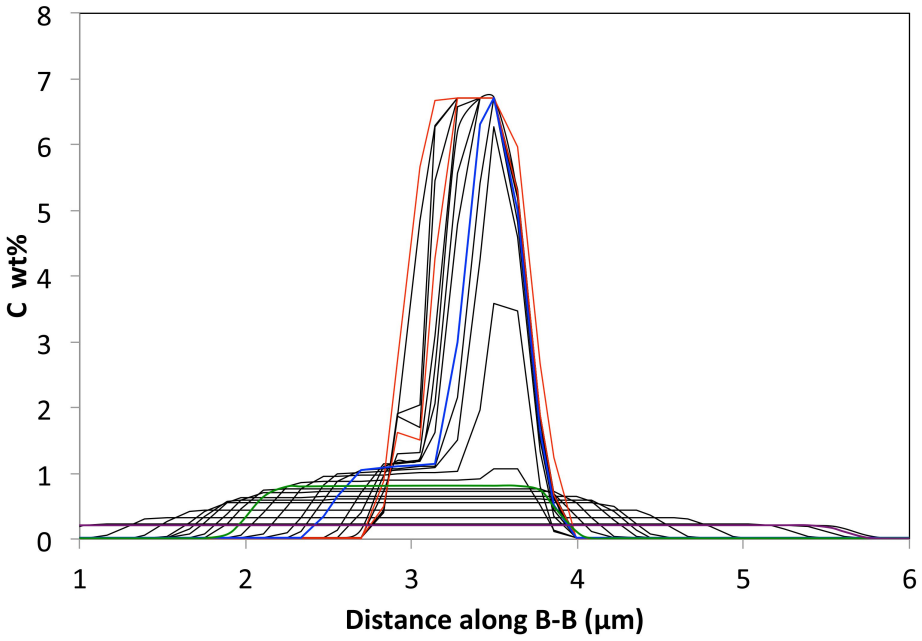


Figure 6.5: Carbon distribution along the line B-B in Figure 6.4 (c).

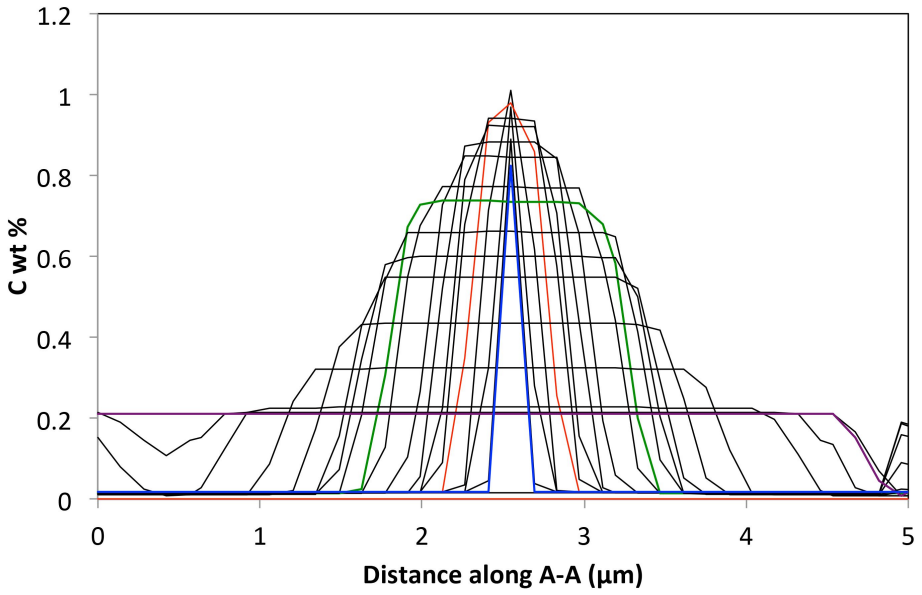


Figure 6.6: Carbon distribution along the line A-A in Figure 6.4 (c).

# 7

# Conclusions

This report mainly studied the microstructural evolution of a DP steel during continuous annealing process. Upon heating, recovery and recrystallization happened first, and when temperature exceeded $Ac_1$, austenite formation happens, and these two processes may interact with each other. Literature revealed that for a typical ferrite-pearlite start microstructure, austenitization process has three stages, and there are two possible nucleation sites of austenite: pearlite colonies and ferrite-ferrite grain boundaries.

Different heating rates were applied to the material, and techniques as dilatometry and SEM were used to investigate the influence on microstructure. Heating rate of cold-rolled DP steel can affect the austenitization process mainly by affecting the starting microstructure before $Ac_1$, hence recrystallization fraction and carbon distribution. The former factor also affects the latter. Spheriodization of cementite and recrystallization of ferrite is seem to happen at the same time. The higher the heating rate is, the higher recrystallization temperature will be.

With heating rate of 4.4 °C/s, recrystallization started at around 680°C, and finished before austenite formation happens. Austenite formed mostly around ferrite-ferrite grain boundaries. As soaking time increases, the carbon trapped inside ferrite bulk can also induce austenite nucleation.

With heating rate of 18.6 °C/s, recrystallization started around 720°C, and is half-way to fully recrystallized structure before $Ac_1$. Austenite formed both at the original pearlite colonies, and at various interfaces inside the microstructure .

With heating rate of 80 °C/s, both recrystallization and austenitization happened at a relatively high temperature. Only a small amount of ferrite had recrystallized before $Ac_1$. Austenite mainly nucleated at prior pearlite colonies, as well as at interfaces such as cell walls inside un-recrystallized ferrite and grain boundaries of recrystallized ferrite grains.

The higher the carbon content in austenite, the lower the Ms transformation temperature is. By affecting the carbon content in austenite, heating rate has a strong influence on Martensite transformation temperature in a complicated manner. Carbon content in austenite fluctuates during different transformation periods, which can influence the Ms captured by dilatometer. Austenite grain size can also influence Ms, but in a similar manner for different heating rates in a longer time period. As austenite grain size increases, Ms slowly increases.

In the current CA-model, increasing the heating rate reveals a similar effect as the experimental results. As heating rate increases, the recrystallization fraction decreases when top temperature is reached, and the recrystallized ferrite grain size is smaller correspondingly.

It is hard to truly simulate the austenitization process from the complicated experimental microstructure. However, by a demonstrating trial, the phase-field model reveals the nucleation behavior of austenite on

ferrite-ferrite grain boundaries. The behavior of austenite in the simulation proved that nucleation of austenite on ferrite-ferrite grainboundaries does not have to be in direct contact with cementite, and that carbon is mainly supplied by diffusion.

# 8

# Recommendations

From the observations in this study, a slower heating rate, varying from 4 °C/s to around 10 °C/s assures a fully recrystallized structure before austenite formation. This allows the reducing of banding structure and results in a more homogeneous microstructure after soaking. Further increasing of the heating rate could cause an interaction of ferrite recrystallization and austenitization. Whether this interaction is positive or negative to the properties of the final product, and how big is this influence, is still unknown.

A quantitatively measurement of recrystallization fraction prior to austenite formation can be carried out. The measurement of recrystallized ferrite can be carried out by EBSD. And a quantitative measurement of austenite fraction at different soaking time could also give a better insight on the influence of heating rate. One alternative to measure the austenite fraction is by optical microscopy, although the accuracy is not ideal. In order to get a more accurate austenite fraction at high temperature, the ammount of retained austenite after quenching also needs to be considered. This could be carried out by XRD experiments.

Further analysis of the dilatometer data is also useful. By adapting the dilatometer curve to the Koistinen-Marburger equation, information as martensite fraction as a function of temperature, and the amount of retained austenite at the end of quenching can be obtained. This could provide a better analysing of the martensite transformation temperature.

A lot of simulation possibilities can be done for this study, especially with the powerful tool of phase-field model. The initial microstructure could be modified more carefully, with a better fit to the experimental results. Conditions in the model can also be modified to have a better fit. However, it requires great effort and study to truly simulate the complicated microstructures in this study.

The effects of the vanadium precipitates have not been studied in this thesis. By introducing precipitates into the material, the interface mobility has decreased significantly. What is the influence of this retarding of mobility on the mechanisms of recrystallization and phase transformation, and how big is this influence is yet still unknown and worth study.

In the commercial DP steel, products with both heating rate 18 °C/s and 4 °C/s have shown a perfect dual phase microstructure, consist of ferrite grains surrounding by martensite colonies. This thesis only studied the first two stages of the continuous annealing process, what is the effect of the latter stages and how they further adjust the microstructure is also interesting.

# List of Figures

# List of Tables

# A

# Sample code

(All samples prepared at TUDelft.)

Table A.1: Sample code I

| | Heating rate (°C/s) | Top temperature (°C) | Holding time (s) | Sample code |
|---|---|---|---|---|
| HR2 | 2 | 800 | 0 | HR2/800Q |
| HR4 | 4.4 | 650 | 0 | HR4/650Q |
| | | 680 | 0 | HR4/680Q |
| | | 720 | 0 | HR4/720Q |
| | | 740 | 0 | HR4/740Q |
| | | 800 | 0 | HR4/800Q/Mar |
| | | | | HR4/800Q/Apr1 |
| | | | | HR4/800Q/Apr2 |
| | | 800 | 5 | HR4/800/5sQ/Mar |
| | | | | HR4/800/5sQ/Apr1 |
| | | | | HR4/800/5sQ/Apr2 |
| | | 800 | 10 | HR4/800/10sQ/Mar |
| | | | | HR4/800/10sQ/Apr |
| | | 800 | 30 | HR4/800/30sQ/Mar |
| | | | | HR4/800/30sQ/Apr1 |
| | | | | HR4/800/30sQ/Apr2 |
| | | 800 | 60 | HR4/800/1minQ/Mar |
| | | | | HR4/800/1minQ/Apr1 |
| | | | | HR4/800/1minQ/Apr2 |
| | | 800 | 180 | HR4/800/3minQ/Mar |
| | | | | HR4/800/3minQ/Apr |
| | | 800 | 600 | HR4/800/10minQ |
| | | 1000 | 600 | HR4/1000/3minQ |

| | Heating rate (°C/s) | Top temperature (°C) | Holding time (s) | Sample code |
|---|---|---|---|---|
| HR10 | 10 | 800 | 0 | HR10/800Q |
| | | 800 | 5 | HR10/800/5sQ |
| | | 800 | 10 | HR10/800/10sQ |
| | | 800 | 30 | HR10/800/30sQ |
| | | 800 | 60 | HR10/800/1minQ |
| | | 800 | 180 | HR10/800/3minQ |
| | | 800 | 600 | HR10/800/10minQ |
| | | 1000 | 600 | HR10/1000/3minQ |
| HR18 | 18.6 | 650 | 0 | HR18/650Q |
| | | 680 | 0 | HR18/680Q |
| | | 720 | 0 | HR18/720Q |
| | | 740 | 0 | HR18/740Q |
| | | 800 | 0 | HR18/800Q/Mar |
| | | | | HR18/800Q/Apr1 |
| | | | | HR18/800Q/Apr2 |
| | | 800 | 5 | HR18/800/5sQ/Mar |
| | | | | HR18/800/5sQ/Apr |
| | | 800 | 10 | HR18/800/10sQ/Mar |
| | | | | HR18/800/10sQ/Apr |
| | | 800 | 30 | HR18/800/30sQ/Mar |
| | | | | HR18/800/30sQ/Apr1 |
| | | | | HR18/800/30sQ/Apr2 |
| | | 800 | 60 | HR18/800/1minQ/Mar |
| | | | | HR18/800/1minQ/Apr1 |
| | | | | HR18/800/1minQ/Apr2 |
| | | 800 | 180 | HR18/800/3minQ/Mar |
| | | | | HR18/800/3minQ/Apr |
| | | 800 | 600 | HR18/800/10minQ |
| | | 1000 | 600 | HR18/1000/3minQ |
| HR40 | 40 | 800 | 0 | HR40/800Q |
| | | 800 | 5 | HR40/800/5sQ |
| | | 800 | 10 | HR40/800/10sQ |
| | | 800 | 30 | HR40/800/30sQ |
| | | 800 | 60 | HR40/800/1minQ |
| | | 800 | 180 | HR40/800/3minQ |
| | | 800 | 600 | HR40/800/10minQ |
| | | 1000 | 600 | HR40/1000/3minQ |
| H60 | 60 | 800 | 0 | HR60/800Q |
| HR80 | 78 | 650 | 0 | HR80/650Q |
| | | 680 | 0 | HR80/680Q |
| | | 720 | 0 | HR80/720Q |
| | | 740 | 0 | HR80/740Q |
| | | 800 | 0 | HR80/800Q |
| | | 800 | 5 | HR80/800/5sQ |
| | | 800 | 10 | HR80/800/10sQ |
| | | 800 | 30 | HR80/800/30sQ |
| | | 800 | 60 | HR80/800/1minQ |
| | | 800 | 180 | HR80/800/3minQ |
| | | 800 | 600 | HR80/800/10minQ |
| | | 1000 | 600 | HR80/1000/3minQ |
| Full Hard | - | - | - | FH |
| Full Cycle | - | - | - | FC |

Table A.2: Sample code II: Samples of different welding positions

| | Heating rate (°C/s) | Top temperature (°C) | Holding time (s) | Sample code |
|---|---|---|---|---|
| EB | 18.6 | 800 | 0 | EB/HR18/800Q/pA1 |
| | | | | EB/HR18/800Q/pA2 |
| | | | | EB/HR18/800Q/pB1 |
| | | | | EB/HR18/800Q/pB2 |
| | | | | EB/HR18/800Q/pC1 |
| | | | | EB/HR18/800Q/pC2 |
| | | | | EB/HR18/800Q/pD1 |
| | | | | EB/HR18/800Q/pD2 |
| | 18.6 | 800 | 60 | EB/HR18/800/60sQ/pA1 |
| | | | | EB/HR18/800/60sQ/pA2 |
| | | | | EB/HR18/800/60sQ/pB1 |
| | | | | EB/HR18/800/60sQ/pB2 |
| | | | | EB/HR18/800/60sQ/pC1 |
| | | | | EB/HR18/800/60sQ/pC2 |
| | | | | EB/HR18/800/60sQ/pD1 |
| | | | | EB/HR18/800/60sQ/pD2 |

# B

# Thermal cycles for dilatometer

## B.1. Heating to different temperatures before 800°C + Quench

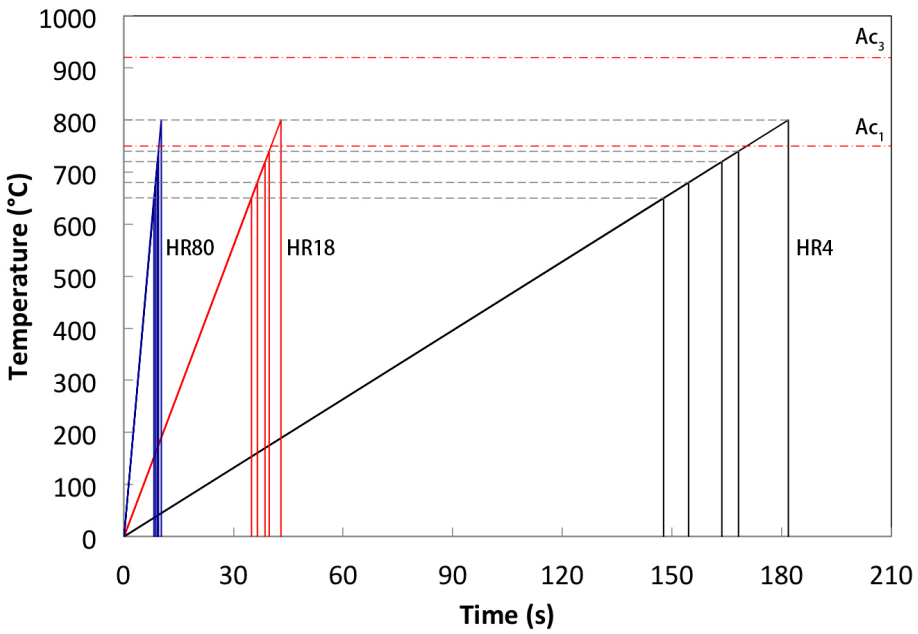


Figure B.1: Dilatometer cycle for heating before 800°C

## B.2. Heating to 800°C + Quench

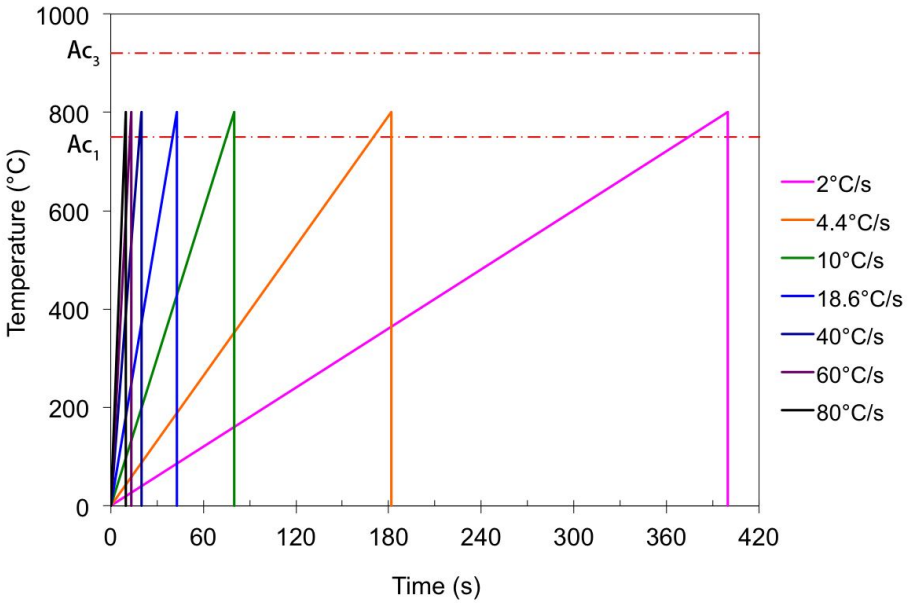


Figure B.2: Dilatometer cycle for heating to 800°C with different heating rates

## B.3. Heating to 800°C + Holding + Quench

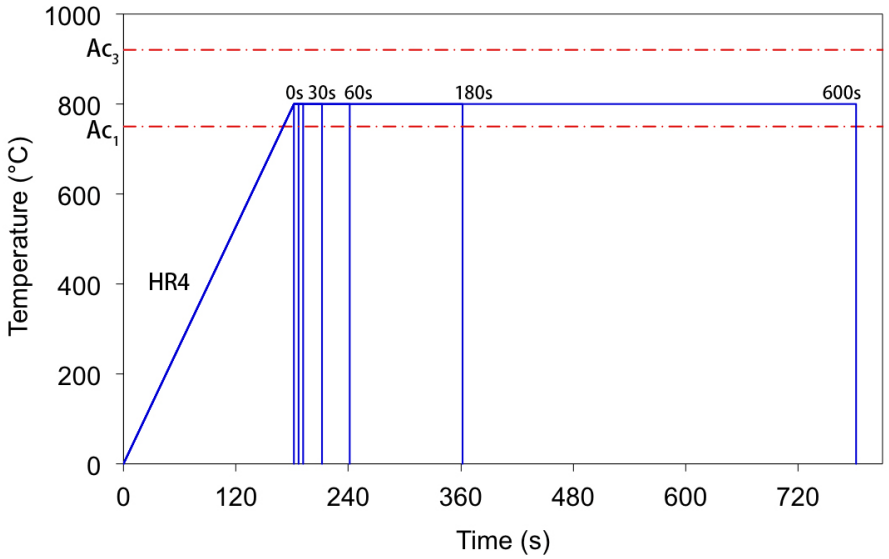


Figure B.3: Dilatometer cycle for heating to 800°C holding with increasing time and quench

## B.4. Heating to 1000°C + Holding 3 min + Quench

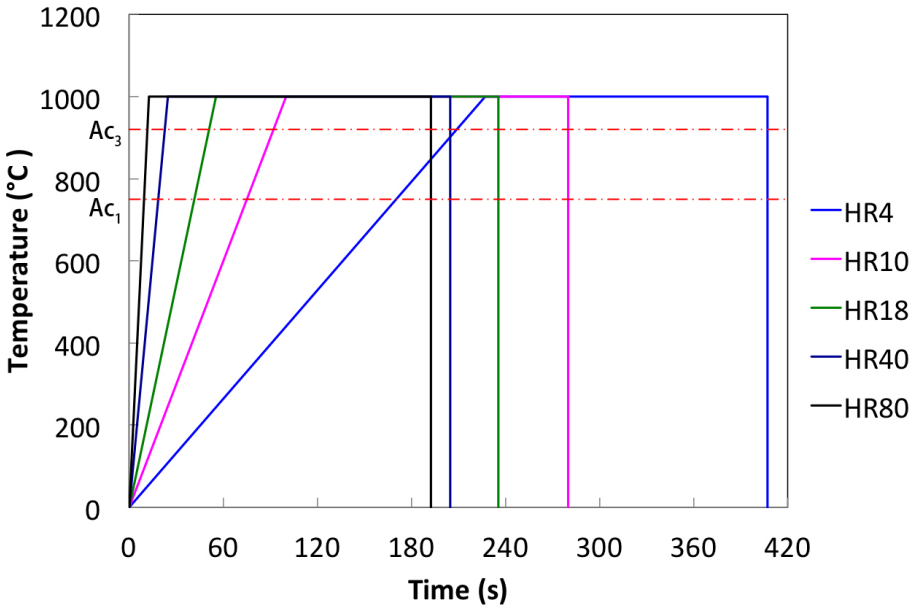


Figure B.4: Dilatometer cycle for full austenite treatment

# C

# Dilatometer curves

## C.1. Heating to 1000°C + Holding 3 min + Quench

### HR4

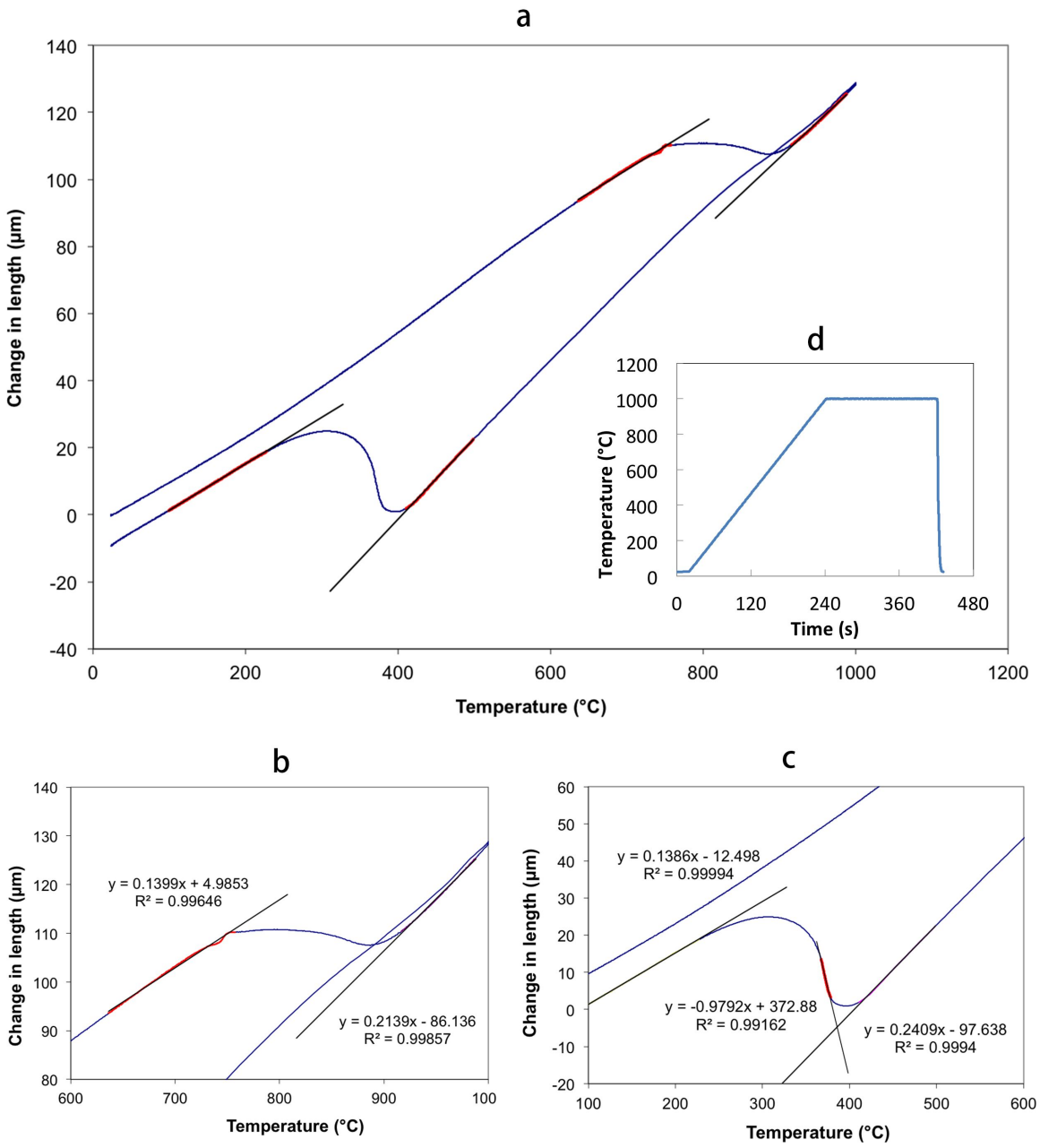


Figure C.1: Dilatometer curve of HR4, top temperature 1000°C, holding time 3min: (a) full curve, (b) austenite transformation, (c) martensite transformation, (d) heat treatment curve, time versus temperature.

## HR10

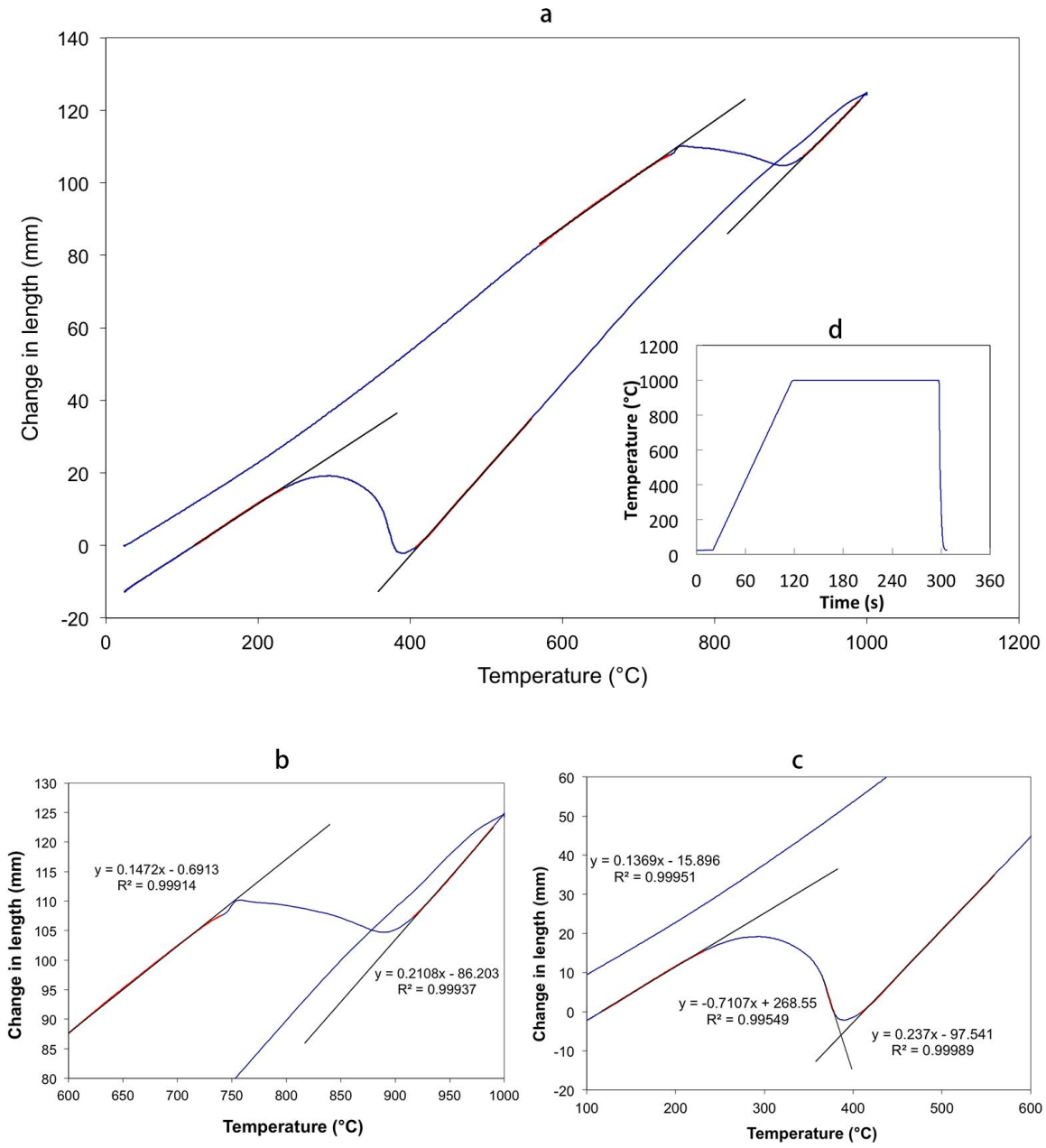


Figure C.2: Dilatometer curve of HR10, top temperature 1000°C, holding time 3min: (a) full curve, (b) austenite transformation, (c) martensite transformation, (d) heat treatment curve, time versus temperature.

## HR18

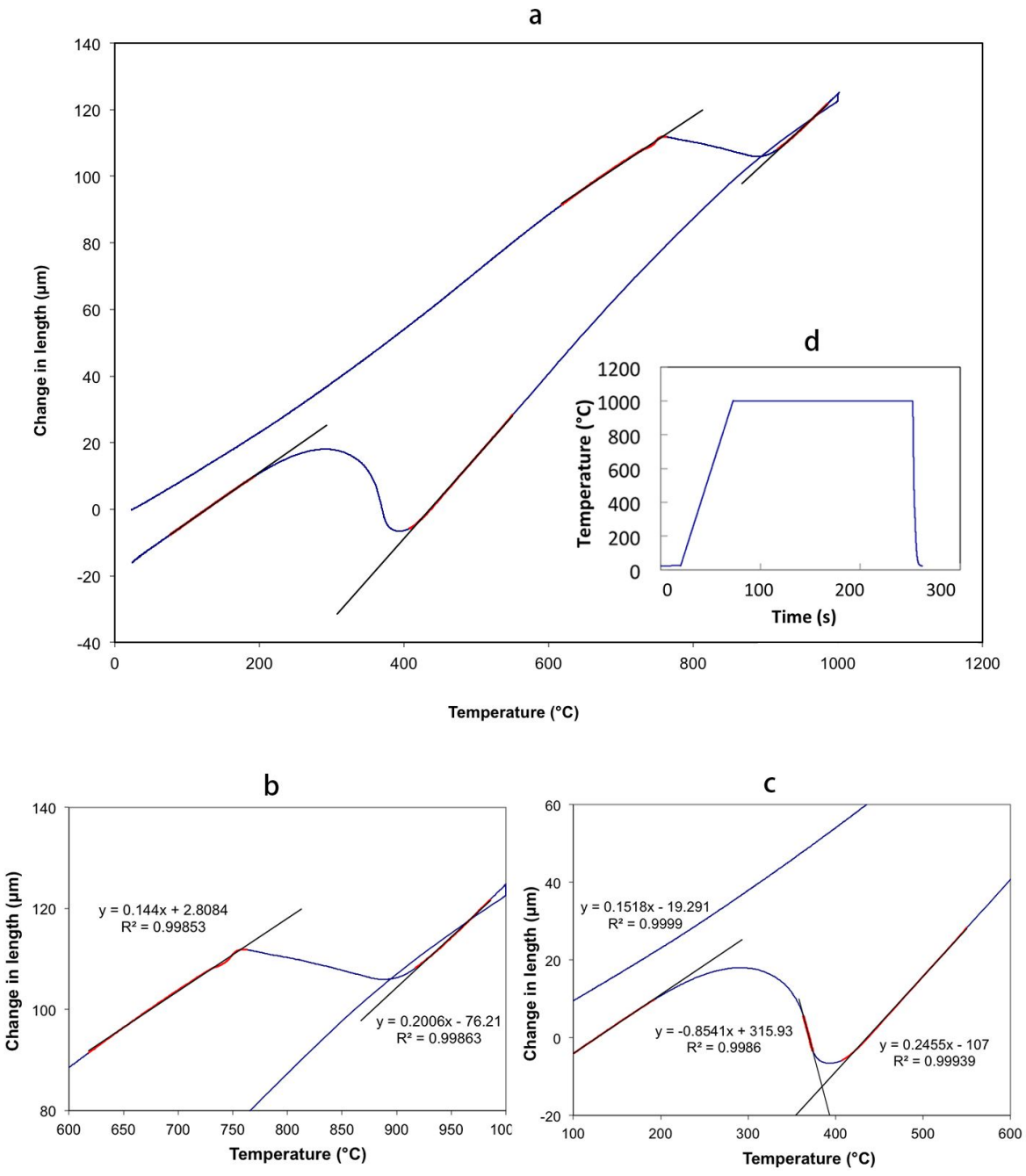


Figure C.3: Dilatometer curve of HR18, top temperature 1000°C, holding time 3min: (a) full curve, (b) austenite transformation, (c) martensite transformation, (d) heat treatment curve, time versus temperature.

## HR40

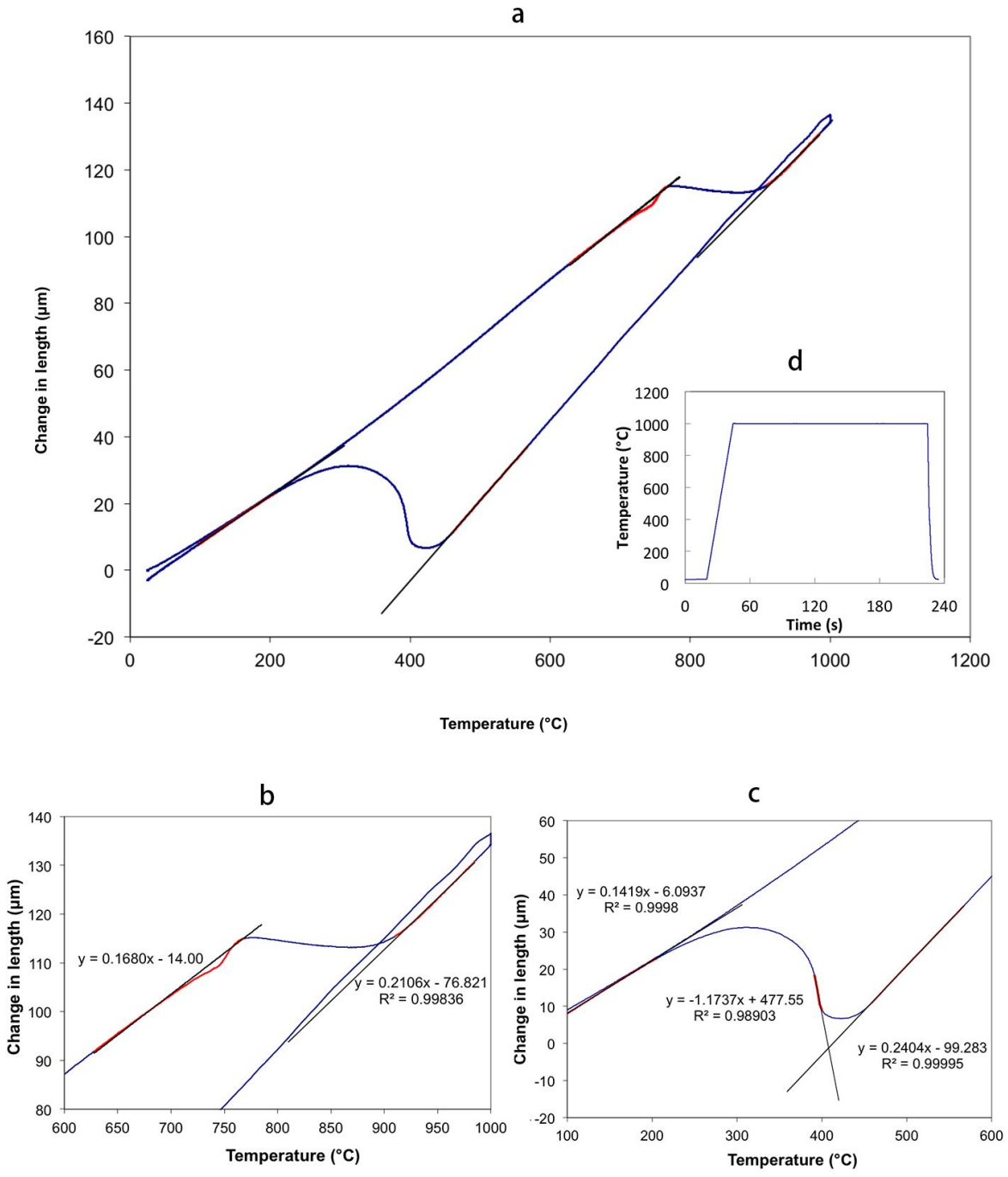


Figure C.4: Dilatometer curve of HR40, top temperature 1000°C, holding time 3min: (a) full curve, (b) austenite transformation, (c) martensite transformation, (d) heat treatment curve, time versus temperature.

## HR80

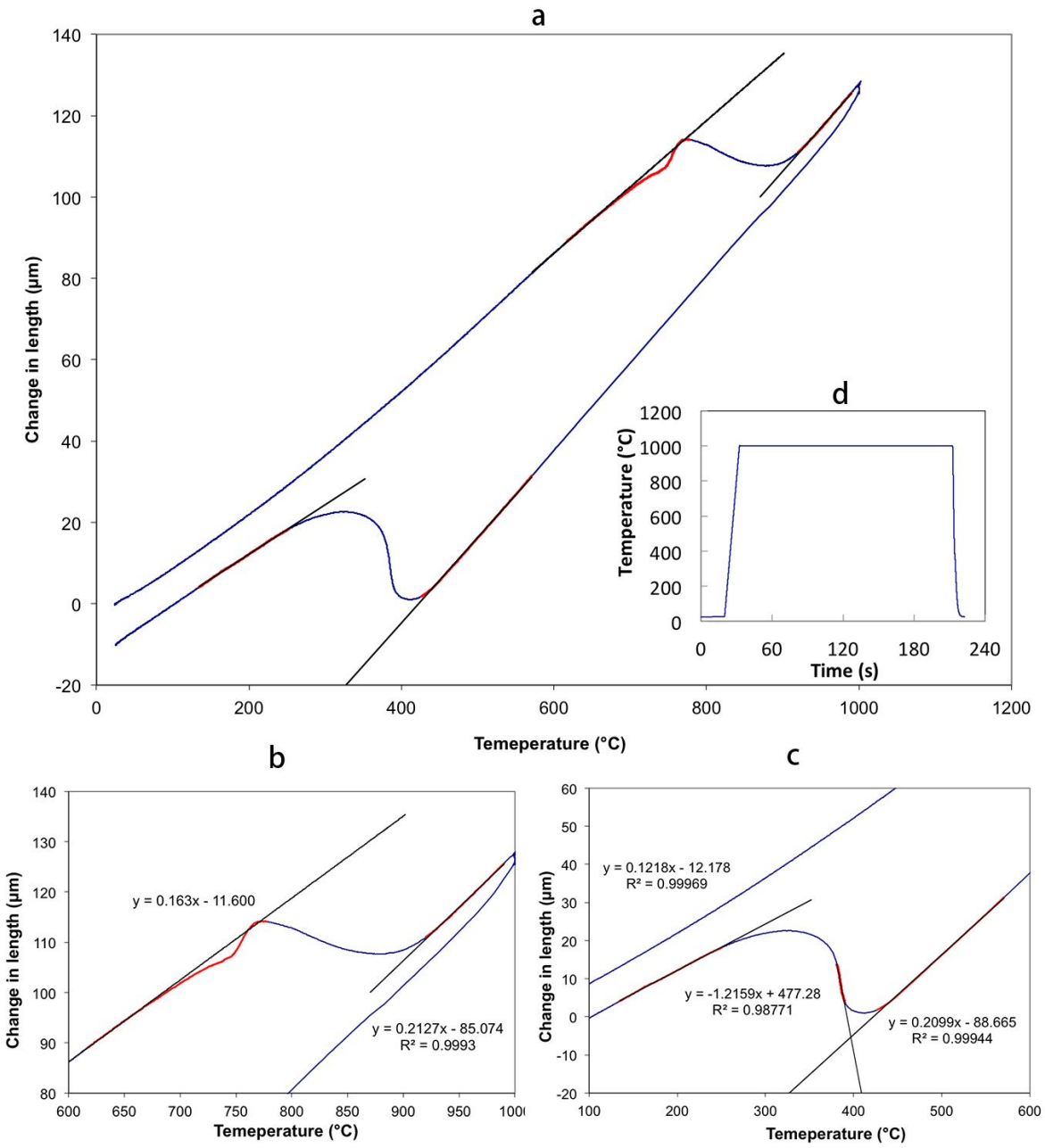


Figure C.5: Dilatometer curve of HR80, top temperature 1000°C, holding time 3min: (a) full curve, (b) austenite transformation, (c) martensite transformation, (d) heat treatment curve, time versus temperature.

## C.2. Heating to 800°C + Holding + Quench

There is a fluctuation of temperature control while the dilatometer shift from heating to cooling, as shown in Figure C.6, Figure C.7, Figure C.8 a, resulting in a fluctuation of dilatation. However, this fluctuation only lasts for about 2s. And the variation increases as the heating rate increases. In all the relevant experiments, the shortest holding time is 5s, which means by the time the sample is quenched, the temperature is already steady, hence 800°C. Hence, this small fluctuation can be neglected and does not affect the results.

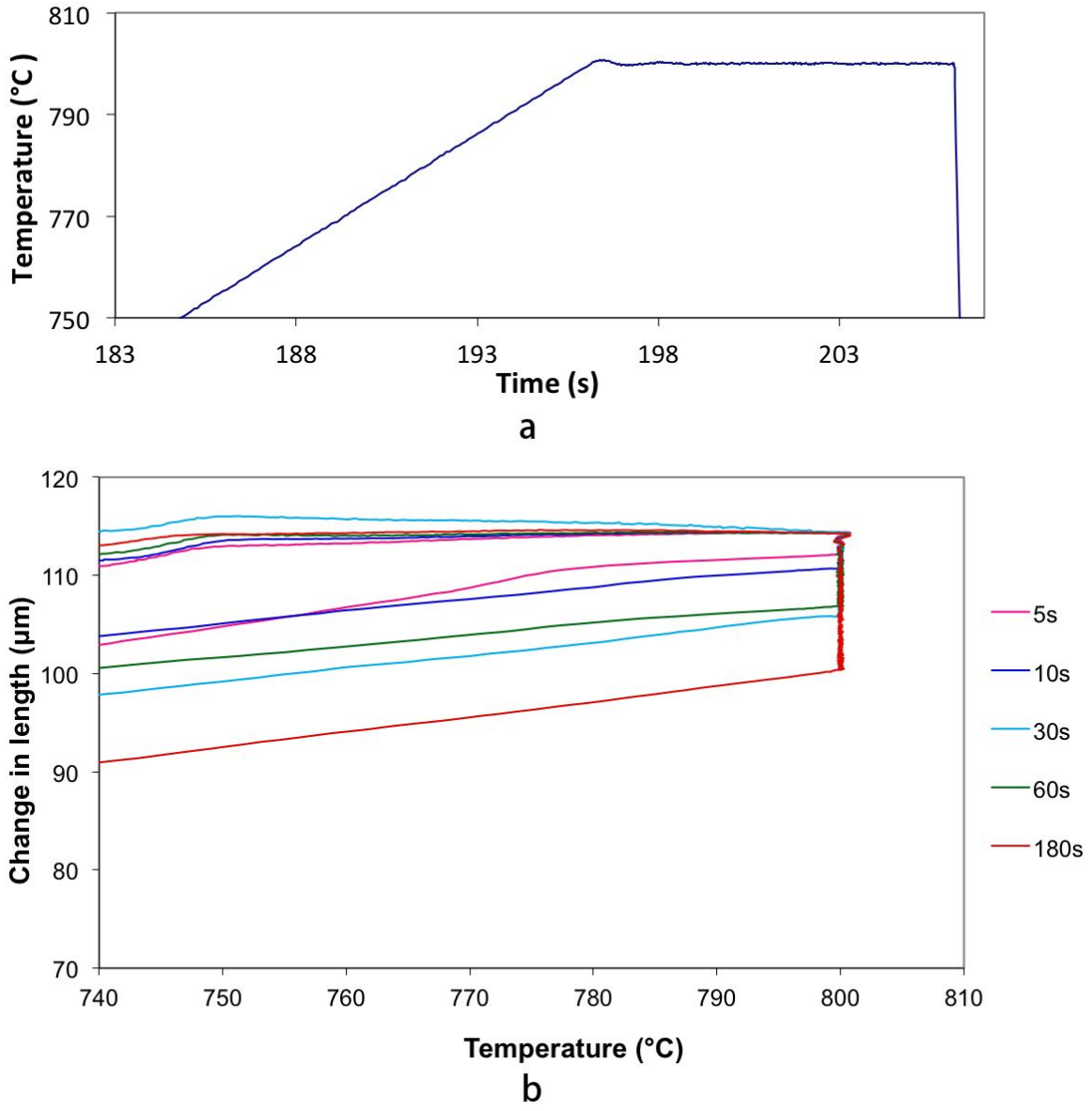


Figure C.6: Dilatometer curve of austenite transformation while intercritical annealing for HR4, top temperature 800°C, holding time from 5s to 180s: (a) heat treatment curve, time versus temperature, holding time 10s; (b) the dilatometer curve at high temperature for austenite transformation.

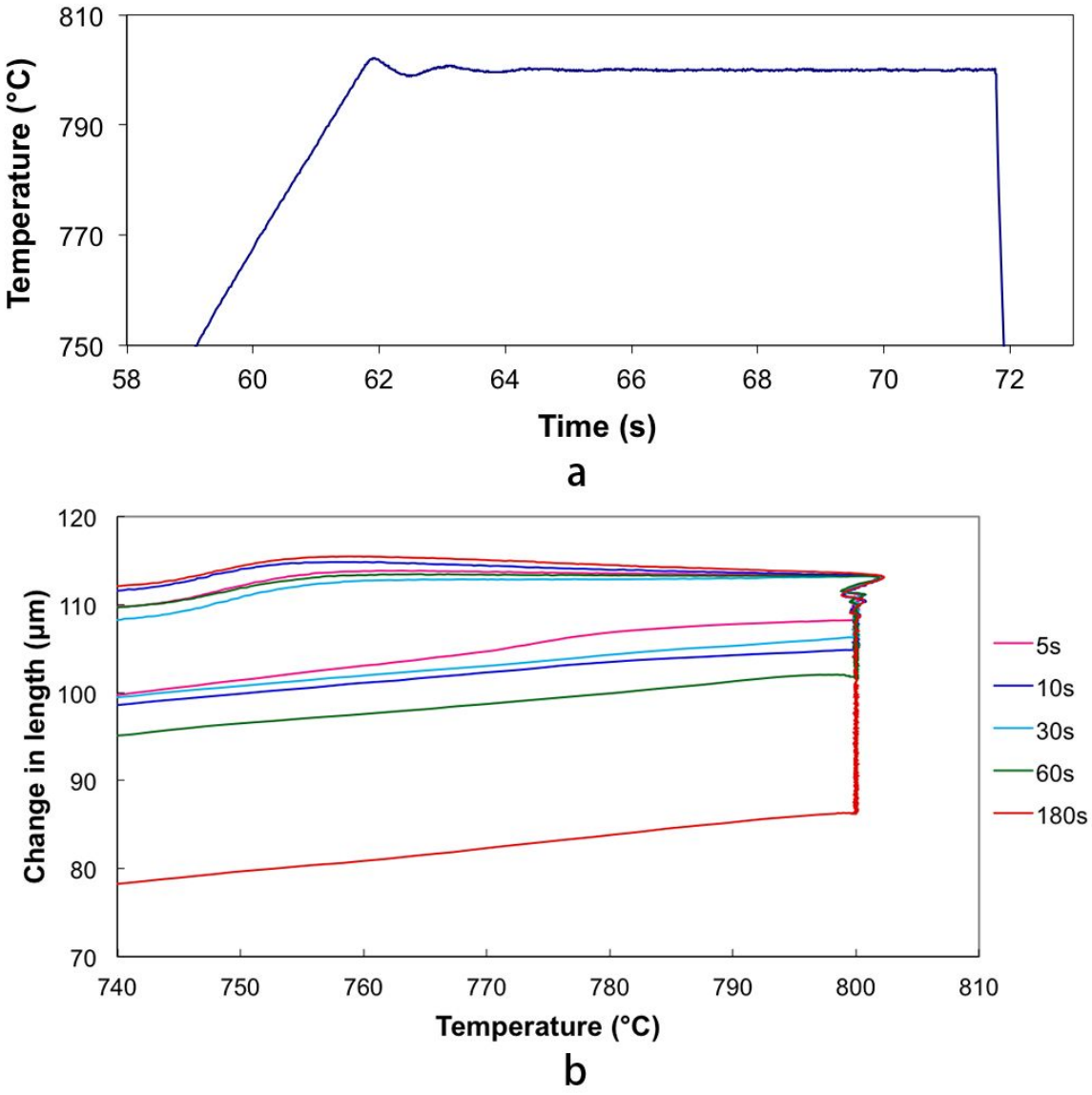


Figure C.7: Dilatometer curve of austenite transformation while intercritical annealing for HR18, top temperature 800°C, holding time from 5s to 180s: (a) heat treatment curve, time versus temperature, holding time 10s; (b) the dilatometer curve at high temperature for austenite transformation.

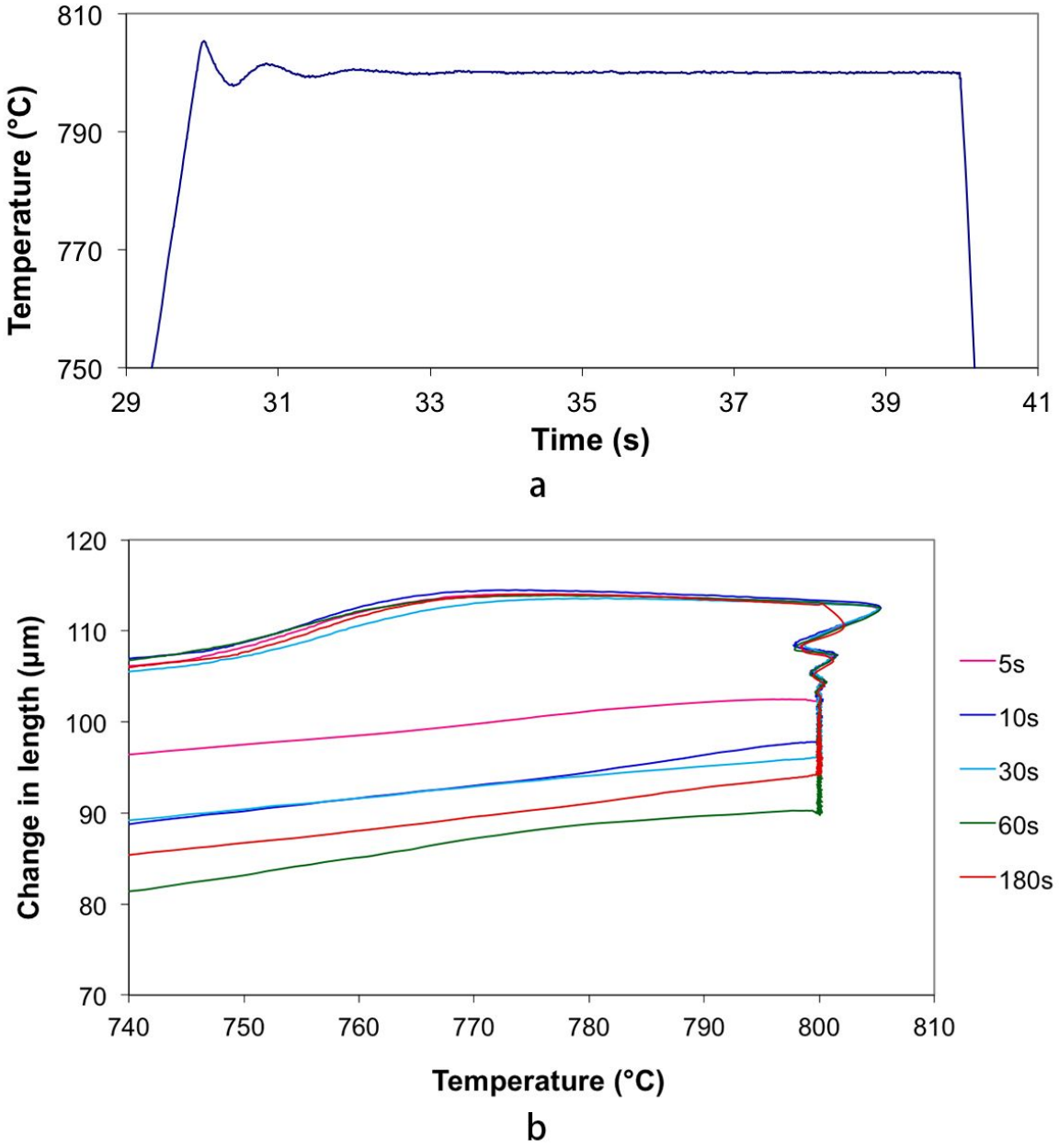


Figure C.8: Dilatometer curve of austenite transformation while intercritical annealing for HR80, top temperature 800°C, holding time from 5s to 180s: (a) heat treatment curve, time versus temperature, holding time 10s; (b) the dilatometer curve at high temperature for austenite transformation.

# D

# SEM pictures

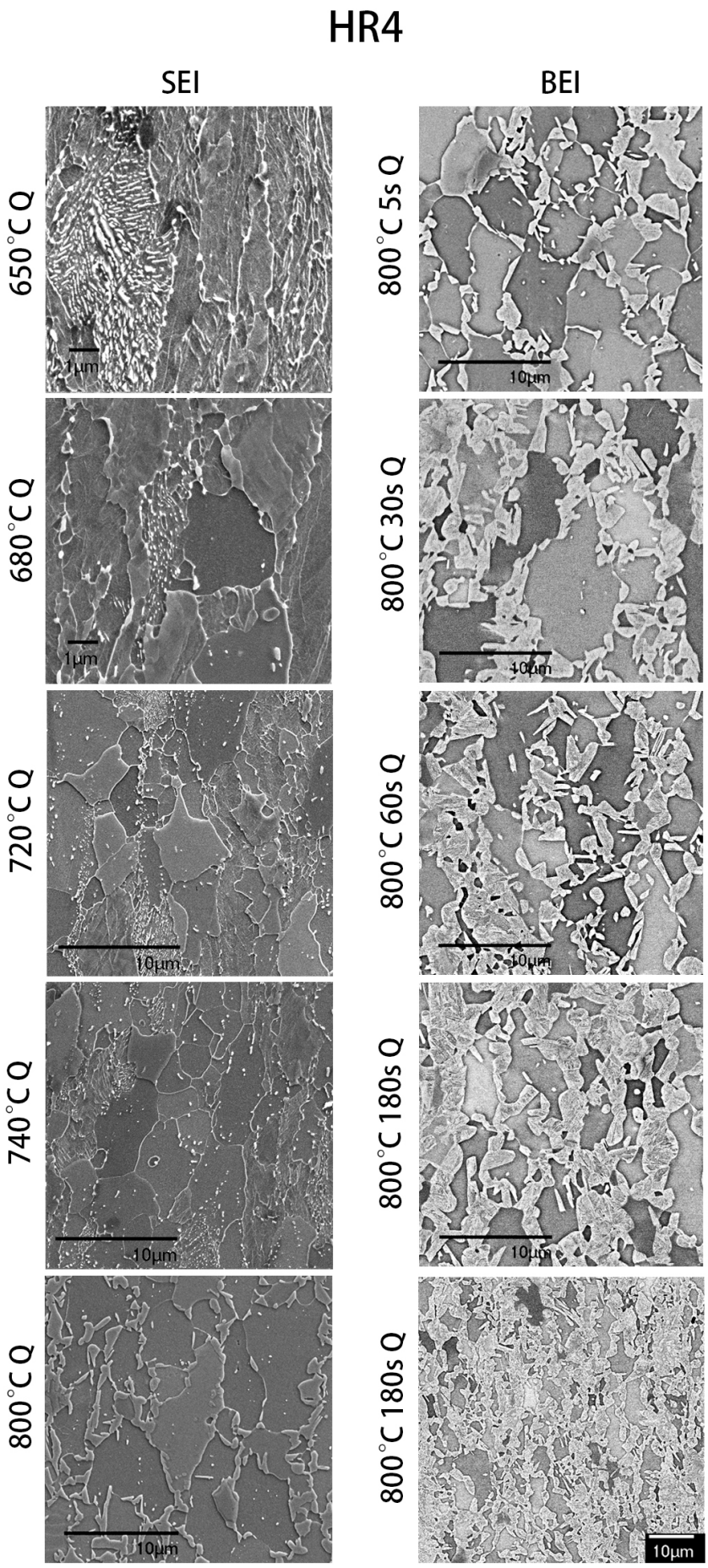
HR4
SEI
BEI
650°C Q
680°C Q
720°C Q
740°C Q
800°C Q
800°C 5s Q
800°C 30s Q
800°C 60s Q
800°C 180s Q
800°C 180s Q
1µm
1µm
10µm
10µm
10µm
10µm
10µm
10µm
10µm

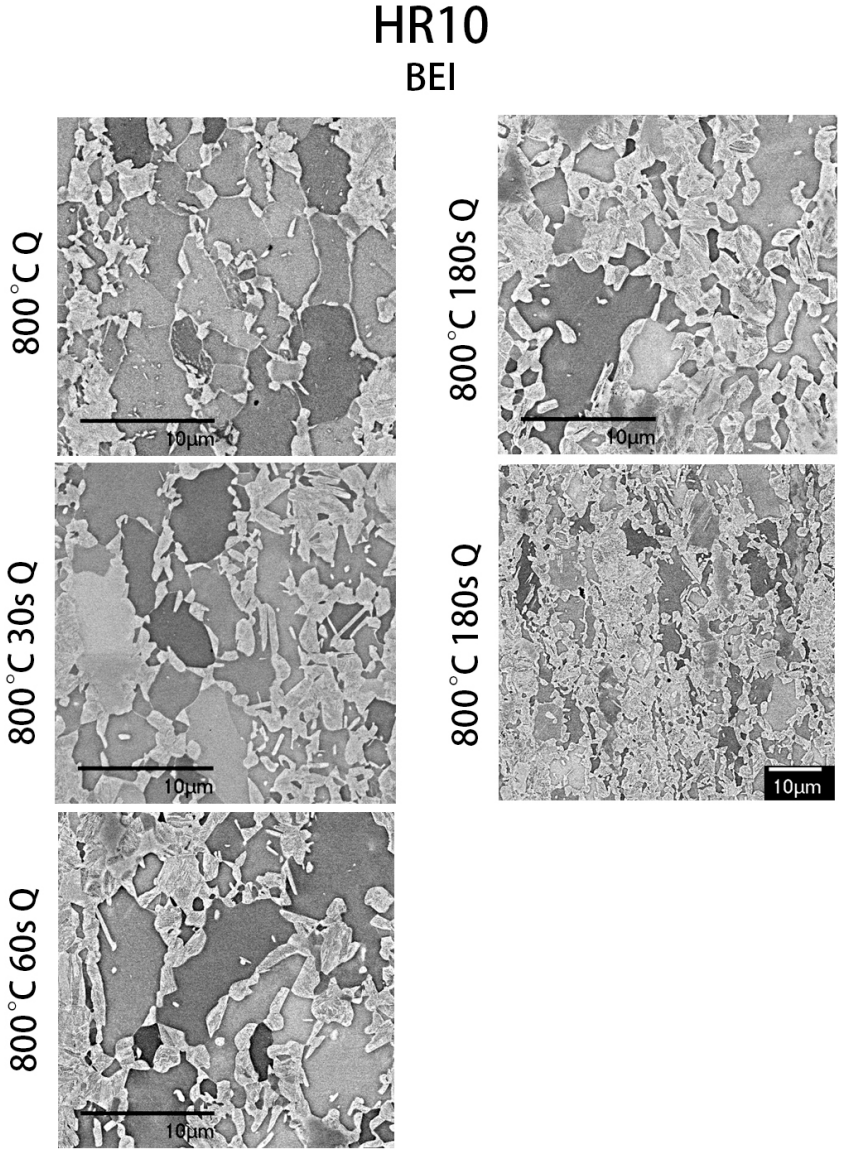
HR10
BEI
800°C Q
800°C 180s Q
800°C 30s Q
800°C 180s Q
800°C 60s Q
10µm
10µm
10µm
10µm
10µm

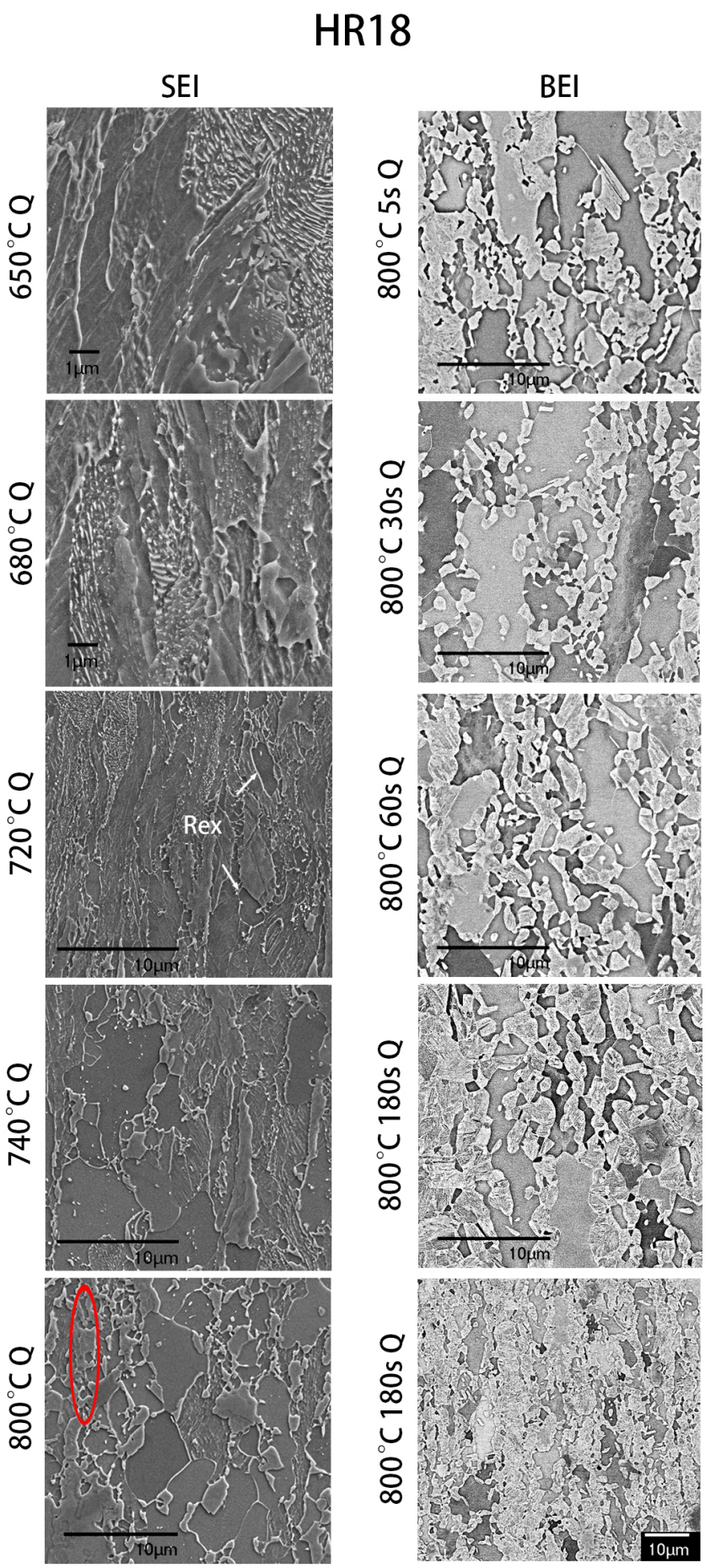
HR18
SEI
BEI
650°C Q
680°C Q
720°C Q
740°C Q
800°C Q
800°C 5s Q
800°C 30s Q
800°C 60s Q
800°C 180s Q
800°C 180s Q
Rex
1µm
10µm

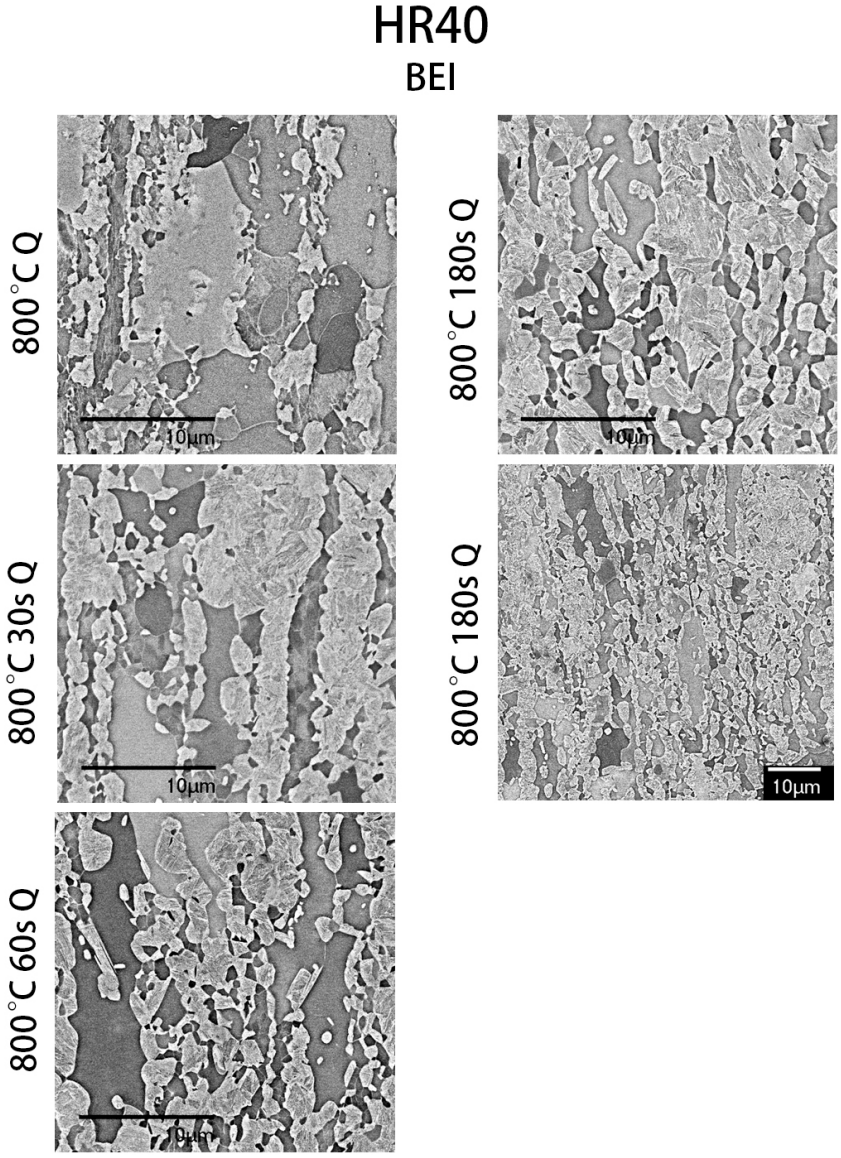
HR40
BEI
800°C Q
800°C 180s Q
800°C 30s Q
800°C 180s Q
800°C 60s Q
10µm
10µm
10µm
10µm
10µm

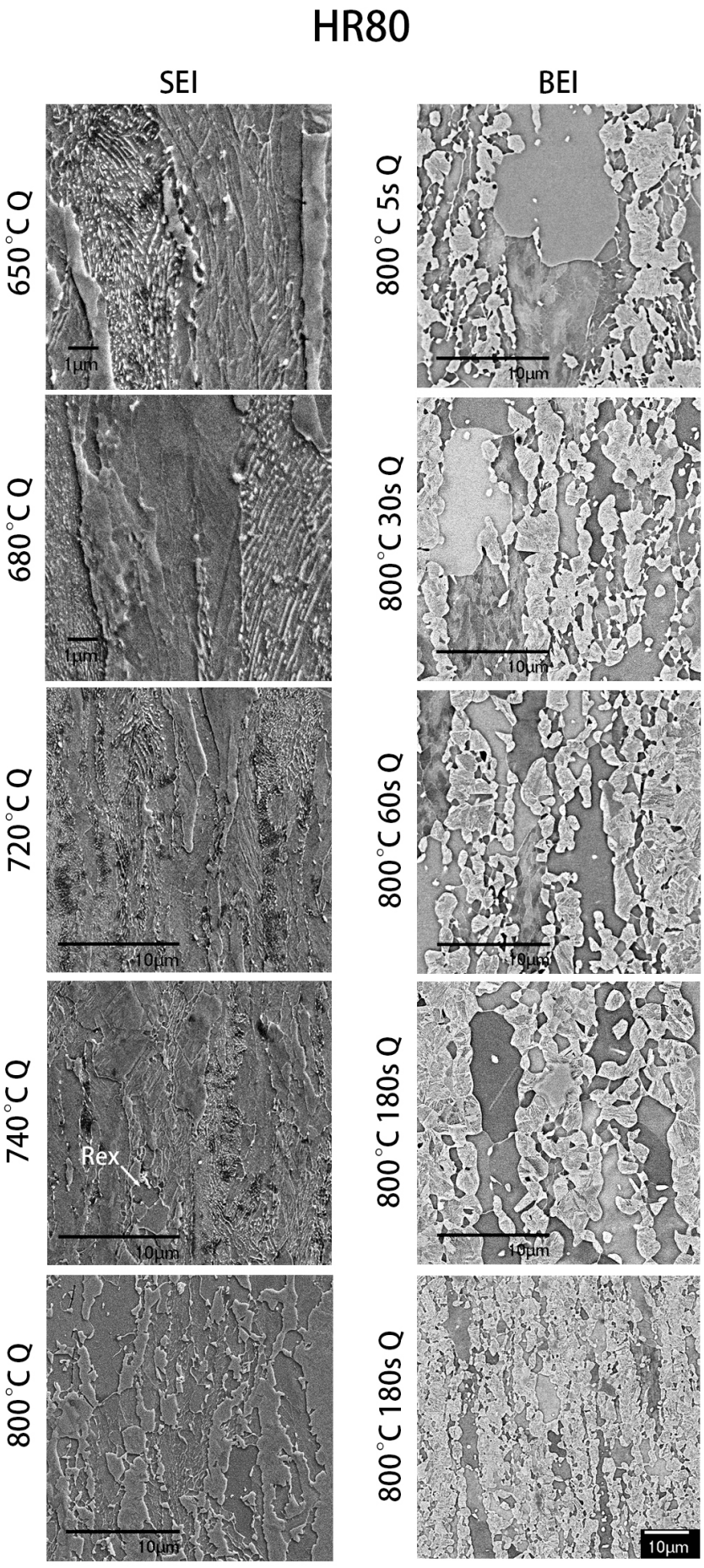
HR80
SEI
BEI
650°C Q
680°C Q
720°C Q
740°C Q
800°C Q
800°C 5s Q
800°C 30s Q
800°C 60s Q
800°C 180s Q
800°C 180s Q
1µm
10µm
Rex

# Bibliography


[1] V Andrade-Carozzo and Pascal J Jacques. Interactions between recrystallisation and phase transformations during annealing of cold rolled nb-added trip-aided steels. In *Materials science forum*, volume 539, pages 4649–4654. Trans Tech Publ, 2007.

[2] KW Andrews. Empirical formulae for the calculation of some transformation temperatures. *J. Iron Steel Inst*, 203(7):721–727, 1965.

[3] David Barbier, Lionel Germain, Alain Hazotte, Mohamed Gouné, and Abdelahad Chbihi. Microstructures resulting from the interaction between ferrite recrystallization and austenite formation in dual-phase steels. *Journal of Materials Science*, 50(1):374–381, 2015.

[4] C. Bos, M. G. Mecozzi, and J. Sietsma. A microstructure model for recrystallisation and phase transformation during the dual-phase steel annealing cycle. *Computational Materials Science*, 48(3):692–699, 2010.

[5] C. Bos, M. G. Mecozzi, D. N. Hanlon, M. P. Aarnts, and J. Sietsma. Application of a three-dimensional microstructure evolution model to identify key process settings for the production of dual-phase steels. *Metallurgical & Materials Transactions A*, 42(12):3602–3610, 2011.

[6] P. J. Brofman and G. S. Ansell. On the effect of fine grain size on the m s temperature in fe-27ni-0.025c alloys. *Metallurgical & Materials Transactions A*, 14(9):1929–1931, 1983.

[7] J. W. Christian. Order-disorder transformations - the theory of transformations in metals and alloys. *Theory of Transformations in Metals and Alloys*, page 422–79, 2002.

[8] J. W. Christian. *The Theory of Transformations in Metals and Alloys*. Pergamon Press, Oxford, 2002.

[9] RA Grange and HM Stewart. The temperature range of martensite formation. *Trans. AIME*, 167:467–501, 1946.

[10] J. R. C. Guimarães and J. C. Gomes. A metallographic study of the influence of the austenite grain size on martensite kinetics. *Acta Metallurgica*, 26(10):1591–1596, 1978.

[11] M. Hillert, J. Odqvist, and J. Ågren. Interface conditions during diffusion-controlled phase transformations. *Scripta Materialia*, 50(4):547–550, 2004.

[12] Mats Hillert. Phase equilibria, phase diagrams, and phase transformations: Their thermodynamic basis. *Zeitschrift Für Physikalische Chemie*, 211(Part 2):227–228, 1998.

[13] Paul Van Houtte, Saiyi Li, Marc Seefeldt, and Laurent Delannay. Deformation texture prediction: from the taylor model to the advanced lamel model. *International Journal of Plasticity*, 21(3):589–624, 2005.

[14] J Huang, WJ Poole, and M Militzer. Austenite formation during intercritical annealing. *Metallurgical and Materials Transactions A*, 35(11):3363–3375, 2004.

[15] G. Inden and C. R. Hutchinson. Interfacial conditions at the moving interface during growth of ferrite from austenite in fe-c-(x) alloys. In *Summaries of technical papers of Annual Meeting Architectural Institute of Japan. D-1, Environmental engineering I, Room acoustics and acoustic environment noise and solidborne sound environmental vibration light and color water supply and drainage water environment urban installation and environmental management environmental psychology and physiology environmental design electro-magnetic environment*, pages 263–264, 2003.

[16] ASM International. "chapter 2: Theory of heating by induction". *Practical Induction Heat Treating www.asminternational.org/bookstore*, 2001.

[17] Nobusuke Kariya, Norio Kanamoto, Hidekazu Ookubo, Yoshiharu Kusumoto, and Takeshi Fujita. High carbon hot rolled steel sheet and method for manufacturing same, June 19 2006. US Patent App. 11/922,250.

[18] OG Kasatkin, BB Vinokur, and VL Pilyushenko. Calculation models for determining the critical points of steel. *Metal Science and Heat Treatment*, 26(1):27–31, 1984.

[19] D. P. Koistinen and R. E. Marburger. A general equation prescribing the extent of the austenite-martensite transformation in pure iron-carbon alloys and plain carbon steels. *Acta Metallurgica*, 7(1): 59–60, 1959.

[20] Gerben P. Krielaart, Jilt Sietsma, and Sybrand Van Der Zwaag. Ferrite formation in fe-c alloys during austenite decomposition under non-equilibrium interface conditions. *Materials Science & Engineering A*, 237(2):216–223, 1997.

[21] Jan Mahieu, BC De Cooman, and J Maki. Phase transformation and mechanical properties of si-free cmnal transformation-induced plasticity-aided steel. *Metallurgical and Materials Transactions A*, 33(8): 2573–2580, 2002.

[22] M. G. Mecozzi. Phase field modelling of the austenite to ferrite transformation in steels. *Management Science*, 35(3):285–303, 2007.

[23] D. Mumford, G. Fourlaris, A. Smith, and N. Silk. The interaction of recrystallization and transformation during the reheating of multiphase steels. *AISTECH -CONFERENCE PROCEEDINGS-*, 2:831–842, 2008.

[24] Roumen Petrov, Leo Kestens, and Yvan Houbaert. Recrystallization of a cold rolled trip-assisted steel during reheating for intercritical annealling. *ISIJ international*, 41(8):883–890, 2001.

[25] GA Roberts and RF Mehl. The mechanism and the rate of formation of austenite from ferrite-cementite aggregates. *Transactions of the ASM*, 31:613–650, 1943.

[26] RO Rocha, TMF Melo, EV Pereloma, and DB Santos. Microstructural evolution at the initial stages of continuous annealing of cold rolled dual-phase steel. *Materials Science and Engineering: A*, 391(1):296–304, 2005.

[27] J. Rudnizki, B. Böttger, U. Prahl, and W. Bleck. Phase-field modeling of austenite formation from a ferrite plus pearlite microstructure during annealing of cold-rolled dual-phase steel. *Metallurgical & Materials Transactions Part A*, 42(8):2516–2525, 2011.

[28] Jenny Rudnizki, Ulrich Prahl, and Wolfgang Bleck. Phase-field modelling of microstructure evolution during processing of cold-rolled dual phase steels. *Integrating Materials & Manufacturing Innovation*, 1 (1):1–13, 2012.

[29] Viktoria Ivanivna Savran. *Austenite formation in C-Mn steel*. TU Delft, Delft University of Technology, 2009.

[30] MM Souza, JRC Guimaraes, and KK Chawla. Intercritical austenitization of two fe-mn-c steels. *Metallurgical Transactions A*, 13(4):575–579, 1982.

[31] GR Speich, A Szirmae, and MJ Richards. Formation of austenite from ferrite and ferrite-carbide aggregates. *TRANS MET SOC AIME*, 245(5):1063–1074, 1969.

[32] GR Speich, VA Demarest, and RL Miller. Formation of austenite during intercritical annealing of dual-phase steels. *Metallurgical Transactions A*, 12(8):1419–1428, 1981.

[33] I. Steinbach. Advances in materials theory and modeling - bridging over multiple-length and time scales. *San Francisco: MRS*, pages AA7.14.1 – AA7.14.6, 2001.

[34] I. Steinbach, F. Pezzolla, B. Nestler, M. Seeßelberg, R. Prieler, G. J. Schmitz, and J. L. L. Rezende. A phase field concept for multiphase systems. *Physica D Nonlinear Phenomena*, 94(3):135–147, 1996.

[35] J. Tiaden, B. Nestler, H. J. Diepers, and I. Steinbach. The multiphase-field model with an integrated concept for modelling solute diffusion. *Physica D Nonlinear Phenomena*, 115(1–2):73–86, 1998.

[36] J Trzaska and LA Dobrzański. Modelling of cct diagrams for engineering and constructional steels. *Journal of Materials Processing Technology*, 192:504–510, 2007.

[37] John D Verhoeven. *Fundamentals of physical metallurgy*. Wiley New York, 1975.

[38] Hong-Seok Yang and HKDH Bhadeshia. Austenite grain size and the martensite-start temperature. *Scripta materialia*, 60(7):493–495, 2009.

[39] Joon Jeong Yi, In Sup Kim, and Hyung Sup Choi. Austenitization during intercritical annealing of an fe-c-si-mn dual-phase steel. *Metallurgical Transactions A*, 16(7):1237–1245, 1985.

[40] Chengwu Zheng and Dierk Raabe. Interaction between recrystallization and phase transformation during intercritical annealing in a cold-rolled dual-phase steel: A cellular automaton model. *Acta Materialia*, 61(14):5504–5517, 2013.